UCLouvain

AGRO LOUVAIN

Faculté des bioingénieurs

Assessing thermal energy storage potential in the groundwater body of Louvain-la-Neuve

Auteur : Quentin VAN BAMBEKE
Promoteurs : Prof. Patrick GERIN
Prof. Marnik VANCLOOSTER
Lecteurs : Prof. Mathieu JAVAUX
M. Marc SERVAIS

Année académique 2023-2024

Mémoire de fin d'études présenté en vue de l'obtention du diplôme de Bioingénieur : Sciences et technologies de l'environnement

Acknowledgements

Before delving into the main topic, I would like to express my gratitude to all individuals who contributed to the successful completion of this Master Thesis.

First of all, I would like to thank Professor Patrick Gerin and Professor Marnik Vanclooster, my supervisors, for letting me work on a topic that was dear to my heart. I am grateful for their availability and their helpful methodological and editorial guidance.

I also want to acknowledge the research team led by M. Vanclooster, including his PhD students, for their support and advice during the weekly meetings. A special thank you to Alice Alonso for her advice and to François Toussaint for his help with the development of the lithostratigraphic model of the study area.

I would also like to take this opportunity to thank the members of the jury, Professor Mathieu Javaux and M. Marc Servais, for taking the time to read my Master Thesis and to attend the final defense.

I also wish to thank my godmother for dedicating her time to review my work, and for improving the document.

Lastly, I would like to thank my family and friends for their support and encouragement throughout my studies, of which this work represents the completion.

Table of contents

List of abbreviations

ATES	Aquifer Thermal Energy Storage
BL72	Belgian Lambert 1972
BSC	Blocry Sport Centre
BTES	Borehole Thermal Energy Storage
c	Volumetric heat capacity $\left[\frac{J}{m^3.K}\right]$
COD	Chemical Oxygen Carbon
COP	Conference of the parties
COP_{HP}	Coefficient of Performance of the Heat Pump
D_h	Thermal diffusivity [m²/s]
DTM	Digital Terrain Model
EIA	Environmental Impact Assessment
EP	Environmental Permit
GHG	Greenhouse Gas
GTPL	*Service de gestion technique du patrimoine de Louvain-la-Neuve*
HEX	Heat Exchanger
HP	Heat Pump
IDW	Inverse Distance Weighting
IPCC	Intergovernmental Panel on Climate Change
IQR	Interquartile range: $Q3 - Q1$.
LHS	Latent Heat Storage
LLN	City of Louvain-la-Neuve
LOOCV	Leave-One-Out Cross Validation

OD	Oxygen Demand
OLLN	Municipality of Ottignies-Louvain-la-Neuve
PCM	Phase Change Material
PTES	Pit Thermal Energy Storage
$Q1$	Fist/Lower quartile (value below which 25% of the data are found when arranged in ascending order)
$Q3$	Third/Upper quartile (value below which 75% of the data are found when arranged in ascending order)
Q_{in}	Energy absorbed by the heat pump
Q_{out}	Energy transferred to the building by the heat pump
R	Thermal Retardation $\left[\frac{m_{solute}}{m_{water}}\right]$ or $\left[\frac{m_{thermal\ energy}}{m_{water}}\right]$
R^2	Determination coefficient [-]
RMSE	Root Mean Square Error
SHS	Sensible heat Storage
SSE	Sum of Squared Errors
$\bar{T}$	Average temperature [°C]
TCES	Thermochemistry Energy Storage
TES	Thermal Energy Storage
TSM	Thermochemical Storage Material
TTES	Tank Thermal Energy Storage
u	Natural groundwater velocity [m/y]
u_*	Heat Transport Velocity [m/y]
USGS	United States Geological Survey
UTES	Underground Thermal Energy Storage

W_m	Mechanical Work

Glossary

Anisotropic: Refers to a property of a material or medium in which certain characteristics or behaviors are not the same in all directions.

Dispersivity (α) [m]: Property of porous media that determines the characteristic dispersion of the medium. In general, the transverse dispersion is smaller than the longitudinal dispersion by a factor of 10 and the vertical transverse dispersivity is often small as well (Bear, 1979; Domenico & Schwartz, 1998).

Effective porosity (n_e) [$m^3_{mobile\ water}/m^3_{total}$]: Refers to the fractional volume of interconnected pore spaces that allows fluid flow through the material. Effective porosity is defined as the ratio of the volume of interconnected pore spaces to the total volume of the sample (Freeze & Cherry, 1979).

Hydraulic conductivity (K) [m/s]: Ability of a porous material to transmit water. It describes the ease with which water can move through the pore space or fracture network of the material.

Specific yield (S_y) [$m^3_{water\ drained\ by\ gravity}/m^3_{total}$]: For an unconfined aquifer, specific yield represents the volume of water that an aquifer releases from storage per unit surface area of aquifer per unit decline in the water height (Chiang & Kinzelbach, 1998). In other words, this term is used to describe the ratio of the water that drains by gravity [m^3] to the total volume of sample [m^3], and the value is therefore between 0 and 1 (Woessner & Poeter, 2020). The usual range of S_y is 0.01-0.30 (Freeze & Cherry, 1979).

Thermal advection: Transport of heat by a moving fluid.

Thermal conductivity (k) [W/mK]: Measure of a material's ability to conduct heat.

Thermal recovery: Ratio between the extracted thermal energy from the subsurface and the amount initially stored (Sommer et al., 2013).

Thermocline region: Layer in a body of water where there is a rapid change in temperature with depth, creating a distinct separation between warmer upper water and colder deeper water.

Transmissivity (T) [m^2/s]: Expresses the rate of water flow (for a unit width) through the entire thickness of an aquifer. It is calculated by integrating the hydraulic conductivity over the entire saturated water head of the aquifer (Freeze & Cherry, 1979; Ruthy et al., 2017).

1. Introduction

The end of the XXth century and the beginning of the XXIst century have seen an increase in the awareness of the impact of human activities on the climate. Indeed, various studies have been carried out (over the last few decades) in order to assess the current state of the climate or to try to find solutions to limit the climate change in the future (Nalau & Verrall, 2021). This is especially the case for the IPCC, for which the first IPCC report, published in 1990, showed that global warming is mainly due to the increase in greenhouse gas emissions into the atmosphere as a consequence of anthropic activities (IPCC, 1992). This report also indicated the need for action to cope with climate change: measures were then drawn up at the "Conference of the parties (COP)", whose first session took place in 1995 (UNFCCC, 1995). The IPCC advises to do all that is needed to avoid a global average temperature increase of 1.5°C by 2100: it is therefore essential to reduce greenhouse gas (GHG) emissions by at least 40% by 2030 (United Nations, n.d.) compared with 1990 (Sénat, 2016) and by more than 80% by 2050 compared to the same period (Climat.be, 2019a).

To achieve this, it is for instance recommended to reduce the consumption of fossil fuels and increase that of renewable energies (European Parliament, 2018). In addition, the increase in prices (including of gas) due to the economic crisis that Europe has been living in recent years also forces consumers to find alternatives to consume less energy or to avoid consumption peaks, in order to reduce their energy bill.

It is in this perspective, that UCLouvain has adopted a "Transition Plan" (UCLouvain, 2021). The Blocry sports centre (BSC), as part of the UCLouvain infrastructure and located in Louvain-la-Neuve (Belgium), wants to reduce its energy bill and its GHG emissions. The BSC is open 360 days a year, so there is a need for producing heat the whole year round (such as for domestic hot water, heating of the swimming pool or of the buildings), with peaks in the non-summer period (to heat the buildings). The annual gas consumption is around 5 000 MWh.

The BSC has already collaborated with the students of the "Sustainability engineering" option in the Bioscience Engineering Faculty (AGRO-Louvain) to evaluate its consumption of gas, water and electricity and then to find solutions to reduce these consumptions. A global diagnosis showed that targeted roof insulation would be a profitable way of reducing heat losses, that building renovation and energy-saving measures through the use of a low-energy room heating management program, would reduce gas consumption (Squilbin et al., 2022). To go further in improving the BSC situation, it is necessary to look at another activity, such as heat recovery and storage. It would be interesting to collect thermal energy through solar panels or from excess heat from buildings when it is present in large quantities (i.e. in summer), to store it for several months and eventually to use it at a more appropriate moment when there is a need for heat (i.e. in winter), in order to cover a part of the energy requirements.

In this context, the **general objective** of this master thesis is to assess the potential of storage of surplus heat collected in the summer in the dynamic groundwater system of Louvain-la-Neuve (LLN) to recover the stored heat in the winter. In other words, the goal is to determine if it is possible to use the Brussels sands groundwater body presents under LLN to store thermal energy for several months, in order to save part of the fossil fuels consumed by the BSC and to reduce the impacts of its activities on the energy and economy balances and on climate. To investigate the question, a 8 km² study area centred on LLN was selected. It is mainly located on the territory of Ottiginies Louvain-la-Neuve (OLLN) and on a small part of Mont-Saint-Guibert and Chaumont-Gistoux.

2. State of the art

2.1. Heat storage usefulness and benefits

Urban areas and, therefore buildings, are responsible for one-third of the world's final energy consumption (OECD, 2013). Within this consumption, 60-70% is directly related to heating, hot water production and air conditioning systems inside buildings (Lizana et al., 2017).

The implementation of a thermal energy storage system offers many advantages, particularly in the context of Belgium, which has a temperate oceanic climate (Britannica, n.d.; Climat.be, 2019b) with a monthly average temperature ranging from 3°C (between 1°C at night and 5°C during the day) in January to 18°C (with an upper average of 24°C) in August (Weather Spark, n.d.). In addition, the frequency, the intensity and the duration of heat waves are constantly increasing (IEA, 2023), while cold waves are expected to decrease in frequency and intensity (Naumann, n.d.). There would therefore be more opportunities to store heat. Thermal storage would offer several advantages:

- First, it mitigates the seasonal imbalance between supply and demand (for heating and cooling) (Lizana et al., 2017) by recovering the surplus energy from a building and storing it to use it at a better time (in the future).
- Second, it prevents the intermittent operation of the primary heating or cooling system when only a small amount of energy is required in the building, by providing a complementary heating/cooling means that can supply enough energy without having to be started and stopped repeatedly (Lizana et al., 2017).
- Then, it reduces primary energy consumption (as well as consumption peaks) and promote the use of renewable energy sources (Lizana et al., 2017). This is achieved by compensating part of the demand with stored energy, enabling the installation of lower-powered equipment (OECD, 2013).
- Lastly, considering that only 22% of the primary energy used for heating and cooling buildings in Europe is renewable, and only 8% in Belgium (Eurostat, 2020), the deployment of heat storage facilities presents an opportunity to reduce GHG emissions into the atmosphere (Kalaiselvam & Parameshwaran, 2014). However, this is only true if heat storage contribute to an increase in GHG emissions from another source, and if it is combined with an appropriate renewable energy storage system.

While the use of a thermal energy storage system offers numerous advantages, a more detailed evaluation of its implementation requires the selection of the appropriate storage system, an examination of the potential environmental impacts associated with its use, and an exploration of the available IT tools to model its use. The legislative aspects related need also to be considered in Appendix 9.1.

2.2. Interseasonal heat storage systems

2.2.1. Types of storage systems

Thermal energy can be stored through thermochemical storage, sensible heat storage or latent heat storage (Tatsidjodoung et al., 2013).

Thermochemical storage (TCES) involves absorption and adsorption chemical reactions or physical processes using different types of materials (Lizana et al., 2017). TCES has an energy density of approximately 1000 MJ/m³, making it the most space-efficient option (Kalaiselvam & Parameshwaran, 2014; Tatsidjodoung et al., 2013).

Latent heat thermal storage (LHS) is linked to phase changes such as melting/freezing in organic materials (paraffins (mixtures of alkanes) or fatty acids, alcohols and esters), inorganic materials (such as salt hydrates, metals and eutectic mixtures) or even ice (Tatsidjodoung et al., 2013), ranging from 100 to 430 MJ/m³ (Lizana et al., 2017). More than 250 materials with a phase change range from -10°C to 120°C have been identified (Lizana et al., 2017).

Lastly, sensible heat storage(SHS) is used to store energy until 95 MJ/m³ for concrete (ΔT = 50°C), 108 MJ/m³ for underground materials (ΔT = 50°C) and 250 MJ/m³ for water (ΔT = 60°C) (Lizana et al., 2017). It is discussed in detail in section 2.2.2.

Despite the relatively high energy density and the long-term heat retention capacity of thermochemical storage materials (TSMs), their effectiveness for building applications is limited due to factors like high cost, limited availability in large quantities, and low stability and reliability over use cycles (Lizana et al., 2017). Similarly, latent heat storage encounters challenges such as the cost of Phase Change Materials (PCMs) and drawbacks related to volume variation, toxicity, flammability, or corrosivity (Lizana et al., 2017).

While thermochemical and latent heat storage require less space and have low thermal losses (Lizana et al., 2017), the associated materials are often expensive, less common, and their thermal and chemical properties may not remain stable over time or temperature variations (Lizana et al., 2017), unlike sensible heat storage. Consequently, sensible heat storage will be examined in more details to determine its suitability for LLN.

2.2.2. Sensible heat storage systems

2.2.2.1. General definition

Sensible heat storage is the most prevalent storage method for buildings energy storage (Lizana et al., 2017) due to its simplicity. It involves storing energy in a material by changing its temperature. The amount of heat stored (or released) depends on the temperature variation and the material's heat capacity (Kalaiselvam & Parameshwaran, 2014; Lizana et al., 2017;

Tatsidjodoung et al., 2013). However, it is associated with heat losses, especially with increased storage time and temperature (Fleuchaus et al., 2020; Tatsidjodoung et al., 2013).

Any material type can be used for sensible heat storage, both liquid or solid (Kalaiselvam & Parameshwaran, 2014), but the optimal volumetric storage capacity [measured in J/m³] is achieved with materials having high density [kg/m³] and specific heat [J/kg.K]. Large-scale applications are mostly used with materials that are abundant, non-toxic, and affordable (Lizana et al., 2017).

a) Stored power and related principles

The heating/cooling power supplied by the storage depends on the thermal conductivity of the material, the exchange flow rate, and the thermal diffusivity (D_h [m²/s]), which is a measure of the rate of heat transfer inside a material (Lizana et al., 2017):

$$D_h = \frac{\lambda}{\rho * C_p}$$

where:

- D_h represents thermal diffusivity $\left[\frac{m^2}{s}\right]$,
- λ is thermal conductivity $\left[\frac{W}{m.K}\right]$,
- ρ is the volumetric density of the medium $\left[\frac{kg}{m^3}\right]$, and
- C_p is the specific heat term $\left[\frac{J}{kg.K}\right]$.

Volumetric density is temperature-dependent and influenced by the material's thermal expansion coefficient (%) (Lizana et al., 2017).

High thermal conductivity (or diffusivity) indicates efficient heat transfer, facilitating rapid charging and discharging of the stored thermal energy. Thermal conductivity is affected by the material's thermal stratification capacity (indicating the temperature difference between the upper and lower portions of the storage reservoir) (Kalaiselvam & Parameshwaran, 2014). In the case of liquid materials, this stratification is also generated by convection, related to heat transfer through the spontaneous movement of fluid due to the effect of density (Kalaiselvam & Parameshwaran, 2014). The more marked is this stratification, the easier it becomes to recover energy from the system (Kalaiselvam & Parameshwaran, 2014), as stored heat and cold are concentrated in the upper and lower parts of the reservoir, respectively (Lizana et al., 2017). Indeed, low stratification occurs when the temperature gradient is low, indicating high thermal conductivity (λ) or high thermal diffusivity (D_h). On the other hand, a high exchange rate [J/s], accentuates stratification. However, these dynamics are only true when the (liquid) material is static. Variable flow conditions could indeed create stratification.

b) Heat storage materials

While solid storage materials like rock beds/concrete (between 40 and 75°C) and metals (up to 150°C or more) can be employed, liquid materials are most commonly used for low or medium-temperature[1] sensible heat energy storage applications due to their large availability and affordable price (Lizana et al., 2017): water is one of the most widely used materials. With a specific heat (C_p) of 4.19 kJ/kg.K, (Tatsidjodoung et al., 2013), water allows a storage capacity of 100 MJ/m³ for a temperature variation of 24K (Kalaiselvam & Parameshwaran, 2014). Water has also a high thermal conductivity (of 0.58 W/m.K at 20°C) (Tatsidjodoung et al., 2013) that increases with temperature and a low thermal diffusivity (D_h) (of 0.15 mm²/s) (Lizana et al., 2017).

2.2.2.2. Underground implementation: Underground Thermal energy Storage

In the underground, water is naturally abundant (Lizana et al., 2017), meaning that the problems of aboveground space availability are avoided. Underground Thermal Energy Storage (UTES) is a type of storage in which thermal energy is stored in large volumes of groundwater and underground rock (Lizana et al., 2017). The utilization of underground water and materials, coupled with natural thermal insulation provided by the ground, minimizes losses compared to surface installations (Lizana et al., 2017), even though pumping and injecting water may induce convection, i.e., the mixing of (ground)water.

The use of underground water and materials in building energy systems can reduce primary energy consumption by approximately 30% (Lizana et al., 2017) provided that the storage volume is sufficient to meet annual energy demands. UTES system allows the storage of thermal energy, either heat or cold, over long periods, even for several months. The system includes a "hot well" for storing surplus summer heat and a "cold well" for available winter cold. However, the storage duration can be adjusted based on the need to recover energy earlier or later than planned.

As the water is initially at ambient temperature of the groundwater body, the cooling potential is lower compared to heating. The theoretical limit is 63 MJ/m³ for cooling (Lizana et al., 2017), representing a temperature variation of 15K. This limitation is imposed to avoid going below 0°C. On the other hand, the theoretical limits is 250 MJ/m³ for heating (Lizana et al., 2017), reflecting a temperature variation of 60K, to avoid exceeding the maximum of 70°C.

a) General system operation

UTES is a relatively straightforward system requiring wells, connecting piping, heat exchanger (HEX), heat pump and the cold supplier (Cabeza, 2020; Equans Nederland, 2019). A minimum

[1] It is preferable not to exceed 70°C (Lizana et al., 2017) although it is still possible to reach over 95°C (Dahash et al., 2021).

of two wells, one cold and one warm well, is required (cf. Figure 1) (Cabeza, 2020). Two different water circuits are involved: one connecting the aquifer wells to the heat exchanger (HEX), and one that remains above ground, connecting the heat exchanger to the building (closed circuit). (Cabeza, 2020). The building's heating/cooling demands can be supplied by various systems, such as air distribution, fan coils units, radiant ceilings or radiant heating (Cabeza, 2020).

The system works as a loop, with both a “summer” and a “winter” mode, as described in the following two sections (Cabeza, 2020).

Summer: cold consumption and heat storage

In summer (cf. left of Figure 1), when indoor temperatures rise, cold water from the "cold well" (available at around 5-10°C (Bloemendal & Hartog, 2018)) is extracted and passed through the heat exchanger (HEX) on the surface to transfer its energy to the (closed) other circuit. This cools the building by absorbing its excess heat, and the heated water is then stored in the "warm well" at around 15-18°C (Bloemendal & Hartog, 2018). It is also possible to store heat in water at 70-80°C, depending on the heat source used (Valstar & Hoekstra, n.d.) but the losses become significant (Fleuchaus et al., 2020).

In extreme conditions (cf. right of Figure 1), when cooling requirements are high, an additional heat pump (HP) is used. This produces colder water for building cooling and warmer water as a by-product, to be stored in the groundwater body (cf. right of Figure 1) (Cabeza, 2020).

In addition to store the thermal energy naturally available in buildings during periods of elevated temperatures, energy can also come from auxiliary sources, typically from solar thermal energy (through the use of solar panels) by storing surplus production (Lizana et al., 2017; Xu et al., 2014). Waste heat from industrial processes or co-generators is another potential source, although less common (Cabeza, 2020).

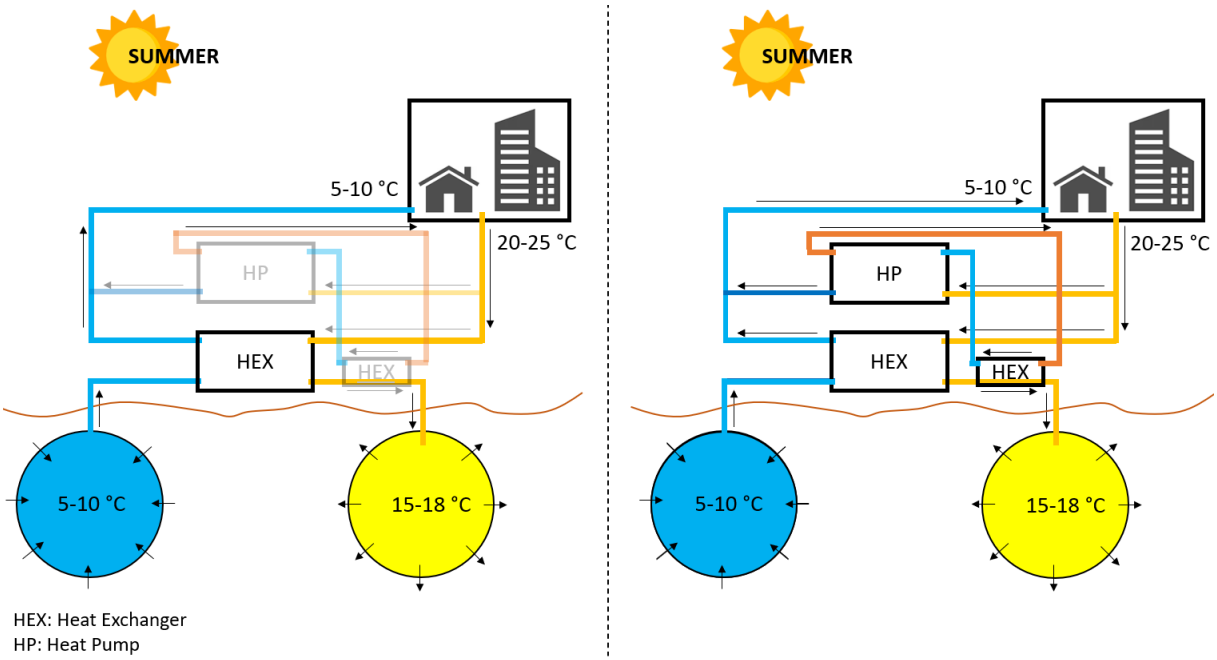

Figure 1 - Storage system operation during the summer period (left: normal operation, right: peak consumption)

Winter: heat consumption and cold storage

During the following winter (cf. Figure 2), the hot water stored during the summer is used to meet the building's heat demand. The heat stored in the groundwater is transferred to the other (closed) water circuit, using the heat exchanger. Due to heat losses, the water temperature is insufficient to meet the building's heating needs. It is therefore necessary to use an electrically-powered "heat pump (HP)", which extracts more heat from the water, producing colder water that is stored in the cold well. Simultaneously, warmer water is generated, which can be used to heat the building. Then, the water leaves the building and follows the reverse path: it reaches the heat pump, where it becomes cold, then the heat exchanger, to finally reach the cold well (Cabeza, 2020).

To store cold water in the groundwater, outside air can be used (when its temperature is below 2°C) to further cool it. This is achieved by passing it through a chiller/dry cooler or a cooling tower (that consumes electricity) before sending it in the cold well (cf. Figure 2). The minimal water stored temperature is around 5°C to prevent the freezing of systems components (Cabeza, 2020).

When the heat pump (HP) is not sufficient to provide the heat required during extremely cold events, an additional heat source (such as a boiler) consuming gas or biofuel car be used to compensate the lack of available thermal energy (Cabeza, 2020; Equans Nederland, 2019). This would represent on average only 10% of total annual energy demand to supply 50% of peak heating demand (Cabeza, 2020), but it depends on the design of the system and climatic characteristics.

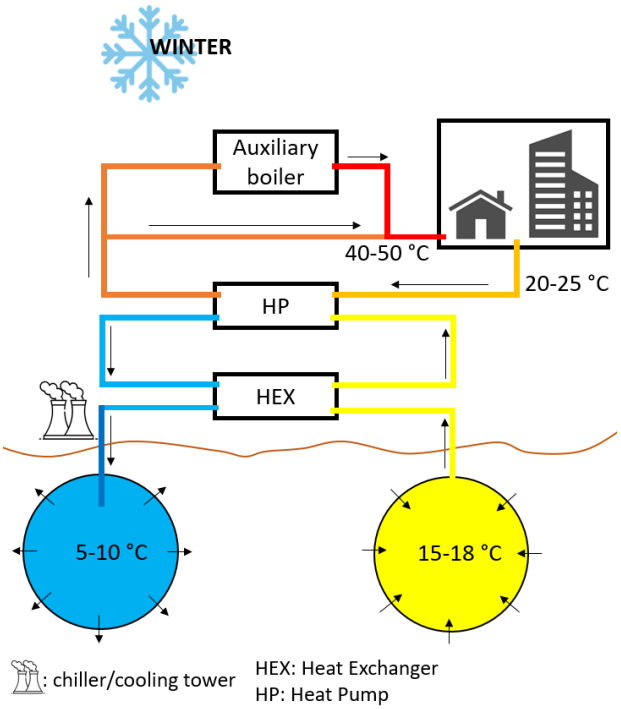

Figure 2 - Storage system operation during the winter period

Heat pump characteristics

A Heat Pump (HP) is composed of an evaporator, a compressor, a condenser, and an expansion valve. The circuit begins by absorbing energy (Q_{in}) from the water to heat transfer fluid and consequently vaporize it (in the evaporator). Then, the compressor compresses this vaporized working fluid, by producing mechanical work (W_m) that consumes electricity. Next, when the fluid is in the condenser, it transfers its energy to the building (Q_{out}) and returns to a liquid state (condenses). Finally, the expansion valve decreases the pressure of the liquid to start a new cycle.

The energy balance of the heat pump is as follows: $|Q_{out}| = Q_{in} + W_m$. The COP_{HP} is the coefficient of performance of a heat pump. It indicates the ratio between the released useful energy (Q_{out}) and the (electrical) energy consumed (W_m) by the system (Bartosiewicz, 2020; Lau et al., 2020; Yerdesh et al., 2022).

$$COP_{HP} = \frac{|Q_{out}|}{W_m} = 1 + \frac{Q_{in}}{W_m}$$

Therefore, the higher Q_{in} is compared to W_m, the better the COP_{HP} is. Thus, the COP_{HP} depends directly on the temperature of the energy source: it is preferable to have the highest possible temperature to achieve the best possible COP_{HP} and consequently, the lowest possible electrical consumption. In any case the COP_{HP} must be above 3 for it to be considered viable.

The COP_{HP} also depends on other factors, such as the temperature at the condenser outlet, the type of heat pump (i.e., the fluids it uses), the characteristics of the HP components, and the operating conditions.

b) Storage in a "closed" system (stationary water)

The basic storage system described above involves the storage of water in reservoirs that can be "open" (to the environment) or "closed". This section describes the existing technologies frequently employed in closed systems where water remains stationary, implying that water movement is only induced by injection or pumping processes.

Closed systems have advantages such as flexibility in installation locations, effective insulation (Dahash et al., 2019), and the ability to start or stop the system as desired (Lizana et al., 2017) because thermal energy is accessible at any time. Moreover, these TES systems can usually operate at higher temperatures and flow rates compared to "open" systems described in point "c)" (Dahash et al., 2019).

The thermal recovery (defined as the ratio between the extracted thermal energy from the subsurface and the amount initially stored) is higher for cold storage than for heat storage. In addition, thermal recovery decreases as the injected temperature increases, due to higher losses (Sommer et al., 2013) as the temperature difference between the injected water and the groundwater body increases.

1) "Tank Thermal Energy Storage" (TTES)

This is a common and simple sensible heat storage technology (Lizana et al., 2017) involving an insulated reservoir for storing water over a desired period (Dahash et al., 2019). The TTES storage system uses the stratification principle (Dahash et al., 2019). Heat losses are minimized by favoring a small thermocline region to avoid the mixing of warm and cold zones (Dahash et al., 2019).

Tank Thermal Energy Storage systems have a high thermal storage density (Dahash et al., 2019). However, TTES systems typically store a limited quantity of water, appropriate to the annual needs of houses (Lizana et al., 2017), due to manufacturing costs and volume constraints, generally remaining well below 100 000 m³ (Dahash et al., 2019).

2) "Pit Thermal Energy Storage" (PTES)

Similar to TTES, PTES also operates on the principle of stratification. However, it stores energy in an excavated soil surrounded by a watertight lining, with insulating walls and a floating cover, insulating the top of the pit from the external environment. PTES is generally shallower than TTES, but with a much larger diameter, making the storage volume larger, potentially

reaching several hundred thousand cubic meters. The storage material is water, occasionally mixed with rocks. (Dahash et al., 2019, 2021).

c) Storage in system "open" on the environment

In this section, the focus shifts to technologies used when the system is open to the environment, and groundwater is subject to natural flows, independent of injection and pumping wells.

In this case, the thermal recovery increases during each of the first cycles (Sommer et al., 2013). However, losses are greater than for closed storage systems, despite the storage temperatures being lower than those in the closed systems (Dahash et al., 2019).

1) Heat stored thanks to boreholes: "Borehole Thermal Energy Storage" (BTES)

Borehole Thermal Energy Storage is a prevalent thermal storage system in Europe (Lizana et al., 2017) involving a series of U-shaped pipes (boreholes) (cf. Figure 3), carrying the heat transfer fluid and spaced by 2 to 4 meters (Kalaiselvam & Parameshwaran, 2014; Rapantova et al., 2016). The heat transfer fluid in BTES systems circulates in a closed cycle (making them not very vulnerable to contamination) and use the principle of conduction to progressively exchange thermal energy between the pipes and the static storage medium, that acts as a thermal battery and insulation (Cabeza, 2020). Thus, the larger the borehole, the better the energy transfer performance will be (Kalaiselvam & Parameshwaran, 2014). BTES systems make it possible to store cold water at less than 5°C using a mixture of water and antifreeze (Cabeza, 2020; Velraj, 2016).

The most common configuration for BTES systems is vertical, where heat is injected at the centre and the pipes travel back and forth in depth to gradually transfer the heat towards the outside of the zone (cf. Figure 3). When heat is required, cold water is injected from the outside of the zone, gradually heats up and exits through the centre (Dahash et al., 2019; Kalaiselvam & Parameshwaran, 2014). In addition, BTES systems are thermally insulated at the top to prevent losses to the atmosphere (Rapantova et al., 2016).

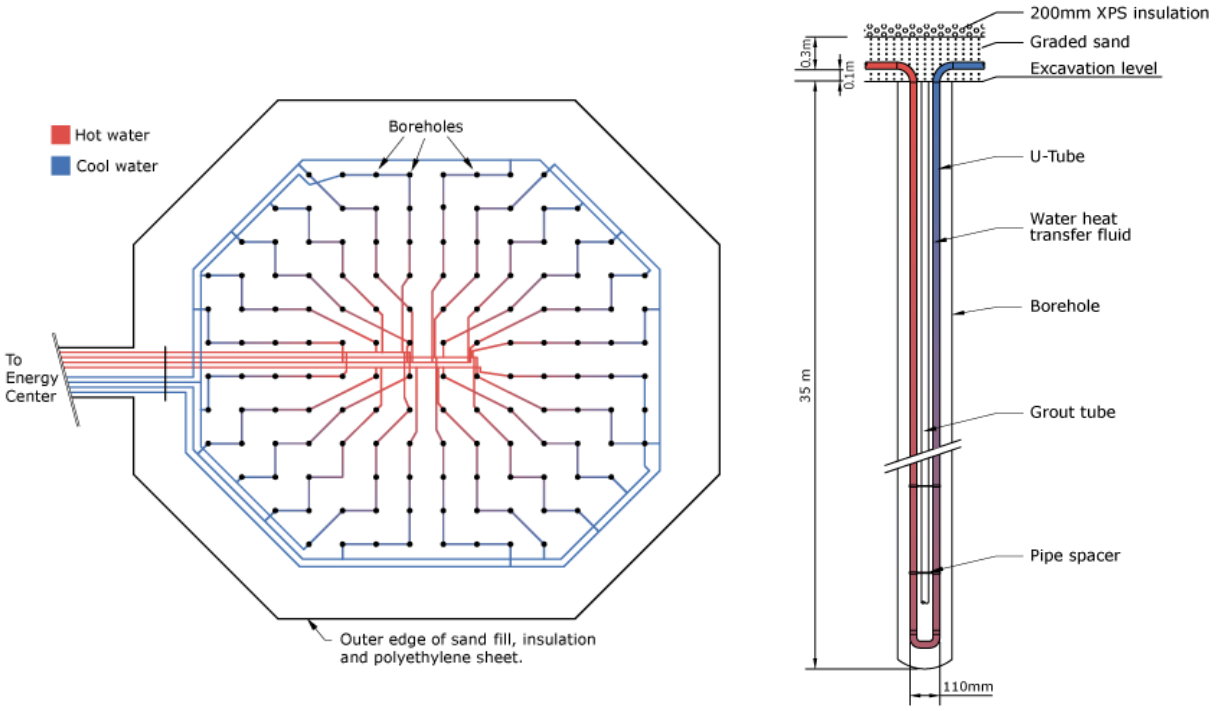

Figure 3 – Top view of a vertical BTES (left) and Sideview of single BTES tube (right) (Drake Landing Solar Community, 2019; Velraj, 2016)

The pipes in BTES system typically have diameters ranging from 100 to 150 mm, extend to depths of 30-100 m, and the heat transfer fluid has a velocity between 0.5 and 1 m/s (Kalaiselvam & Parameshwaran, 2014). However, this depends on the characteristics of the storage medium (Dahash et al., 2019).

On average, BTES systems achieve a thermal recovery rate between 54% and 65% when the system is at equilibrium (on a multi-year basis) (Rapantova et al., 2016). However, the heat transfer efficiency is only about 50% at the beginning of the storage period and decreases to reach 20 to 25% after 100 days, as the temperature difference between the heat transfer fluid and the environment decreases during the storage period (Gao et al., 2022).

2) Heat stored thanks to wells: "Aquifer Thermal Energy Storage" (ATES)

The storage system known as ATES is similar to the BTES, but it uses the principle of convection through two wells to exchange thermal energy (with the environment, in water and rock) (Cabeza, 2020). ATES systems have lower construction costs (Dahash et al., 2019).

As water can be pumped at greater depths, where the pressure is higher compared to the surface (where the water is transported to reach the heat exchanger), significant pressure variations occur due to the change in altitude. The use of pumps is therefore necessary to bring the water to the surface or to reinject it in depth.

ATES systems can achieve pumping and injection flow rates of up to 100 m³/h, provided the characteristics of the aquifer allow for such rates (De Boever et al., 2012; Gringarten et al., 1976).

Studies have shown that thermal recovery can exceed 80% to 90% under optimal conditions (Bloemendal & Hartog, 2018), but may decrease with natural groundwater flow (Dahash et al., 2019). In the best cases, system efficiencies can still reach 72% to 80% (Bloemendal & Olsthoorn, 2018). This specific situation is described in the next point (d).

d) Difficulties of storage in moving water

Low groundwater flow velocities are advantageous for ATES operation, as stored thermal energy remains close to the injection/pumping zone (Anibas et al., 2016). However, when water is in motion, heat follows its movement, requiring anticipation of its location when recovery will be needed (Bloemendal & Olsthoorn, 2018).

The location where heat will be found several months after being injected upstream depends on several factors. During the storage period (with no injection or extraction), only the natural speed of the underground water flow and the presence of other installations in the water table near the ATES system influence the water movement. During the injection and/or extraction, the system's usage rate affects the speed, that increase with the flow rate at which the system is used (Bloemendal & Olsthoorn, 2018).

The optimum theoretical distance between wells is 80% of the natural annual flow distance (u) (Bloemendal & Olsthoorn, 2018). As thermal energy is also transmitted to the soil matrix, it doesn't travel at the same speed as water; heat travels (u_*)at around 50% of the flow speed of water, due to thermal retardation (R); with thermal retardation that depends on porosity (n) and the ratio between volumetric heat capacities of water (c_w) and aquifer ($c_{aq} = nc_w + (1-n)c_s$) (Bloemendal & Olsthoorn, 2018):

$$u_* = \frac{1}{R}u = \frac{nc_w}{c_{aq}}u \approx 0.5u$$

where:

- u_* represents the velocity of the thermal front $\left[\frac{m}{s}\right]$,
- R is the thermal retardation factor $\left[\frac{m_{thermal\ energy}}{m_{water}}\right]$,
- u represents the ambient groundwater flow velocity $\left[\frac{m}{s}\right]$,
- n is the porosity $\left[\frac{m^3{}_{void}}{m^3{}_{total}}\right]$,
- c_w is the volumetric heat capacity of water $\left[\frac{J}{m^3.K}\right]$,

- c_{aq} is the volumetric heat capacity of saturated porous medium $\left[\frac{J}{m^3.K}\right]$, and
- c_s is solids volumetric heat capacity $\left[\frac{J}{m^3.K}\right]$.

Considering all factors, the optimal practical strategy is to place wells at a distance of 40% of the yearly distance that water naturally travels (u) (Bloemendal & Olsthoorn, 2018).

However, the presence of buildings or infrastructure in urban areas sometimes prevents optimal wells placement. In such cases, wells may need to be installed in proximity on the same flow line, or slightly to the side (Bloemendal & Olsthoorn, 2018). If the downstream well cannot be installed at the optimum location, it can be placed at a greater distance. Unfortunately, in this case, it takes more time for the heat to reach the downstream well, with up to 10 years needed to reach high efficiency (i.e. to get the temperature close to the injection temperature) for a distance of 2.5*u. (Bloemendal & Olsthoorn, 2018)

Groundwater flow stretches the volume in which heat is stored, increasing the surface area over which losses occur (Bloemendal & Olsthoorn, 2018). However, when groundwater flow velocity exceeds 25 m/y, conductive heat losses become negligible compared to losses due to groundwater movement (Bloemendal & Hartog, 2018) because the energy that is lost beyond the pumped volume will never be recovered (Bloemendal & Olsthoorn, 2018). Installing several downstream wells can limit these losses (Bloemendal & Olsthoorn, 2018) and offer additional advantages. For instance, since energy is not always needed at the same moment as the predicted energy is available at the well, having multiple downstream wells allows to anticipate the need via a well located slightly upstream, or to recover the energy from a well located further downstream if it has not been possible to pump it into one of the previous wells (Bloemendal and Olsthoorn, 2018). In areas with high hydraulic conductivity, a well field installation can improve the system performance (Anibas et al., 2016).

It has also been demonstrated that heat loss by advection can be limited by using a shorter screen length[2]. However, this may not always be advised, as it limits well capacity and increases the thermal radius[3], compromising optimal storage. (Bloemendal & Olsthoorn, 2018).

[2] It refers to the length of the well screen (i.e. strainers present on the well tubes) determining the contact area between the well and the surrounding groundwater body for efficient exchange of thermal energy.

[3] It refers to the distance over which the thermal influence of a well extends in the groundwater body.

2.3. Description of Louvain-la-Neuve's (hydro)geology

Louvain-la-Neuve (LLN) is predominantly an urban area with limited available surface space. Notably, a concrete slab has been installed in the urban centre. The geological layers in the study area, as reported by B. Couly, consist of a Quaternary layer at the surface, followed by the Tongrian, Bruxellian, Landenian and, ultimately, the bedrock (Couly, 2022).

2.3.1. Composition of geological layers

The upper subsoil layers are composed of silts from the Quaternary era (Boulvain & Pingot, 2023; Dassargues & Walraevens, 2014; Wallonie.be, 2006) and of sandy-silty deposits (corresponding to the Tongrian) (Dassargues & Walraevens, 2014).

The Bruxellian sands geological layer, also known as the "Brussels Formation", consists of fine to coarse sands (Ruthy et al., 2017) with the presence of calcite ($CaCO_3$) due to the fact that the sandy formation was initially carbonated (Boulvain & Pingot, 2023), glauconite (a mineral belonging to the silicate group: "$(K,Na)_2(Fe^{3+},Fe^{2+},Al,Mg)_4[Si_6(Si,Al)_2O_{20}](OH)_4$") and silica ($SiO_2$) in certain locations (Dassargues & Walraevens, 2014). The presence of (insoluble) calcite and CO_2 leads to the presence of soluble calcium bicarbonate $Ca(HCO_3)_2$ in the aquifer water (since this is a free aquifer with a water pH of between 6.8 and 7.4) (Dassargues & Walraevens, 2014). Iron oxi(hydroxi)de is also present (Anibas et al., 2016), and anthropic activities can introduce nitrate, chloride, and sulfate (Possemiers et al., 2014).

The thickness of the Bruxellian sands varies from 10 to 70 meters (Dassargues & Walraevens, 2014), with measurements at Louvain-la-Neuve suggesting a range of 10 to 55 meters, according to data measured by the 'Gestion Technique du Patrimoine de Louvain-la-Neuve - GTPL' team, using the piezometers (Couly, 2022).

Beneath the Brussels Formation are the Landenian sands, containing silty sands, clay and sandy clay (SPW, 2010), lying on a schisto-sandstone bedrock (Wallonie.be, 2005) (Couly, 2022).

2.3.2. Characteristics of the Bruxellian sands aquifer

The Bruxellian sands aquifer is a large unconfined and porous aquifer (i.e. the flow of water is caused by gravity), approximately forty kilometres wide in the centre of Belgium (Dassargues & Walraevens, 2014; Ruthy et al., 2017).

Despite heavy exploitation (Wallonie.be, 2006) including at LLN (partly for drinking water) (Ruthy et al., 2017; UCLouvain, 2022), the groundwater level remains relatively stable over time, with multi-year fluctuations of less than 2 meters (Couly, 2022; Ruthy et al., 2017). In addition, groundwater level fluctuations due to climatic variations take 3 years to become

evident (Ruthy et al., 2017). The rivers flow northwards, serving as a natural outlet for the aquifer, with the groundwater generally flowing in the same direction (Wallonie.be, 2006).

Aquifer Parameters Values

The Bruxellian sands aquifer has a large capacity and variable hydrodynamic characteristics (Wallonie.be, 2006).

The effective porosity (n_e) of the aquifer ranges from 0.035 to 0.058 [$m^3_{mobile\ water}/m^3_{total}$] (Dassargues & Walraevens, 2014; ISSeP, 2011). The specific yield (S_y) equals the effective porosity (Bear, 1979; Chiang & Kinzelbach, 1998). The bulk density (ρ_a) is 1610 kg/m³ (Anibas et al., 2016).

The hydraulic conductivity (K) ranges between $4.2*10^{-6}$ et $1.4*10^{-4}$ m/s (Anibas et al., 2016; Ruthy et al., 2017). The upper limit is confirmed through pumping tests ($1.45*10^{-4}$ m/s), a method that takes into account large water volumes but is only feasible near pumping sites (installed at locations with high conductivity) (Dassargues & Walraevens, 2014). The transmissivity (T) varies between $6*10^{-4}$ and $3*10^{-2}$ m²/s (Ruthy et al., 2017) and permeabilities range from $1,4*10^{-6}$ to $6*10^{-3}$ m/s (Wallonie.be, 2006).

Thermal properties include a thermal conductivity (k) of 2.4 W/mK and a volumetric heat capacity of 2550 J/m³K (Anibas et al., 2016).

Diffusion characteristics reveal a low longitudinal dispersivity (α_L) from 0.016 à 1.25 m, characteristic of a homogeneous sandy aquifer. Conversely, transverse dispersivity (α_T) is high, ranging from 4.2 to 4.65 m. These values were measured at Limal, nearby LLN (Ruthy et al., 2017).

The groundwater temperature is in the range of 10 to 12°C (Couly, 2022; De Boever et al., 2012).

2.4. Impacts of UTES

The influence of Underground Thermal Energy Storage systems on the quality and composition of groundwater (presented in section 2.3.2) are influenced by temperature variations, pressure fluctuations, and the mixing of water from different depths. The effects of temperature are categorized in ascending order based on the magnitude of the variation.

2.4.1. Temperature variation

2.4.1.1. Slight temperature variation (water temperature between 0 and 25°C)

Slight temperature variations ($\Delta T \leq 15°C$), whether positive or negative (provided the temperature remains above 0°C), have minimal influence on groundwater quality (specifically the chemical composition) (Jesußek et al., 2012; Possemiers et al., 2014). Consequently, this range of temperature variations presents is no immediate risk for the quality of the drinking water supply (Possemiers et al., 2014).

Even with a temperature variation of up to 25°C (and provided the temperature remains above 0°C), the effects on mineral equilibria remain limited, if not entirely undetectable (Possemiers et al., 2014).

2.4.1.2. Impact of warmer water (25 to 50°C)

As the water temperature exceeds 25°C, microbial activity increases (potentially contributing to methanogenesis) and organic carbon (OC) starts to be mobilized, leading to an increase in groundwater chemical oxygen demand (COD) and reduction of the O_2 solubility in water (Possemiers et al., 2014).

Within the temperature range of 25 to 40°C, conditions shift towards reducing environments for nitrates and iron (III) (Jesußek et al., 2012).

Above 45°C, an increase in temperature promotes the development of a thermophilic microbial community specialized in sulfate fermentation and reduction (Possemiers et al., 2014).

2.4.1.3. Impact of high-temperature water (> 50°C)

When the water temperature exceeds 60°C, silicates dissolve, resulting in their high concentrations in hot wells due to increased silicate solubility with rising temperature (Jesußek et al., 2012). Conversely, sillicates precipitate in cold wells. (Possemiers et al., 2014). At the same temperature, carbonates precipitate (in the hot well) while they dissolve in the cold wells due to a reduction in carbonate solubility with increased temperature (Jesußek et al., 2012; Possemiers et al., 2014). Calcium also precipitates (with carbonates) (from 40°C or 70°C, depending on the source), reducing porosity and permeability (Possemiers et al., 2014). In

general, precipitations can lead to well clogging (Fleuchaus et al., 2020; Possemiers et al., 2014).

Lastly, at 70°C, conditions for sulfate become reducing, linked to microbial activity and to a greater release of organic carbon (OC) from sediments (Jesußek et al., 2012; Possemiers et al., 2014).

2.4.2. Pressure variation due to wells utilization

When the pressure drops, either in the pumping well area or in the pipes near the surface, the gas dissolved in the water tends to become gaseous (forming small bubbles), which can lead to corrosion. The proportion of gas released depends on pressure variation, influenced by depth and pumping rate. This can be avoided by artificially increasing the pressure in the pipes, after being pumped. However, this is not necessary during injection, as the pressure rises in the well zone, promoting the dissolution of gas into the water (Jenne, 1992).

2.4.3. Water mixing

Water mixing results from various processes, such as the pumping of water from different depths or the mixing that occurs at the injection well. The pumping results in the water replacement from various groundwater depths that have different compositions. During injection, a mixture is created when the injected water interacts with the surrounding water and disperses. This is more critical when waters of different compositions meet, potentially altering water quality: shallow groundwater is rich in oxygen, nitrates and other anthropogenic contaminants, while deeper groundwater contains iron (II). Therefore, the mixture leads to the oxidation of soluble iron (II) into insoluble iron (III).

In general, mixing processes therefore facilitate the transport of contaminants to deeper waters. (Possemiers et al., 2014)

It is essential to avoid installing wells near public drinking water supply wells to minimize the pumping of contaminants through these water extraction wells (Possemiers et al., 2014) (see Appendix 9.1.2 for information on protection zones).

Unlike continuous pumping wells (water catchment), ATES systems change pumping direction twice a year (when the system is installed in still water, as each well pumps and injects in turn), limiting the risk of mixing water of different quality. Additionally, most of the water has already been mixed in the previous season, reducing the risk of mixing water of different qualities when using ATES. The results from studied sites showed concentration changes that were small enough to not have impact on drinking water quality. (Possemiers et al., 2014). However, this is not true when the wells are only pumping or injecting.

2.4.4. Consequences for implementing a TES system in LLN

Considering that the groundwater body at LLN serves as a source of drinking water, it is crucial that heat storage does not induce any chemical change to it (Possemiers et al., 2014). It is therefore preferable to not exceed 25°C for thermal energy storage, especially as this limits heat loss (cf. section 2.2.2.2).

It is also important to take care to avoid the installation of an ATES system nearby a drinking water well and to minimize the mixing water from different depths, for example by limiting the length of the of the strainers present on the well tubes. (Possemiers et al., 2014)

2.5. Tools to model underground water flow

2.5.1. Characteristics of available/existing softwares

This section provides an overview of various software programs suitable for modelling underground water flow involving heat transfer.

2.5.1.1. MODFLOW

MODFLOW, developed by the United States Geological Survey (USGS), is a hydrological model requiring no license for use. Considered as a standard in hydrogeological engineering by the USGS, MODFLOW is employed for simulating and forecasting groundwater conditions and interactions with surface water. This software is linked to various programs, allowing the modelling of complex hydrogeological scenarios. (USGS, 2022)

For instance, the program can be coupled with the MT3DMS model (Simcore Software, 2023), which is able to simulate the heat transfer in groundwater based on the analogy between solute and heat transfer. It has been shown that this approximation is reliable when temperature variations are small (Fossoul et al., 2011): even with temperature differences of up to 60°C, the error in heat transport simulation remains below 3% (Hecht-Méndez et al., 2010). MT3DMS operates exclusively in the saturated zone, while MT3D-USGS extends its capabilities to unsaturated zone solute transport applications (Morway et al., 2023).

MODFLOW is able to model subsurface flows in anisotropic et heterogeneous porous media, under both stationary and transient flow conditions. It uses the finite-difference calculation method on a two or three-dimensional grid, calculating iteratively within a time step the values on the node of each of the cells (Dassargues, 2022; INOWAS, 2018; Panday et al., 2013).

Several software packages integrate MODFLOW:

a) Visual MODFLOW

Visual MODFLOW is a modelling environment with advanced visualisation and interactivity features (Waterloo Hydrogeologic, 2023a). Unfortunately, it comes with a high license cost (Waterloo Hydrogeologic, 2023b).

b) Processing MODFLOW

It is an open-source software that offer flexibility and customisation of the modelling environment according to specific needs. Indeed, the full version 8.0.47 released on 15/01/2017 entered the public domain on 25/07/2021: the license is therefore available for free (Simcore Software, 2021).

2.5.1.2. Other software

Other effective and commonly used software for hydrogeological modelling and solute and/or heat transport are FEFLOW (DHI, n.d.), HydroGeoSphere (Aquanty, n.d.) and MARTHE (BRGM, n.d.; Tiéry, 2016). They produce results similar to MODFLOW.

The licenses for FEFLOW and HydroGeoSphere are fee-based, and the free version of MARTHE offers limited functionality.

2.5.2. Transport equations

2.5.2.1. Definition of the equations

a) Solute transport

MODFLOW, when combined with the MT3DMS model, simulates solute flow in the system. The equation governing solute transport under transient conditions is (Hecht-Méndez et al., 2010; Zheng & Wang, 1999):

$$\left(1+\frac{\rho_b K_d}{n}\right)\frac{\partial C}{\partial t} = div[(D_n+\alpha v_a)gradC] - div(v_a C) + \frac{q_k C}{n}$$

with (Zheng & Wang, 1999):

$$\left(1+\frac{\rho_b K_d}{n}\right) = R$$

where:

- ρ_b is the volumetric apparent mass of the solid [kg/m³],

- K_d is the (solute) distribution coefficient [m³/kg], defined as the ratio between the concentration of solute sorbed to the surface of a solid ($\bar{C}$) and the concentration of solute in the liquid phase (C): $K_d = \frac{\bar{C}}{C}$ (Zheng & Wang, 1999),
- n is the (effective porosity) [$m^3_{mobile\ water}/m^3_{total}$],
- R is the retardation factor [m_{solute}/m_{water}],
- C represents the total solute concentration [kg/m³],
- t is the time [s],
- D_n is the molecular diffusion [m²/s],
- α is the dispersivity [m],
- v_a is the groundwater velocity [m/s], and
- q_k is the well-source [1/s].

The left-hand side of the equation calculates the sum between the total concentration of solutes and the mobile concentration of solutes/contaminants where the information on the mobile concentration is derived from the K_d term and is distributed in the different phases.

The first part on the right-hand side of this equation represents the hydrodynamic dispersion, with the term αv_a (dispersivity and groundwater velocity) referring to the mechanical dispersion of solutes. The second part represents solute advection, describing the mass movement of solutes with groundwater flow, and the third one describes the influx (source) or efflux (sink) in units of [kg/m³.s], which may be related to inflow or outflow of water, or even to reactions for dissolved or sorbed phases (Zheng & Wang, 1999).

b) Heat transport

The heat transport equation, presented below, applies under the assumption of thermal equilibrium between water and the soil/rock matrix (where no net transfer of energy occurs between phases) and convection is mainly related to the pressure gradient, in transient flow through porous media. The equation takes into account heat conservation, conduction and convection (de Marsily, 1986; Fossoul et al., 2011; Hecht-Méndez et al., 2010).

$$\left(\frac{\rho_m c_m}{n\rho_w c_w}\right)\frac{\partial T}{\partial t} = div\left[\left(\underbrace{\left(\frac{\lambda_m}{n\rho_w c_w}\right)}_{=\bar{D}_h} + \alpha v_a\right) gradT\right] - div(v_a T) + \frac{q_h}{n\rho_w c_w}$$

where:

- ρ_m is the volumetric mass of the (saturated) porous medium [kg/m³],
- c_m is the (specific) heat capacity of the (saturated) porous medium [J/kg.K],
- $\rho_m c_m$ is the volumetric heat capacity of the (saturated) porous medium [J/m³K],
- n represents the (effective) porosity of the medium [$m^3_{mobile\ water}/m^3_{total}$],

- ρ_w is the volumetric mass of the fluid (water) [kg/m³],
- c_w is the (specific) heat capacity of the fluid (water) [J/kg.K],
- $\rho_w c_w$ is the volumetric heat capacity of the fluid (water) [J/m³K],
- T is the temperature (of the fluid in the porous medium) [K],
- λ_m the thermal conductivity of the porous medium [W/m.K],
- D_h represents the thermal diffusion [m²/s],
- α is the dispersivity [m],
- v_a is the effective groundwater velocity [m/s], and
- q_h is the thermal energy input or output: sink-source term [W] or [J/s]).

The term $\rho_w c_w$ [J/m³K] represents the volumetric heat capacity of the fluid. The term $\rho_m c_m$ corresponds for its part to the volumetric heat capacity of the porous medium and is calculated as the arithmetic combination of the heat capacities of both the solid rock ($\rho_w c_w$) and the interstitial fluid ($\rho_s c_s$): $\rho_m c_m = n\rho_w c_w + (1-n)\rho_s c_s$ (Hecht-Méndez et al., 2010).

The thermal conductivity (λ_m) and heat capacity (c_m) of the porous medium are the main parameters for thermal conduction and solid-fluid heat transfer. On the other hand, hydraulic conductivity (K) and effective porosity (n_e) are the main convection parameters, since they significantly influence the effective groundwater velocity (v_a). The total effective thermomechanical dispersion includes thermal diffusion and thermomechanical dispersion, dependent on longitudinal and transverse thermomechanical dispersion coefficients that vary greatly with the scale considered.

On the first term of the right-hand side of the equation, the left part represents the thermal diffusion (D_h). The term αv_a represents the mechanical dispersion (as v_a depends on hydraulic conductivity and the inverse of the effective porosity). The second term represents the thermal convection and the third one is the expression of the sink-source terms, accounting for thermal energy input or output.

2.5.2.2. Equations comparison

The use of the MT3DMS model, initially designed to describe the movement of solutes in a saturated underground environment, for heat movement is justified by the similarity of the phenomena represented:

a) Left-hand side correspondence

For both equations, the terms within the brackets on the left-hand side are dimensionless. This implies that the dimensions of all the parameters counterbalance each other. What remains are the terms $\frac{\partial C}{\partial t}$ and $\frac{\partial T}{\partial t}$, respectively representing the partial derivatives of solute and temperature with respect to time.

b) Right-hand side correspondence

The first part, which depends on molecular diffusion (D_n) and concentration (C) in the case of solute transport, becomes into thermal diffusion (D_h) and temperature (T), respectively, in the heat transfer equation, which is analogous. The terms for dispersivity (α) and groundwater velocity (v_a) are identical in both equations.

The second part replaces the concentration (C) with the temperature (T), while the groundwater velocity (v_a) remains identical in both equations. These two parts are thus similar.

The last term ($q_k C$), describing the quantity of solutes entering or leaving [kg/m³.s] is replaced by the amount of energy (or heat) entering or leaving the system $\left(\frac{q_h}{\rho_w c_w}\right)$ [m³.K/s] during a given time interval.

2.6. General information about Blocry's requirements

The Blocry Sports Centre (BSC) consumes natural gas in boilers with varying power capacities, activated either individually or collectively based on demand. These boilers are responsible for heating water to 80°C, mainly to prevent the growth of *Legionella* in the circuits until the water is used (Lemlin, 2022).

This elevated temperature is specifically targeted to ensure the quality of domestic hot water. For heating purposes, where the water remains in a closed circuit without direct contact with users, lower temperatures in the range of 40 to 50°C (as shown on Figure 2), would be sufficient. The boilers can operate all year-round to provide the BSC with domestic hot water and heating water to satisfy the centre's needs. The implementation of an ATES system could therefore assist the BSC to reduce its gas consumption.

3. Specific objectives & Strategy

3.1. Specific objectives of this work

The specific objectives of this study are:

1. To evaluate the feasibility of employing Aquifer Thermal Energy Storage in the LLN configuration, particularly in the surroundings of the Blocry's Sport Centre.
2. To analyse the behaviour of thermal plumes within the groundwater body to assess the feasibility of implementing such a system in LLN.
3. To evaluate the efficiency of the storage system in terms of proportion of the injected energy that can be recovered.
4. To identify the well locations that allows to improve the storage performance.

3.2. General approach

Initially, the approach was to consider the hydrogeological characteristics of LLN to determine the optimal storage system based on hydrogeology of the water table and the Blocry's thermal requirements.

Once the storage system was identified, the hydrogeological modelling of the groundwater body in the LLN area was examined. However, two preliminary steps were necessary before this could be done. Firstly, a lithostratigraphic prediction of geological layers was carried out to define the model. Subsequently, a simplified hydrogeological modelling at the catchment scale was performed to determine the boundary conditions of LLN. The hydrogeological modelling focused on LLN was then performed.

The next step took into account the presence of wells and thermal energy plumes in the groundwater. This was needed to search for suitable well locations in the relevant zone.

4. Materials & methods

4.1. Lithostratigraphic model

4.1.1. Creation of databases of geological layers topography

Data on the geological layers present under Louvain-la-Neuve are available as a descriptive sheet established for each piezometer drilled under and near LLN. An example of available information is presented in Appendix 9.2.1.1. The piezometers are not uniformly distributed over the study area, concentrated in Ottignies-Louvain-la-Neuve, with one in Chaumont-Gistoux and the remaining two in Mont-Saint-Guibert. These measurements, mostly rounded-up digits, have a maximum depth of 112 m (cf. Appendix 9.2.1.1).

These data were used to feed a database in CSV format containing the location of 30 piezometers with Belgian Lambert 1972 (BL72) coordinates, starting and ending elevations of each geological layer and the thickness of each of them. The data for 8 piezometers were not included due to inaccurate data. The list of the retained and removed piezometers is provided in Appendix 9.2.1.2.

4.1.2. Spatial prediction of geological layer thickness and elevation

The piezometer database contains information only at the location of the piezometer, while prediction of the groundwater flows requires a full spatial description of the aquifer. The lacking data of geological layer thickness and elevation were estimated by a kriging procedure to predict geological layer thickness on a 10 meters horizontal mesh grid. Kriging was performed on layer thicknesses rather than on the altitudes of the upper parts of each of them to prevent negative layer thickness and potential layer intersections. It is a more accurate method than alternatives (such as Inverse Distance Weighting method) when the variogram model is carefully established (Razas et al., 2023).

Using the vague spatial gradient shown on the thickness measurements for each piezometer, a plane trend that corresponds to the data variation was calculated. Then, thickness residuals, obtained by subtracting the trend from the initial data), enabled more accurate predictions for each layer.

Identification and removal of outliers were executed using boxplots. Values outside the boundaries of "$Q1 - 1.5 * IQR$" and "$Q3 + 1.5 * IQR$" were considered as outliers (Babura et al., 2018; Spitzer et al., 2014) and therefore excluded. These lower and upper boundaries represent the limits of the data within the central 95% of the dataset (Spitzer et al., 2014).

Semivariograms were used to assign a weight to each of the known data points in order to estimate the value of a given point (Razas et al., 2023). Variogram fitting implies that the

stationarity hypothesis is valid (for example, second-order stationarity means that the covariance (Cov) depends only on the distance $(\mathbf{h}_{ij})$). Variograms were first estimated based on the residuals of the thickness based on data that are stationary of order 1 (i.e. the residual expected value is identical everywhere), which then allowed variograms to be calculated on the basis of models chosen manually to best represent the situation. The modelled variograms were fitted using the "Ordinary Least Squares fitting" method.

The residuals of thickness were predicted for the entire grid as well as the prediction variance. Then, the predicted thickness was calculated by adding the predicted residuals to the trend that had been removed at the beginning. All negative geological layer thicknesses were replaced by zero values.

The altitude of each layer was calculated using a Digital Terrain Model (DTM) (Géoportail de la Wallonie, 2015) of the study site (ground surface altitude) and by repeatedly subtracting layer thicknesses from the previous layer's altitude, using the DTM as the starting reference. The DTM has a one-meter spatial resolution representation and covers all of Wallonia's ground surface. The data has a 0.12-meter altimetric accuracy and does not take into account elements present on the ground surface (such as bridges, trees, buildings, etc.). The DTM is based on measurements taken between 2012 and 2014 by Lidar technology.

4.1.3. Assessment of the prediction quality of geological layer thickness and altitude

Given that kriging uses an exact predictor, meaning that the prediction at a measuring point exactly corresponds to the measured value, the Leave-One-Out Cross-Validation (LOOCV) method was used. It consists in making predictions using all measurements except one and then comparing those predictions with the actual measured value at that specific point. It was therefore necessary to select the DTM points that corresponded to the points at which the predictions had been made (specifically on the 10 meters mesh grid), allowing the comparison of values located in exactly the same place (same latitude and longitude).

The root-mean-square error (RMSE), the sum of squares errors (SSE) and the determination coefficient (R^2) for both thickness and altitude of each geological layer were calculated.

4.2. Hydrogeological modelling

4.2.1. Simplified model of the catchment area

4.2.1.1. Delimitation of the watershed and draining river

Elevation data (DTM) for the provinces of Walloon Brabant and Flemish Brabant were simultaneously obtained from the United States Geological Survey (USGS) website. The resolution of the data, known as "SRTM[4] 1 Arc-Second Global", is 38.853 meters in the x-axis and 31.231 meters in the y-axis (USGS, n.d.-a).

The merging of downloaded layers was accomplished using QGIS, employing the "Raster > Miscellaneous > Merge" tool (Figure 33 in Appendix 9.3 shows the DTM centred on the catchment area). Contour lines were then extracted in vector format ("Raster > Extraction > Contour"), and slopes were computed using the "r.slope.aspect" algorithm from the "GRASS" plugin ("GRASS > Raster > r.slope.aspect"). Subsequently, the watershed and hydrographic network were identified using the "r.watershed" algorithm from the "GRASS" plugin ("GRASS > Raster > r.watershed"). The rasters created in QGIS were then converted into polygons ("Raster > Conversion > Polygonize") (Jonard, 2022). The entities of interest, representing the watershed containing LLN down to the first outlet, and the main watercourse, were then exported in " DXF AutoCAD" format.

4.2.1.2. Hydrogeological modelling

Given that MODFLOW provides satisfactory results despite its simplification based on solute transport to model heat transport (cf. section 2.5), there is no need for employing another program. Processing MODFLOW, particularly the version 8 (from 2017), was therefore selected, after checking that the equations were similar.

a) Model setup

The initial step was to specify the initial characteristics of the model in "Grid > Mesh size", determining the number of layers, extent (minimum and maximum coordinates in both x and y dimensions), and the number of rows and columns. The model, consisting of a single layer with a resolution of 100 m, encompassed the entire previously delimited watershed. Efforts were made to align the centre of the corresponding cells as closely as possible with the boundaries of the forthcoming LLN model.

Subsequently, the layer characteristics were encoded (Chiang, 2005; Simcore Software, 2022). The layer was defined as unconfined in "Grid > Layer property," with the upper limit corresponding to the DTM downloaded from the USGS site (USGS, n.d.-a). This DTM was

[4] Shuttle Radar Topography Mission

adjusted so that the altitude values imported via an ASCII file in "Grid > Top of layers (TOP)" reflected measurements taken at the closest proximity of the centre of the corresponding cell. Due to absence of data, the lower altitude ("Grid > Bottom of layers (BOT)") of the model was calculated by subtracting from the surface elevation values (i.e. from the DTM) the predicted average thickness between the surface and the bedrock in the LLN area. Boundary conditions were then specified in "Grid > Cell status > IBOUND (MODFLOW)". The watershed and river shapes were imported in DXF format ("Option > Maps > Vector graphic") and displayed onto the grid (cf. Figure 13). Fluxes through the geographical boundaries of the catchment were ignored (set to zero) by assigning an "Ibound" value of "1" to all cells within the watershed boundaries (indicating active cells subject to water transfers and hydraulic head variations) and a value of "0" to all exterior cells, signifying inactivity and the absence of water flow.

Following that, modelling parameters were input. The simulation was configured as a "Steady-State flow simulation" with a simulation duration of 100 years (to ensure equilibrium starting from the initial state) using daily temporal discretization (1 day). This information was provided in the "Parameters > Time" tab. Subsequently, in the corresponding "Parameters" tabs, values for Initial hydraulic heads, horizontal hydraulic conductivity (K), and effective porosity (n_e) were filled in for each cell of the model (cf. Table 1). The latter two parameters correspond to the average values of the aquifer described in section 2.3.2.

Table 1 – Hydrogeological modelling parameters

Parameter	Parameter values	Converted values ([m] and [d])
Initial hydraulic heads	30 m below surface	/
Average hydraulic conductivity (see section 2.3.2)	$7.46*10^{-5}$ m/s (Anibas et al., 2016; Ruthy et al., 2017)	6.445 m/d
Effective porosity and Specific yield (see section 2.3.2)	0.0465 $m^3_{mobile\ water}/m^3_{total}$ (Dassargues & Walraevens, 2014)	/

b) Packages used

The selection of packages was conducted in "Models > MODFLOW (Flow Simulation) > Flow Packages."

Water recharge

The recharge of the model, assumed to be constant over time, was applied to the top of the grid. It was estimated under the assumption of zero stock variation (ΔS = 0 [m/d]) (EPFL, n.d.):

$$\underbrace{\Delta S}_{=0} = P - ET - R - \frac{Q}{S}$$

$$\Rightarrow \quad R = P - ET - \frac{Q}{S}$$

Where R is the recharge [m/d], P is precipitation [m/d], ET is evapotranspiration [m/d], Q is the discharge [m³/d] at the outlet, S is the (topographic) surface area [m²] drained by the watercourse (and its tributaries) upstream of the outlet. Parameter values are provided in Table 2, and evapotranspiration was estimated at 50% of precipitation, an average for Belgium (IRM, 2007). Consequently, recharge was estimated at 269.197 mm/y, or $7.375*10^{-4}$ m/d across the entire model.

Table 2 – Catchment parameters implemented in the packages

Parameter	Parameter values	Converted values ([m] and [d])
Average precipitation in LLN (P)	907.6 mm/y (Weather Spark, n.d.)	$2.487*10^{-3}$ m/d
Outlet discharge[5] (Q)	5.268 m³/s (Ministerie van de Vlaamse Gemeenschap, 1999; WATERINFO.be, 2023a)	455 134.78 m³/d
Catchment area (S)	899.9 km² (Ministerie van de Vlaamse Gemeenschap, 1999)	$899.9*10^{6}$ m²

River

The Dyle River was considered by specifying parameters related to the "River" package: head in the river (H_{RIV}) [m], elevation of the riverbed bottom (R_{BOT}) [m] and hydraulic conductance of the riverbed (C_{RIV}) [m²/d] (Chiang & Kinzelbach, 1998; Simcore Software, 2012).

Implemented values account for a river depth of 0.75 m (WATERINFO.be, 2023b), assumed constant along the entire river, and the riverbed is 1 meter thick. Thus, the river was positioned to represent the outcrop of the aquifer (Foglia et al., n.d.). Hydraulic conductance of the riverbed (C_{RIV}) [m²/d] was defined using the following equation (Chiang & Kinzelbach, 1998; Foglia et al., n.d.), assumed to be the same for each cell the river passes through:

[5] The discharge rate was calculated based on flow measurements collected over a five-year period (from 21/10/2018 00:00 to 20/10/2023 23:30) near the outlet of the modeled watershed (WATERINFO.be, 2023a). The measurement station is located slightly upstream, to the north of Leuven.

$$C_{RIV} = \frac{K * L * W}{M}$$

where:

- K is the hydraulic conductivity of the riverbed material, of 10^{-8} m/s, equivalent to 8.64 m/d (Ruthy et al., 2017; Shackelford, 2013).
- L is the length of the river within a cell [m], assumed to be 100 m.
- W is the width of the river [m], assumed to be 1 m along its entire length.
- M is the thickness of the riverbed [m], also assumed to be 1 m everywhere.

A value of 0.0864 m²/d was therefore utilized for cells affected by the river presence.

(Pumping) Wells

Given that LLN is an area where the groundwater body is significantly exploited (Ruthy et al., 2017) compared to the rest of the catchment area, and due to the difficulty in obtaining watershed-scale pumping data, it was assumed that the rest of the catchment is exploited on average at 20% of the pumping rate in LLN (where 1000 m³/d are pumped (Ruthy et al., 2017) for an area of approximately 10 km²), distributed across various extraction points (Ruthy et al., 2017). Therefore, a pumping rate of 0.2 m³/d was thus applied to all these cells.

c) Model calibration

To finalize the model, piezometric observations were incorporated through "Models > Modflow (flow simulation) > Head observations ". Information such as piezometer names, geographical coordinates, measurement time, observed water height (H_{obs}), and confidence weight in the data were encoded.

The chosen measurement time corresponds to the end of the modelling period (100 years) to ensure convergence. The average of all recorded water heights in LLN (Couly, 2022) and the average of the minimum and maximum values for other piezometers (Wallonie.be, 2023) were used. The weight was set to 1 as confidence in the data is high (Chiang, 2005). The complete list and information of the piezometers used for calibration can be found in Appendix 9.3. Used piezometers were selected based on their location, and only those situated in proximity to the centre of their cell were retained. In cases of multiple piezometers in one cell, only the central one was included.

Finally, in "Models > Modflow-2000 (Parameters estimations) > Simulation settings" (Chiang, 2005), the "hydraulic conductivity" parameter (and consequently, transmissivity) was optimized to converge toward the piezometric observations implemented in the model.

d) Results simulation and verification

The PCG2[6] package is used for solving the groundwater flow (in “Models > Modflow (flow simulation) > Solvers > PCG2”) (Bloemendal & Olsthoorn, 2018). The convergence criterion was set to 10^{-3} m for "Head change" and 10^{-3} m³/d for residuals.

Subsequently, the model was run, and the results were displayed (via “Tools > 2D-visualization”) and saved. The utilized results are titled "Flow right face", "Flow front face" and "Hydraulic head".

The matrices of "Flow right face", corresponding to the flow between the cells [J, I, K][7] and [J+1, I, K] (i.e., to the cell in the next column on the same row), and "Flow front face", corresponding to the flow between the cells [J, I, K] and [J, I+1, K] (i.e., to the cell in the next row in the same column) (Simcore Software, 2012) were saved to be used in the LLN model presented below.

The "Hydraulic head" was used to analyse and verify the overall results of the model. For this purpose, the hydraulic head matrix was exported to calculate the thickness and depth of the water table across the entire watershed. The map created by Modflow was also compared to the piezometric map of the area (Wallonie.be, 2006) (Figure 34 in Appendix 9.4) and to the results of Dominique Fasbender's thesis (Fasbender, 2008) (Figure 35 in Appendix 9.4). He predicted the water over a part of the watershed using the Bayesian data fusion approach.

4.2.2. Hydrogeological model focused on Louvain-la-Neuve

a) Model setup

The modelling resolution for this model was set at 10 meters. It consists of a single layer, is bound by the surface and the bedrock (whose altitude was predicted in the lithostratigraphic model), and shares the same values for hydraulic conductivity and porosity parameters (refer to Table 1). The total modelling duration remains the same to achieve equilibrium from the initial hydraulic head, which is also set at 30 meters below the surface. However, this model operates under transient flow conditions, and the Specific Yield value has been specified.

[6] Preconditioning Conjugate Gradient Package 2

[7] "J" corresponds to columns, "I" to rows, and "K" to layers (Chiang & Kinzelbach, 1998). Therefore, [J, I, K] corresponds to [x, y, z].

b) Packages used

Water recharge

At the study area scale, recharge calculation considers precipitation and evapotranspiration (Ruthy et al., 2017):

$$R = P - ET$$

For this model, the recharge value is $1.243*10^{-3}$ m/d.

Wells

The extracted volumes from the four water extraction points located in LLN, used for public distribution, have been considered. These extractions are assumed to be constant over time and are detailed in Table 3 (Ruthy et al., 2017), sorted by decreasing flow. However, this table only includes extractions greater than 3 000 m³/y) (Ruthy et al., 2017), making it incomplete.

Table 3 – Extracted volumes for public distribution in LLN in 2014 (Ruthy et al., 2017)

Name of the extraction wells	Location	Annual pumped flow (in 2014) [m³/y]	Daily flow pumped [m³/d]
S49	"Bois de Lauzelle"	219 642	601.76
S40	"Parc de la source"	110 244	302.04
S19	"Cyclotron"	28 745	78.75
S29	"Place Ste-Barbe"	15 657	42.90

The results from the matrices "Flow right face" and "Flow front face" of the simplified catchment model were used to determine the inflow or outflow in this detailed LLN model. These lateral flows were simulated by adding wells along the entire perimeter of the model (USGS, n.d.-b). The injected or extracted volume for each cell was calculated by dividing the fluxes from the corresponding cells in these matrices by 10, to take account of the change in grid size. Taking into consideration these lateral flows allow for the incorporation of external influences on the model, including hydraulic head, gradient, and flow velocity.

c) Model calibration

The average of all hydraulic head observations for each piezometer (Couly, 2022) was used as a reference to calibrate the model. The complete list and information of the piezometers used for calibration can be found in Appendix 9.3. The same methodology was applied as in the case of the simplified model at the catchment scale (cf. section 4.2.1.2), involving the optimization of hydraulic conductivity to converge towards these observed values.

d) Results simulation and verification

The same solver as for the watershed model was used, following the same convergence criteria. The "Hydraulic head" of the model was then downloaded, enabling the calculation of groundwater thickness and depth for result verification.

4.3. Heat transfer modelling

After completing the hydrogeological representation of LLN, the MT3DMS model, available in Processing Modflow ("Models > MT3DMS"), was employed to simulate thermal energy transfer.

In the "Simulation settings", it was specified that the simulation mode operates at constant density, and that no kinetic reactions are involved. The initial temperature of the groundwater, i.e. 11°C (cf. section 2.3.2), was encoded in the "Initial concentration" tab. The Finite Difference Method was utilized for the advection package to simulate heat transport, with a courant number[8] of 0.75 (Chiang & Kinzelbach, 1998). In the dispersion tab, TRPT[9], le TRPV[10] and longitudinal dispersivity were specified (Simcore Software, 2012) based on characteristic values of transverse dispersivity (α_T) and longitudinal dispersivity (α_L) of the aquifer (cf. section 2.3.2). The temperature of cells corresponding to injection wells and Constant Head cells (i.e., when Ibound = "-1") was specified in "Sink/Source concentration". A temperature identical to the groundwater temperature (i.e. 11°C) was set for injection wells on boundary cells (simulating lateral supply of water in the groundwater body) and Constant Head cells, while the temperature of injection wells for ATES systems depends on scenarios.

Different models were created, starting with a preliminary simple verification to ensure the model's proper functionality, followed by general tests over the entire study area, and finally, a realistic modelling of an ATES system for the BSC. Results were obtained in "Tools > 2D-Visualization > MT3DMS".

4.3.1. Verification of MT3DMS operation

Initially, simple cases were created to test and verify that the MT3DMS model was producing the expected results. The models had LLN characteristics, but no recharge, extraction well, or other lateral wells were modelled. In the first tested case, the ground surface, the aquifer bottom, and the initial hydraulic head were horizontal, representing a stationary case without any natural water flow. In the second tested case, an average gradient similar to that of LLN calculated in the model described in section 4.2.2 was imported for the Initial hydraulic head to account for the natural flow of the groundwater.

[8] The “Courant Number” represents the number of cells a particle will be allowed to move in one transport step, typically between 0.5 and 1 (Chiang & Kinzelbach, 1998).

[9] Ratio of the horizontal transverse dispersivity to the longitudinal dispersivity

[10] Ratio of the vertical transverse dispersivity to the longitudinal dispersivity

Moreover, these scenarios were run twice, once with, and once without specifying that the cells at the model's border have constant head cells.

In the third test case, warm water injection wells were installed as control points, and pumping wells were placed near some of them at different distances.

4.3.2. Study of energy transfer across the entire study area

The second step was to create models representative of the groundwater flow situation in LLN to study heat transfer in the study area. Different situations were implemented.

1. In the first one, heat injection wells were placed at regular intervals across the entire area.
2. Subsequently, the influence of UCLouvain extraction well was studied by placing injection wells around each of them.
3. A third situation focused on energy injection at major buildings, especially the sport centre and auditoriums.
4. Finally, a model allowed the study of installing two parallel storage lines (one hot and one cold) for three buildings.

4.3.3. Implementation of a realistic ATES system for the Blocry Sport Centre

The study of a realistic ATES system for the Blocry Sport Centre involved creating four models (one per season), each lasting 91 days, launched successively based on the results of the previous model.

1. In the first model representing summer, the system was operated at 100 m^3/d (both for pumping and injection), the initial water table was pumped at a temperature of 11°C and the injection temperature was set at 20°C.
2. The second model, without any wells, representing the offseason period and simulating the flow of the created thermal plume.
3. The third model, representing winter, pumped the heat injected in the first model (at the same discharge rate of 100 m^3/d) and injected cold water at 5°C.
4. Finally, the offseason flow model was launched a second time.
1. After that, the 1st summer model was started again, pumping cold water injected in the 3rd model instead of the initially 11°C water table.

The search for the optimal zone to install the pumping well was done in two steps, knowing that the injection was done next to the Blocry parking near the BSC (precisely at coordinates

X=166610m and Y=151160m). First, the search area was visually identified based on the grid where the thermal plume remained the warmest (for summer) throughout the pumping period. This area was then narrowed down by comparing the average temperatures of the pumped water for different well locations. The search stopped when the average temperature varied little from one cell to another, so the exact optimal cell might not have been found.

The average pumped water temperature ($\bar{T}$) was calculated by looking into the "OUTPUT.MTM" text file, automatically generated during the MT3DMS software model runs. The file contains information such as the total energy pumped and injected by all wells in the model throughout the modelling duration (of 91 days). The specific energy pumped by the downstream well of the ATES system was determined by comparing the total amount of energy pumped by all the wells in the 3rd model to the energy pumped in a reference situation without any ATES system (similar to the 2nd model). This difference, aiming to neutralize the effects of extraction wells and boundary cells simulating the lateral water inflow or outflow, was then divided by the flow rate of the ATES well and the modelling duration to obtain the average temperature of the pumped water.

The efficiency was calculated by comparing the pumped thermal energy to the initially injected energy, comparing only the average temperature of the pumped water ($\Delta\bar{T}_{out}$) to the injected one ($\Delta\bar{T}_{out}$) when the pumped and injected volumes are identical (Bloemendal & Olsthoorn, 2018).

$$\eta(t_0 \rightarrow t) = \frac{E_{out}}{E_{in}} = \frac{\int_{t_0}^{t} \Delta T_{out} * Q_{out}\, dt}{\int_{t_0}^{t} \Delta T_{in} * Q_{in}\, dt} = \frac{\Delta\bar{T}_{out} * V_{out}}{\Delta\bar{T}_{in} * V_{in}}$$

Two efficiency values were calculated. First, the efficiency of the distinct thermal plumes (i.e., hot or cold lines) was calculated by comparing the average temperature of the pumped water to that injected 6 months earlier, knowing that the water is initially at 11°C.

$$\eta_{flow\ line}\ [\%] = \frac{\bar{T}\ pumped\ -\ 11°C}{T\ injected\ -\ 11°C}$$

Next, the efficiency of the complete cycle of the system was calculated by comparing the temperature change related to heating the water (i.e., in summer to go from pumped chill water to injected warm water (20°C) and cooling the water to recover energy (i.e., in winter to go from pumped lukewarm water to injected cold water (at 5°C)).

$$\eta_{complete\ cycle}\ [\%] = \frac{\bar{T}\ winter\ pumped - \bar{T}\ winter\ injected}{\bar{T}\ summer\ pumped - \bar{T}\ summer\ injected}$$

The overall efficiency of a system cycle was determined by considering the average temperature recovered for both the warm and cold parts. Consequently, the models had to be

run a second time, starting with the injection of cold water in the first model and then warm water in the third model. This is akin to initiating the modelling process at the beginning of winter (i.e., with the 3rd model described earlier) and then following the logical order of the models (i.e., 4th, 1st, 2nd, etc.).

Finally, a sensitivity analysis was conducted by studying different scenarios. Injection rates and the temperature of warm water injection were modified (one parameter at a time) to study the impact of these variations. The summer injection temperature was set to 15 and 25°C, and the flow rate was set to 50 and 200 m^3/d.

5. Results

5.1. Required volumes of thermal storage materials

As mentioned in section 2.1, the objective of storage is to store a portion of the energy consumed by the sport centre. Therefore, the goal is to store surplus thermal energy available in summer for use in winter, ultimately reducing primary energy consumption. Various storage options are possible: Thermochemistry Energy Storage (TCES), Latent Heat Storage (LHS), and Sensible Heat Storage (SHS), offering storage capacities of 1000 MJ/m³, 300 to 5000 MJ/m³, and 100 MJ/m³, respectively. The Table 4 illustrates the necessary storage volume for these technologies at various proportions of the BSC's annual consumption. To provide a comparative perspective, the required storage volume is also expressed in terms of the size of a cube with the appropriate capacity.

Table 4 - Required storage volumes for different proportions (%) of the annual total BSC's consumption according to different storage technologies (TCES: Thermochemistry Energy Storage, LHS: Latent Heat Storage, SHS: Sensible Heat Storage)

[-]	Amount of energy to store		Volume of stored energy [m³][11]			Size of a cube with the corresponding capacity [m]		
%[12]	[MWh]	[GJ]	TCES	LHS	SHS	TCES	LHS	SHS
-	1	3.6	3.6	7.2 - 12	36	1.53	1.93 – 2.29	3.30
100	5 000	18 000	18 000	36 000 – 60 000	180 000	26.21	33.02 – 39.15	56.46
50	2 500	9 000	9 000	18 000 – 30 000	90 000	20.80	26.21 – 31.07	44.81
20	1 000	3 600	3 600	7 200 – 12 000	36 000	15.33	19.31 – 22.89	33.02
10	500	1 800	1 800	3 600 – 6 000	18 000	12.17	15.32 – 18.17	26.21

The sports complex demands substantial storage capacities for the energy it consumes, as detailed in Table 4. Even for a modest energy storage proportion, such as 10% of the total consumption, the volume needed corresponds approximately to a cube with sides of 12 m for thermochemical storage, 15 to 18 m for latent heat, and over 26 m for sensible heat, which is substantial.

[11] Calculated on the basis of the amount of energy stored by each of the existing systems (thermochemical storage (1000 MJ/m³), latent heat storage (300 and 500 MJ/m³) and sensible heat storage (100 MJ/m³)).

[12] Percentage of the average annual consumption of the BSC to be stored.

5.2. Choice of the Thermal Energy Storage system

Selecting an appropriate Thermal Energy Storage (TES) system is important. Considering the substantial amount of energy requiring storage (cf. section 5.1), above ground storage is inappropriate, making underground storage the preferred choice. Both Tank Thermal Energy Storage (TTES) and Pit Thermal Energy Storage (PTES) systems are excluded due to their complexity and high implementation costs. The decision to opt for an open system is influenced by the necessity to handle large volumes.

In this context, the presence of the groundwater body beneath LLN is advantageous, enabling the consideration of Aquifer Thermal Energy Storage (ATES) and Borehole Thermal Energy Storage (BTES) systems, as described in section 2.2.2.2. Since BTES systems require the storage water to be as immobile as possible, and the groundwater is flowing (towards the north) (cf. section 2.3.2) the more efficient and viable choice is the ATES system.

5.3. Lithostratigraphic model

5.3.1. Databases of geological layers topography

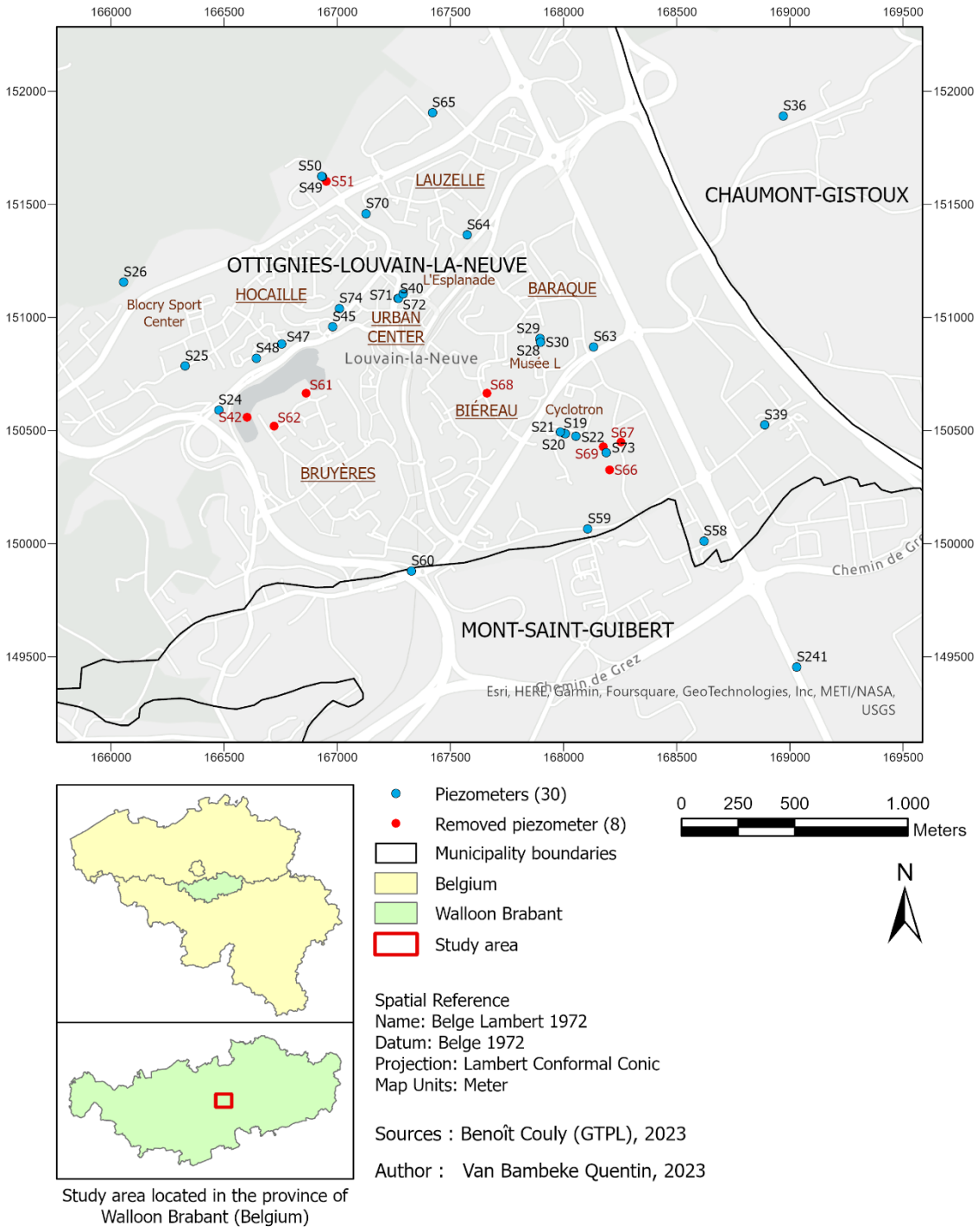

Figure 4 - Location of piezometers managed by the GTPL department of UCLouvain

The map displayed in Figure 4 provides an illustration of the area. The study area covers approximately 8 km², which is slightly larger than the area encompassing all the piezometers.

The BSC is situated near the western edge of the study area, with two nearby piezometers: S25 and S26.

The piezometers considered in the present study are shown in blue, while the piezometers excluded due to inaccurate data are shown in red. Figure 4 reveals that some of the excluded piezometers are located close to other piezometers for which data can be used (S42, S51, S66, S67 and S69), while others are located much further away (such as S61, S62, and S68). Figure 4 also reveals that in certain locations, several retained piezometers are very close to each other (S19, S20-S21-S22, S28-S29-S30, S49-S50, and S40-S71-S72).

5.3.2. Geological layer thickness and altitude prediction

5.3.2.1. Measured data

Figure 5 below presents the initial thickness data, with consistent scales across all figures for ease of comparison.

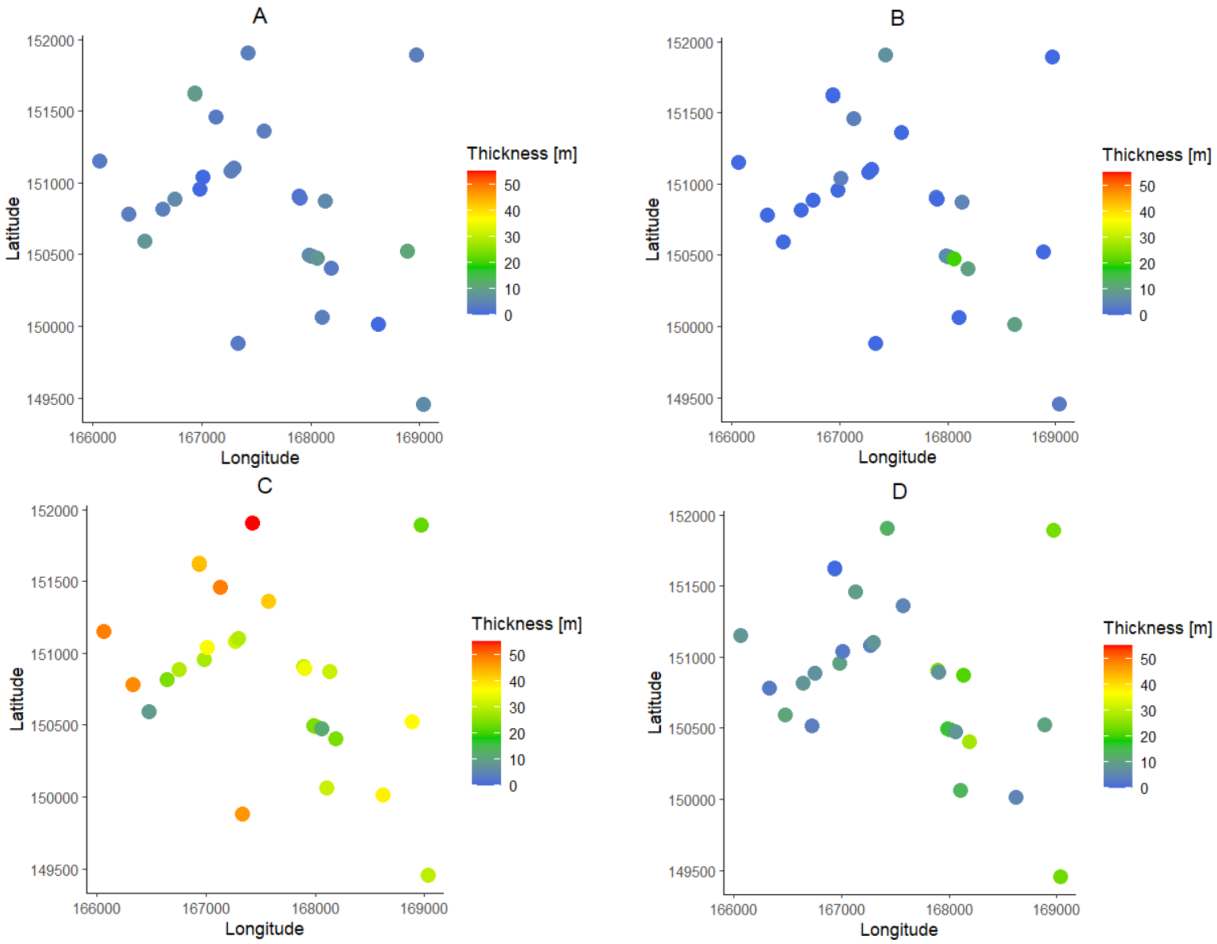

Figure 5 - Thickness of geological layers (A: Quaternary, B: Tongrian, C: Bruxellian, D: Landenian). The locations corresponding to the longitude and latitude coordinates can be found in Figure 4.

A slight gradient in layer thickness values is observed, reflecting global trends among piezometers in proximity but evolving with distance. Several key observations arise from these data:

1. Substantial variations in layer thickness are evident between different layers, with the Bruxellian layer consistently appearing as the thickest, with a few exceptions.
2. Within the same geological layer, many measured thickness values appear to be quite similar. For the Quaternary layer, Figure 5 illustrates a dominant thickness slightly below 5 meters. The Tongrian layer is often absent (zero thickness), while the Landenian layer thickness tends to be around 10 meters. Notably, the Bruxellian layer stands out as the only layer with significant variability in measured thickness among piezometers, since several thickness values are present in similar proportions.
3. It is not uncommon for thickness measurements at one piezometer to vary significantly from those of neighbouring piezometers. Figure 5 highlights instances where a point deviates from its close neighbours, particularly noticeable in the groups of piezometers S19, S20, S21, and S22.

5.3.2.2. Thickness residuals calculation and outliers identification

The results of the calculation of thickness residuals, obtained by subtracting the linear trend from the initial data, are presented in Figure 28 (available in Appendix 9.2.2.1). Then, the identification of outliers in the calculated residuals was performed using Boxplots for which Figure 6 illustrates the obtained results. The bold line representing the median value is close to 0 m for each Boxplot. The interquartile range (IQR), which represents the spread of the middle 50% of the data, is smaller for the Quaternary and Tongrian layers compared to the Landenian and, especially, the Bruxellian. This pattern extends to the lower and upper limits of the boxplots.

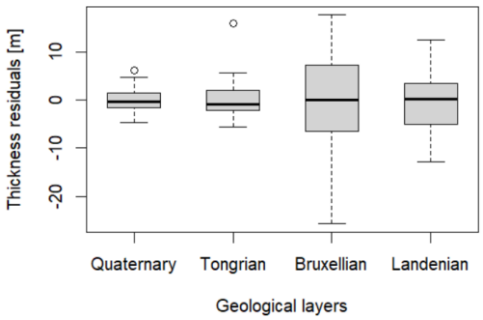

Figure 6 - Boxplots of thickness residuals for each geological layer

Two outliers are identified: one for the Quaternary layer and one for the Tongrian layer. The Quaternary outlier is near the upper limit of the Boxplot, while the Tongrian outlier is more significant. No outliers were detected for the Bruxellian or Landenian geological layers.

5.3.2.3. Variogram models

Table 5 presents the model parameters used to construct variograms for each geological layer. The obtained variograms are depicted in Figure 7.

The "Psill" parameter is a semi-variance parameter [m²] which corresponds to the value of the plateau (horizontal part of the graph) reached by the chosen model. This value is added to the nugget effect of the nugget model when the two are combined.

The "Range" represents the model's range, indicating the distance [m] between pairs of points at which the data (in this case, the residuals of layer thickness) can be considered independent. The range of a nugget effect is zero since predicting a nugget value from another point is impossible.

The "Nugget" corresponds to the value at which the variogram intercepts the y-axis, in other words, when the distance between points is 0. A value of 0 suggests the expectation of finding precisely the same values for the same location, as the semi-variance is zero. Conversely, a non-zero value indicates the presence of a chance effect, with variance occurring even when the distance between points is 0.

Table 5 - Model parameters obtained for the different variograms

Geological layers	Model used	Parameter values		Nugget effect values	
		Psill [m²]	Range [m]	Psill [m²]	Range [m]
Quaternary	Exponential	7.71	97.67	0.00	0
Tongrian	Exponential	8.75	193.18	0.08	0
Bruxellian	Spherical	101.88	1596.36	30.62	0
Landenian	Exponential	521.10	19559.47	27.88	0

The Quaternary and Tongrian have a very low Psill and Range values (cf. Table 5) for their model and a very low nugget effect (even absent for the Quaternary). The variogram function (black line in Figure 7) is relatively close to the variance of the datasets (represented by the red dotted lines), although the Quaternary variance slightly exceeds it.

The Bruxellian has larger Psill and Range values, and the Landenian even more: the model range for the Landenian is almost 20 km compared to 1600 m for the Bruxellian. In addition, the variogram function (black line in Figure 7) significantly surpasses the variance of the datasets (red dotted lines) in both cases.

It is essential to note, as shown in Figure 7, that a considerable number of points are not well represented by the modelled variogram curve.

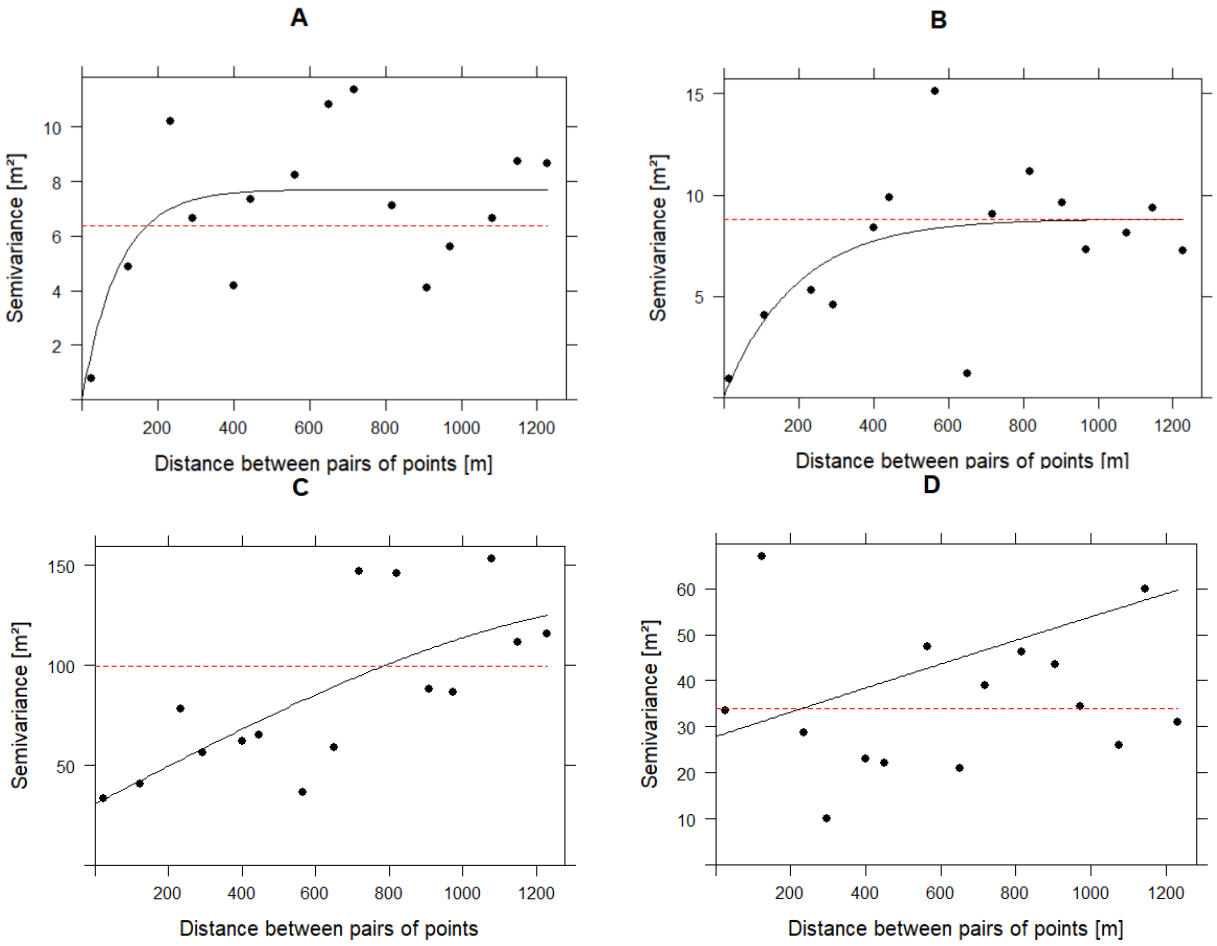

Figure 7 - Modelled variograms of residuals in the geological layers studied (A: Quaternary, B: Tongrian, C: Bruxellian, D: Landenian)

5.3.2.4. Residuals prediction

Kriging was employed to predict residual thickness values on a 10m grid size, along with their associated variation as an assessment of indicating the quality of the prediction. The geographical boundaries of the prediction grid are defined by 166 000 m to 169 050 m on the abscissa and 149 400 m to 152 000 m on the ordinate, corresponding to the minimum limits to encompass the entire set of data points (cf. Figure 4).

Figures corresponding to the predicted values were omitted since they closely resemble to the thickness values presented below (cf. section 5.3.2.5), differing only in the absence of the trend. Therefore, only the variance related to the residuals predictions is discussed: the results are shown in Figure 8, and the extreme values are provided in Table 11 (available in Appendix 9.2.2.1).

Figure 8 shows that for the Quaternary and Tongrian layers, the variance is low in proximity to the piezometers (around 5 m²) and slightly higher but consistent elsewhere (8 and 9.4 m² for the Quaternary and Tongrian, respectively - see Table 11 (in Appendix 9.2.2.1)). In contrast, for the Bruxellian and Landenian layers, the variance is high even near the piezometers (exceeding

30 m² - see Table 11 (in Appendix 9.2.2.1)) and increases with distance from the piezometers. Notably, the maximum variance is quickly reached for the first two layers, unlike the two subsequent layers.

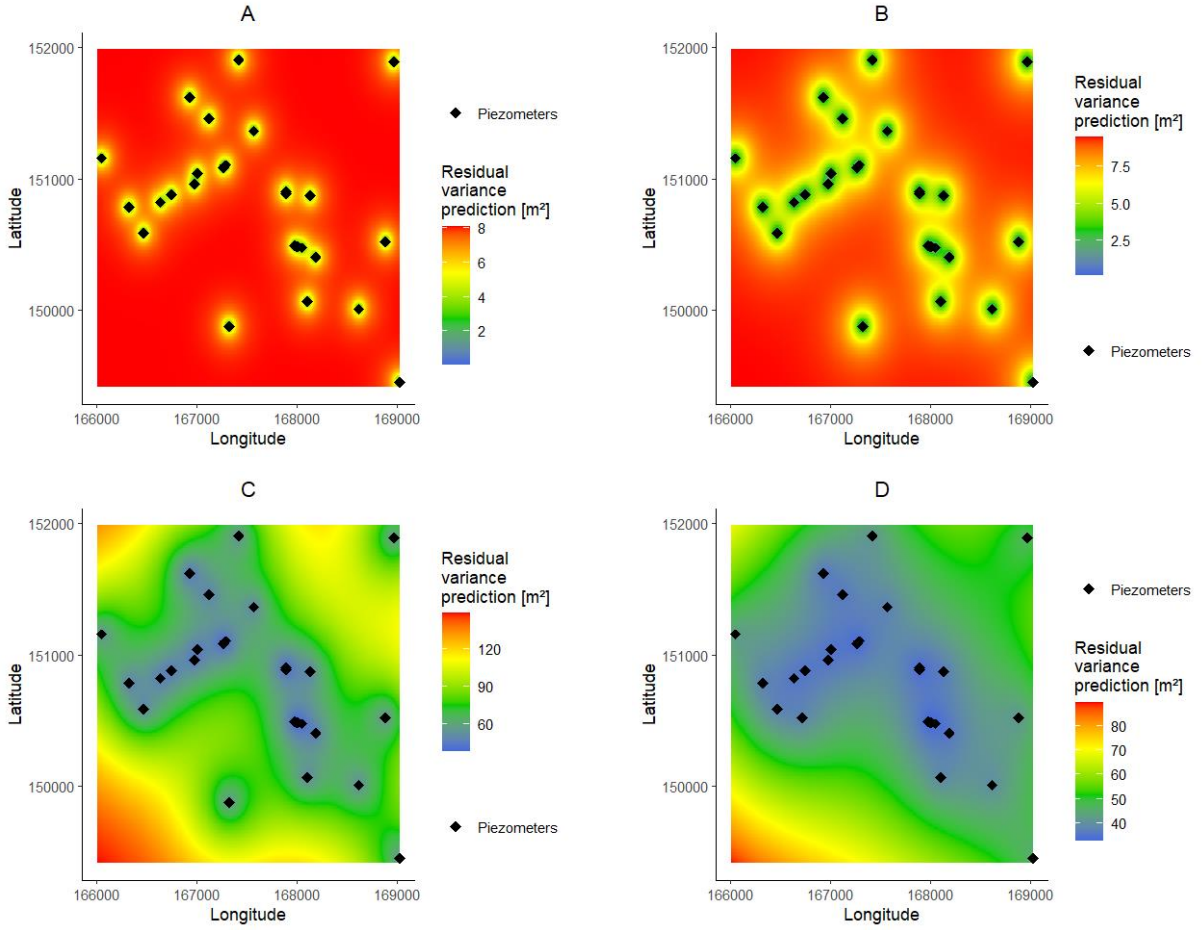

Figure 8 - Variance of the predicted residuals. The locations corresponding to the longitude and latitude coordinates can be found in Figure 4.

5.3.2.5. Calculation of geological layer thickness

The final step involved predicting thickness at all grid points by adding back the previously removed linear trend into the predicted residuals. Results are shown in Figure 9 (and Table 6). The scales of values used in the figures differ intentionally, facilitating a clear observation of thickness variations, especially in the thinner layers.

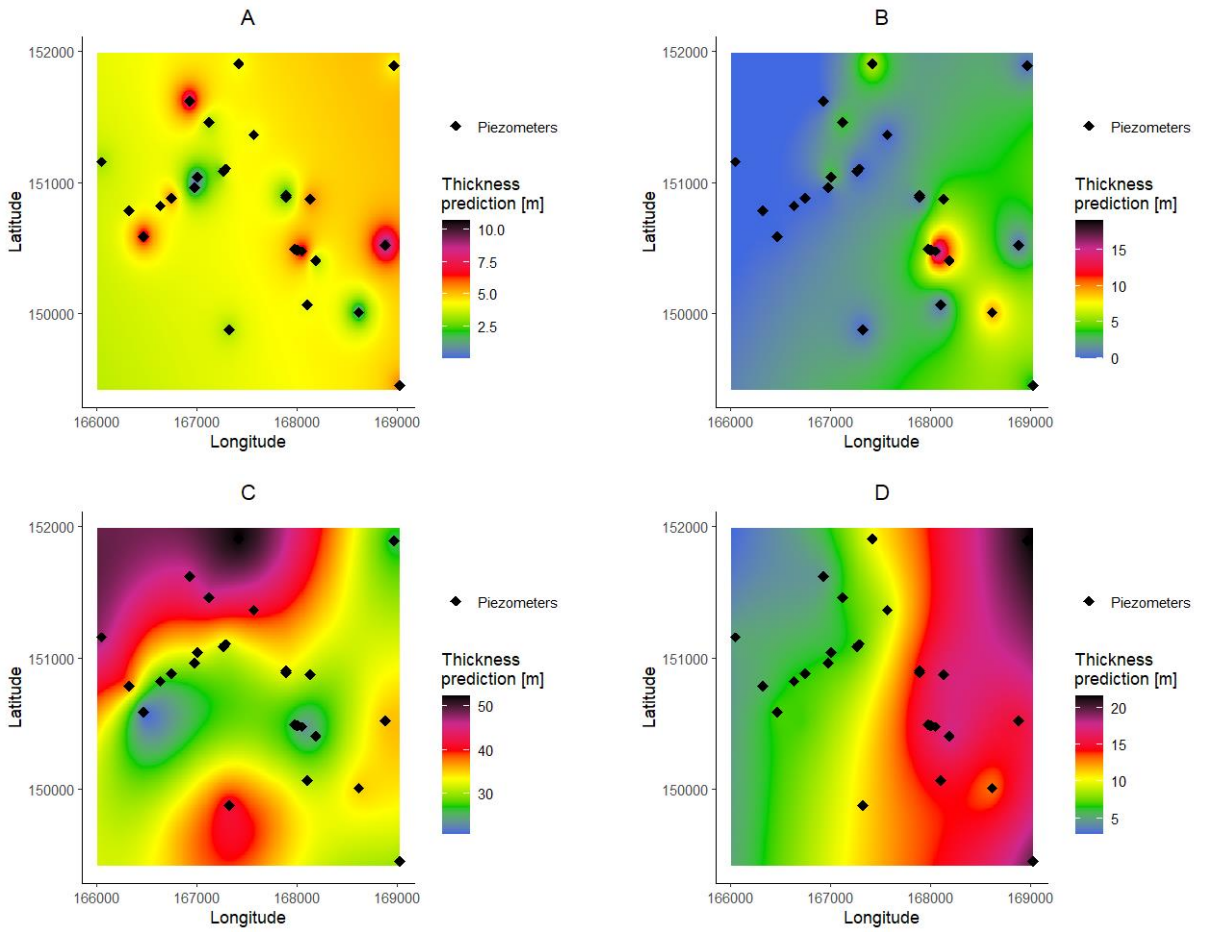

Figure 9 - Thickness prediction for the different layers (A: Quaternary, B: Tongrian, C: Bruxellian, D: Landenian). The locations corresponding to the longitude and latitude coordinates can be found in Figure 4.

Table 6 - Extreme values of the thickness and altitudes predicted on the prediction grid

Geological layers	Predicted thickness [m]		Predicted altitudes [m]	
	Min	Max	Min	Max
Quaternary	0.38	9,50	72.72	152.98
Tongrian	0.00	15,92	68.76	148.71
Bruxellian	21.13	52,19	68.76	144.23
Landenian	2.79	21,65	19.42	111.41

Figure 9 reveals that the Quaternary layer maintains a relatively constant thickness across the whole study area, with the most extreme thickness values near the piezometers. The Tongrian layer, however, displays a slight gradient of thickness that increases from west to east. Notably, the Tongrian layer is non-existent in the western area due to predicted negative values (up to -2m) that were replaced by 0. Thicknesses of the Bruxellian and Landenian layers show significant variations based on location, with the Bruxellian layer being thicker. The Bruxellian layer is thinnest in the centre and increases in thickness towards the north and south, while the Landenian layer is very thin in the west and gradually increases in thickness towards the east.

5.3.2.6. Calculation of geological layer altitude

The altitude given by the DTM measured by Lidar is shown in Figure 10. It is ranging between 72.72 meters and 152.98 meters.

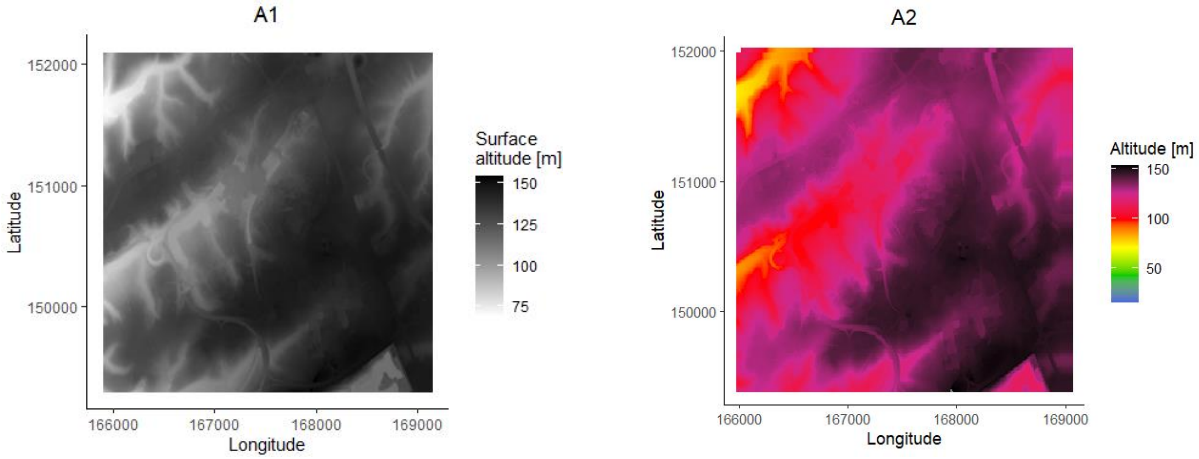

Figure 10 - Altitude surface transformation (A1: DTM data, A2: Quaternary (top interface) altitude). The locations corresponding to the longitude and latitude coordinates can be found in Figure 4.

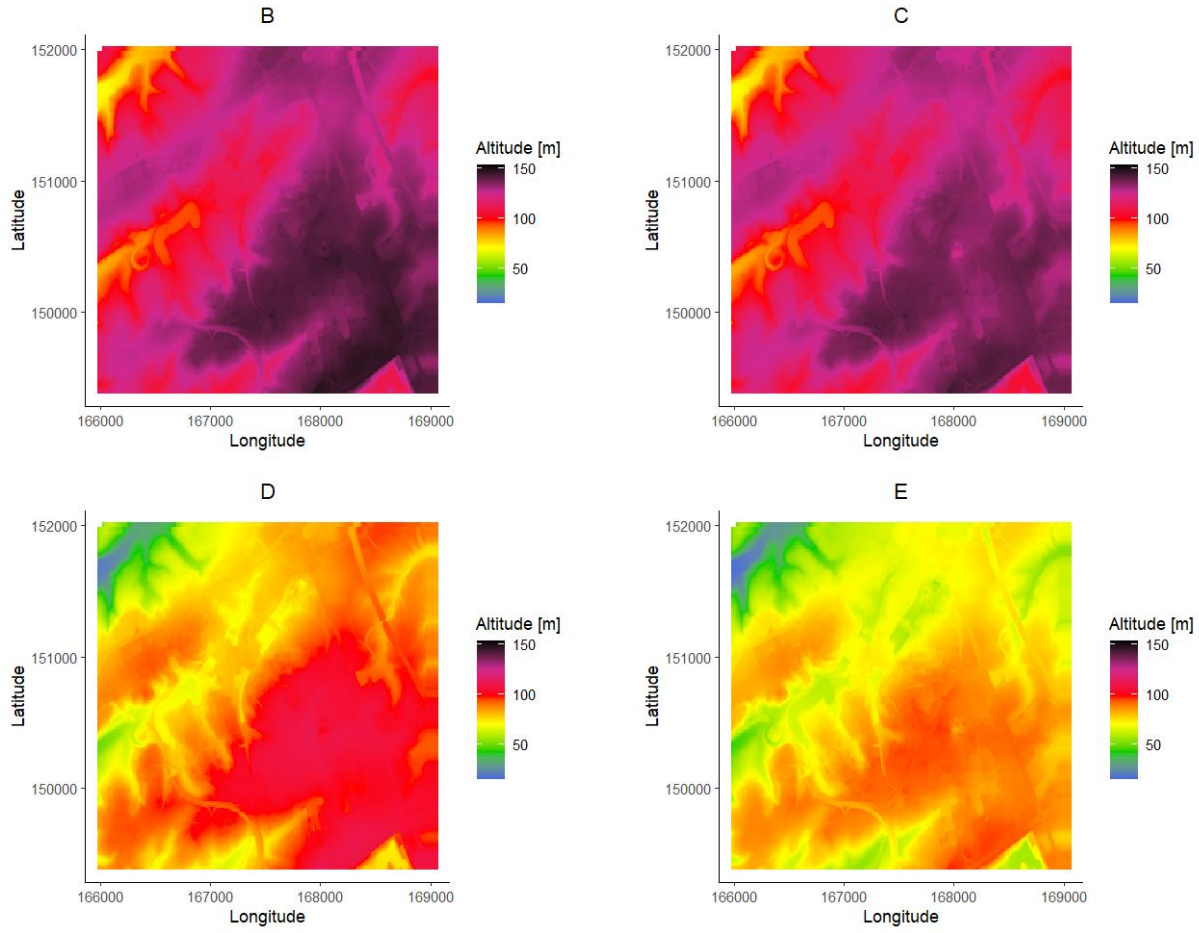

Figure 11 - Altitudes of the geological layers (B: Top of Tongrian, C: Top of Bruxellian, D: Top of Landenian, E: Top of Bedrock). The locations corresponding to the longitude and latitude coordinates can be found in Figure 4.

Figure 11 illustrates the altitudes of each layer, separated by the thickness values shown in Figure 9. Hence, the similarity in altitude on the west side of the Tongrian and Bruxellian layers is a result of this phenomenon. The most significant change in altitude occurs between the Bruxellian and Landenian layers.

Despite thickness variations across locations (cf. Figure 9), the altitude profiles remain similar for all layers, including the deeper ones, as evidenced in the repeated patterns in each layer's images in Figure 11.

5.3.3. Calculation of the prediction quality by Leave-One-Out Cross-Validation

5.3.3.1. Uncertainty on thickness prediction

An analysis of the LOOCV prediction's quality was performed for both layer thickness and geological layer altitude. Since only altitude will be used in the following parts of this work (i.e. Modflow modelling), the thickness statistics can be found in Appendix 9.2.2.2.

5.3.3.2. Uncertainty on altitude prediction

Plots comparing predicted and measured altitudes are shown in Figure 29 of Appendix 9.2.2.1. Additionally, the difference between the known and the predicted data for each piezometer are plotted in Figure 12. In this figure, a positive difference in altitude indicates a predicted elevation that is higher than the measured value.

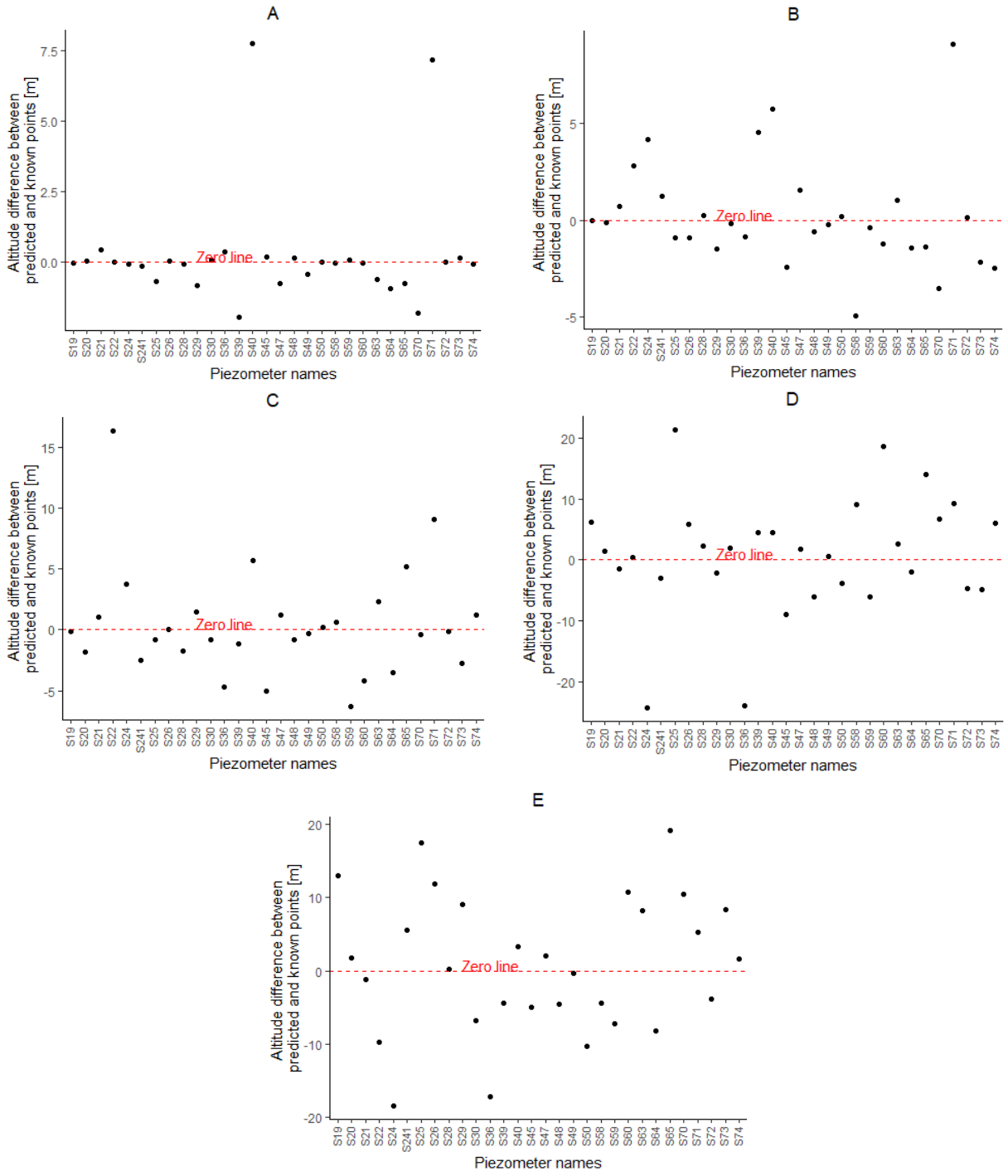

Figure 12 - Difference between predicted and known altitudes of each layer per piezometer (A: Quaternary, B: Tongrian, C: Bruxellian, D: Landenian, E: Bedrock)

The predicted altitude of piezometers S40 and S71 is about 7.5 m above the measured one in Figure 12 and in Figure 29 (Appendix 9.2.2.1). These piezometers are located under the concrete slab at Louvain-la-Neuve (cf. Figure 4), stand out as notably higher than others. Figure 12 also shows that the prediction gradually degrades for deeper geological layers. In the case of piezometers S25 and S26, located near the BSC, the difference reaches approximately 20 m and 10 m, respectively, indicating that the predicted altitude is too high.

Table 7 - Prediction quality statistics for the altitude of the top of the geological layers (all data)

Geological layer	RMSE [m]	R^2	SSE [m^2]
Quaternary	2.03	0.99	122.97
Tongrian	2.78	0.97	231.18
Bruxellian	4.37	0.91	573.22
Landenian	9.63	0.69	2778.93
Bedrock	9.31	0.57	2600.17

Table 7 summarizes the prediction statistics that represent the difference between the measured altitude (piezometer data files) and the predicted values. The R^2 is close to 1 (i.e. almost perfect) for Quaternary layer and decreases progressively with depth, reaching 0.57 for the Bedrock layer. The coefficient of determination is not equal to 1 because it compares data from the piezometer data files to the DTM (which serves as a prediction). The RMSE and SSE increase with depth, except for the bedrock, where the error is slightly lower than for the Landenian.

These results show that the errors for different piezometers vary from one layer to another. Different cases can be considered:

The error can remain similar for all layers, as observed for example for piezometers S21, S47, or S49, where the error remains very close to 0 for all layers (Figure 12). In this case, the altitude difference of the previous geological layer is transmitted from layer to layer.

The error for a given piezometer may change from sign from one layer to another. For example, piezometer S24 shows positive errors in the first layers and negative error from the Landenian onwards.

The error can also increase slightly from layer to layer. This occurs when the thickness prediction error is consistently of the same sign.

By excluding outlier point (i.e. S39 for the Quaternary and S22 for the Tongrian layer) as well as the two piezometers located under the concrete slab (S40 and S71), the LOOCV statistics are given in Table 8.

The values in Table 8 are better than those in Table 7, especially for the first 2 geological layers, with marginal improvement in the underlying three layers. However, some statistical parameters for the deepest layers are worse than those with outliers (underlined in Table 8).

It should be noted that some statistical parameters are worse than those with S40 and S71 piezometers for the deepest layers (these are the ones underlined in Table 8). It's noteworthy

that SSE values are not directly comparable with Table 7 due to fewer points being considered, resulting in a smaller total error.

Table 8 – Prediction quality statistics for the altitude of the top of the geological layers (without outliers)

Geological layer	RMSE [m]	R^2	SSE [m^2]
Quaternary	0.53	1	7.51
Tongrian	2.00	0.99	107.72
Bruxellian	4.05	0.92	458.35
Landenian	9.77	0.69	2672.32
Bedrock	9.57	0.57	2561.79

5.4. Hydrogeological model of the watershed

Figure 13 illustrates the implemented regional model and predicted hydraulic head (with piezometric height resolution of 5 meters). A grid size of 100 meters was chosen to provide sufficient spatial resolution for a gradual variation in the model's hydraulic head, ensuring accurate prediction quality without excessive computational demands. The catchment area boundaries do not align with the aquifer limits but are distant enough from LLN to assume no significant impact on flows within the study area.

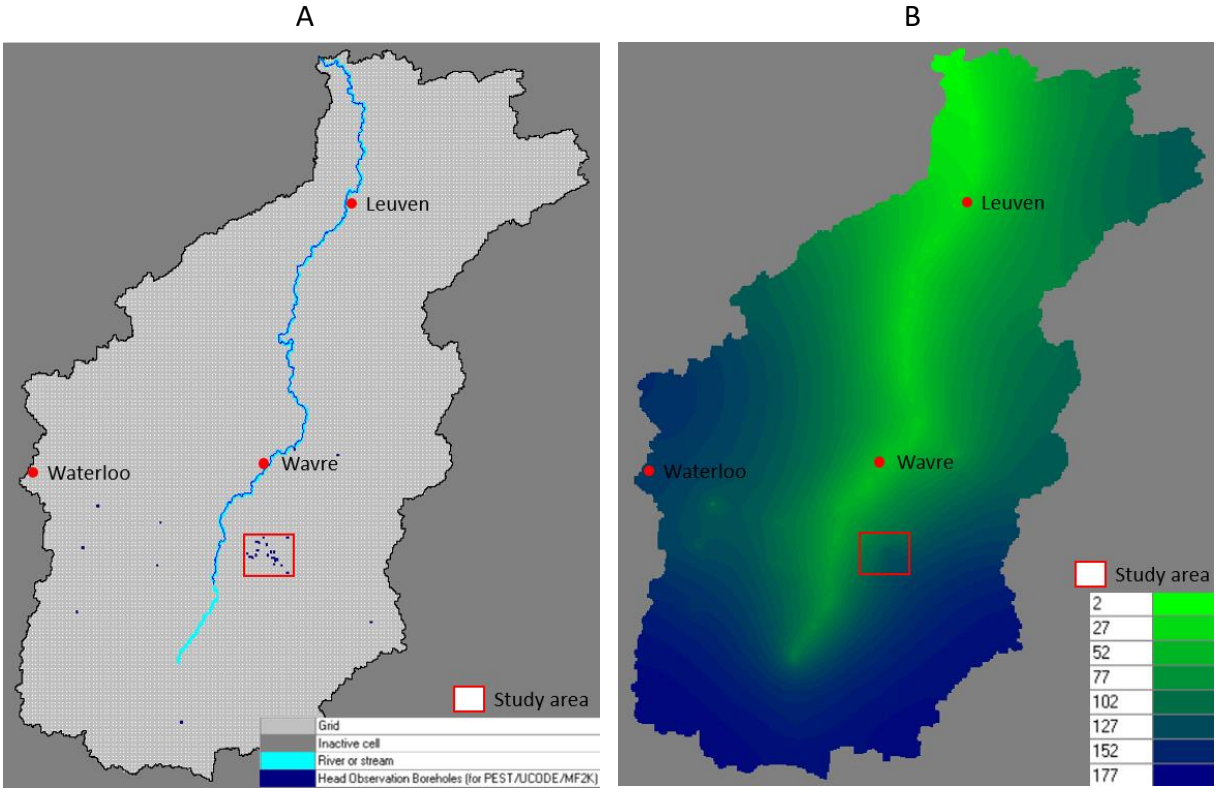

Figure 13 – Model diagram (A) and hydraulic head (altitude of the top of the water table) [m] at the catchment scale (B)

Figure 13 shows the considered watershed as considerably larger than the study area, with the Dyle river traversing the watershed's centre. Additionally, all piezometers used for model calibration (also known as "Head Observation Boreholes" in Figure 13) are located in the Southern (upstream) half of the watershed, with a significant concentration in the LLN area. The hydraulic head result indicates a general water gradient from South to North and from the edges towards the draining Dyle river, with piezometric curves parallel to the river. The Dyle represents the region with the lowest hydraulic head, although it exhibits continuous vertical fluctuations depending on location. When few piezometric observations are available in a subregion, the model predicts hydraulic head that tends towards the regional mean. This causes the hydraulic head to be biased in the surroundings of the piezometers of these subregions. This is clearly visible for piezometers located near Waterloo.

More details on the regional model, centred on LLN are given in the Appendix 9.4, which contains piezometric maps of the area available for comparing the results.

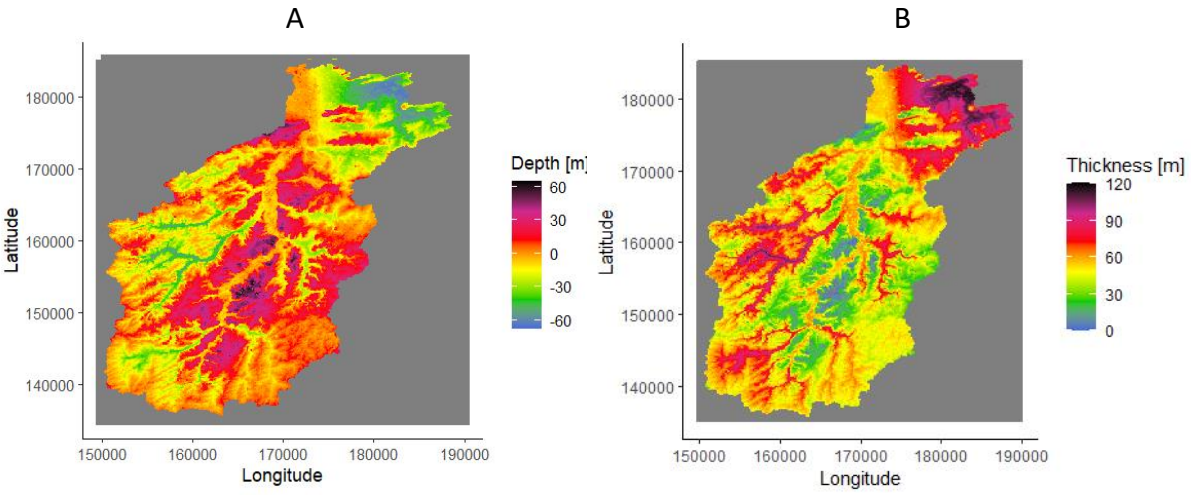

Figure 14 - Water table depth (from the surface) (A) and groundwater body thickness (B) at the catchment scale

Figure 14 presents the depth of the top of the groundwater layer from the ground surface and thickness of this groundwater body across the entire watershed. Negative depths indicate water levels above the ground surface, observed mainly in the Northern part of the watershed, far from LLN, and in what appears to be valleys or beds of secondary rivers (that were not modelled) on the catchment area edges. These locations coincide with areas where the groundwater thickness is most significant, given the constant layer thickness across the model.

5.5. Hydrogeological model of the study area

The created hydrogeological model, depicted in in Figure 16, aligns with the lithostratigraphic model boundaries and maintains a resolution of 10m. The model spans 2600 m (261 rows) in the N-S direction and 3050 m (306 columns) in the E-W direction. This model consists of a

single layer only (limited by the ground surface and bedrock) with the thickness shown in Figure 15. Attempts to implement a four-layer model, aligning with lithostratigraphic model results for each layer were unsuccessful: these modelling attempts yielded "absurd" outcomes, as certain parts of the lower layers did not contain water.

Lateral wells simulating lateral water inflow or outflow in the groundwater have been placed along the model's edges. The injected or pumped discharge flow takes account of the influence of the rest of the aquifer, meaning water inflow or outflow across the model's boundaries (obtained thanks to the catchment-scale model). This approach helps avoiding the need for an extensive model where lithostratigraphic and piezometric data may not be available.

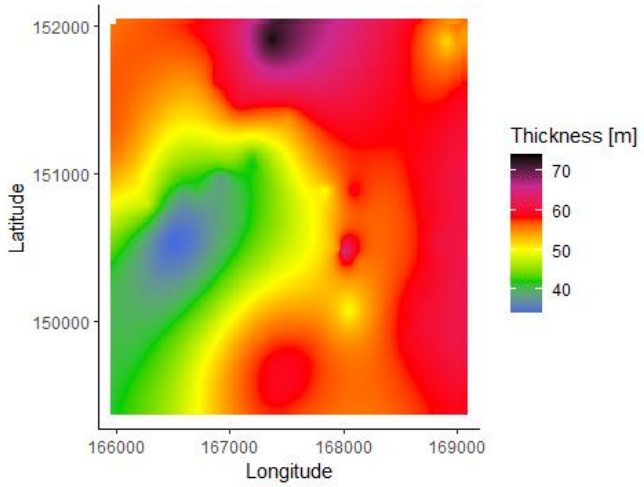

Figure 15 – Total geological layers thickness at LLN (between ground surface and bedrock)

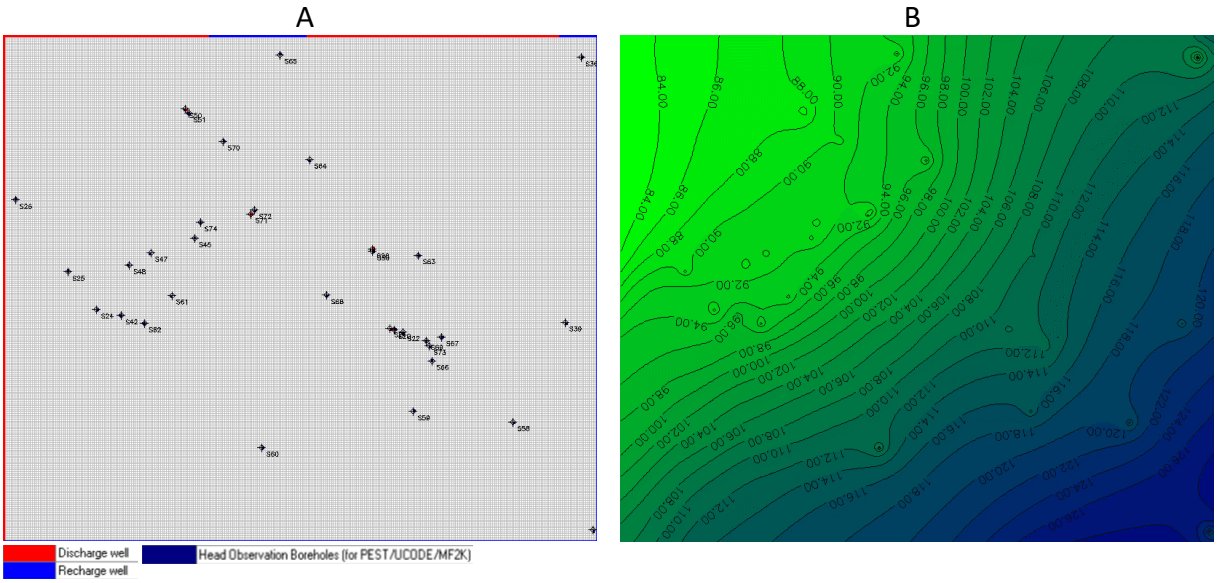

Figure 16 - Model diagram (A) and hydraulic head (altitude of the top of the water table) [m] at the catchment scale (B). Part (A) of the figure displays the lateral wells (injecting or extracting water) and indicates the locations of all the piezometers used for calibration.

Injection wells (feeding the peripheral cells) are situated on the South and East edges (indicated by blue cells in Figure 16), while pumping wells (removing water from the peripheral cells) are exclusively located on the North and West edges (highlighted by red cells), except for four specific 100-meter sections where water is injected in limited quantities (a few m^3/d). Notably, the piezometer S65 is placed in close proximity to these lateral wells feeding the peripheral cells.

The resulting simulated groundwater table shown in Figure 16 illustrates a gradient of approximately 40m over a little more than 3km. The gradient indicates a Southeast to Northwest groundwater flow, with the steepest gradient at the model's centre and the shallowest downstream (where the groundwater level is minimal), near the BSC.

Additionally, the figure highlights local variations in hydraulic head at piezometer locations, a result of the calibration process, which adjusts the groundwater level towards the observed values.

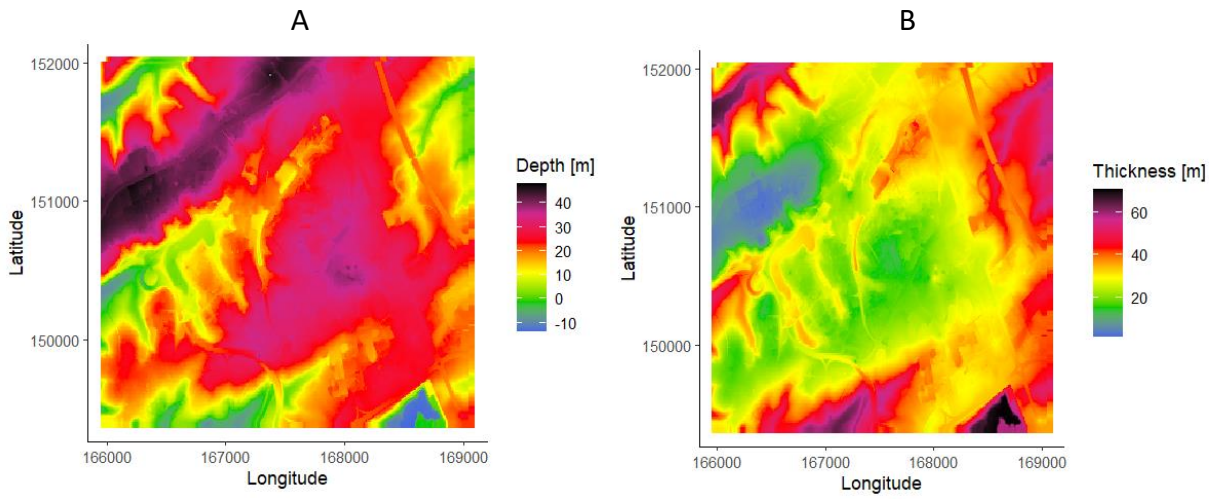

Figure 17 - Water table depth (from the surface) (A) and ground water body thickness (B) in the study area

As shown on Figure 17, negative depths (representing a water height exceeding the surface) are only present at the model's extremities, far from the piezometers used in calibration. These regions also exhibit notably high thickness. Lastly, the figure illustrates that the groundwater thickness is lower near the BSC compared to the rest of the area.

5.6. Heat transfer modelling

For most heat transfer modelling scenarios, injection is set at a continuous rate of 100 m³/d at 20°C for hot water and 5°C for cold water. Results are presented after a 6-month modelling period.

5.6.1. Verification of MT3DMS operation

To ensure the functionality of the MT3DMS model, various tests were conducted separately to avoid interference between them. However, the figures in this section show all results simultaneously to provide a comprehensive overview. Some injection wells serve as controls, while others are paired with a pumping well (also at 100 m³/d), represented by a black point in the figures.

5.6.1.1. Steady state no flow simplified ground water model

A steady state initially uniform simplified groundwater model was implemented. The impact of water model boundary conditions on the thermal state of this simplified groundwater body was tested by creating two modelling scenarios: one with water impermeable boundaries and another with water permeable boundaries, allowing to simulate equilibrium water flow with the exterior of the model's boundary. This allows differentiation between an isolated model from its surrounding environment and a model that takes its environment into account.

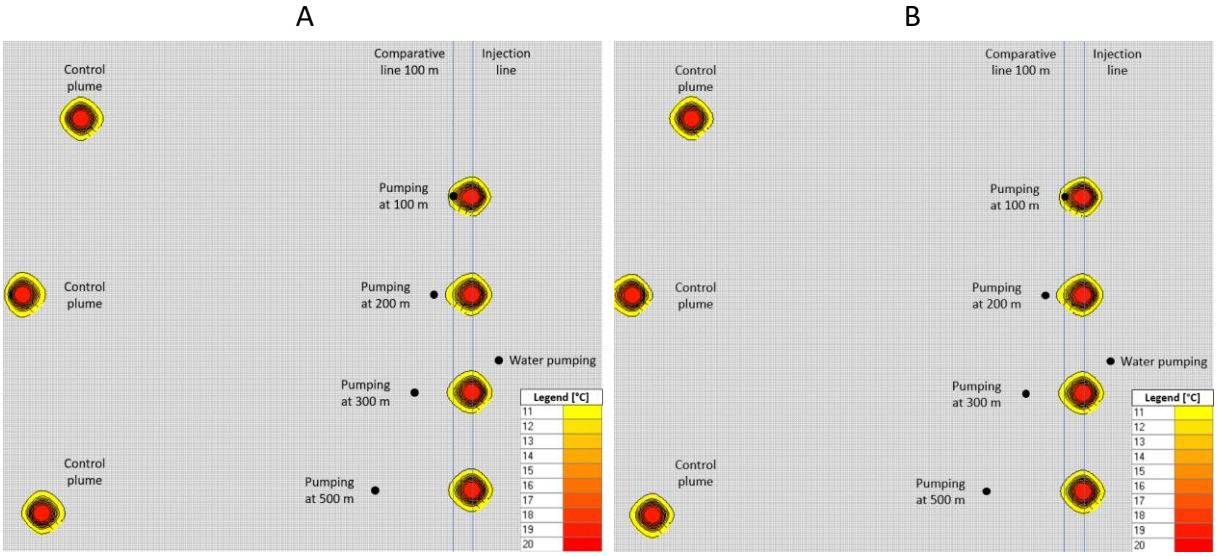

Figure 18 – Influence of boundary conditions on a stationary aquifer: water impermeable boundaries (A) and water permeable boundaries

Control plumes (on the left in Figure 18 (A and B)) reveal that impermeable boundaries impacts the shape of the thermal plumes, especially when they are close to the edges. The progression of the thermal plumes is obstructed by the impermeable boundaries (cf. Figure 18 (A)), leading

them to distort more towards the centre of the modelled region. Conversely, when the boundaries are permeable, the thermal plumes remain circular, as shown on Figure 18 (B).

The impact of pumping at different distances from the injection well shows that when the pumping well is distant, the thermal plumes remain circular (see pumping at 500m from the injection). As it gets closer, an ellipse becomes more noticeable (see pumping at 200 m). In the case of pumping at 100 m, the thermal plume encloses the pumping well.

5.6.1.2. Steady state flow simplified groundwater model

Subsequently, a steady state simplified (mobile) groundwater model was implemented. Therefore, a difference in hydraulic head was created within the model, with the bottom remaining flat at 0 m elevation. The initial hydraulic head was defined considering a gradient similar to that of LLN (in Figure 16). A 40 m difference between the east and west boundaries (3050 m apart) was implemented, as illustrated in Figure 19. Additionally, the constant head cell boundary condition was applied to all the contour cells.

In Figure 19, the top plume represents the "control" configuration with a constant water height gradient, where there is injection but no nearby pumping. The lower four plumes consider a pumping well at different distances.

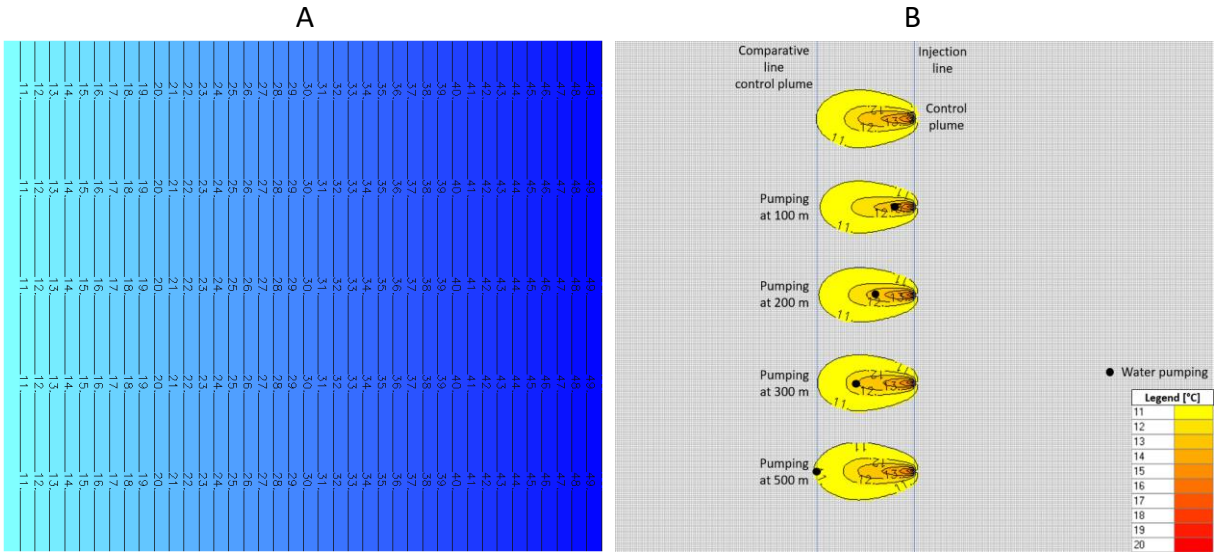

Figure 19 – Influence of initial hydraulic head of the model (A) and the distance of pumping wells from injection on thermal plume (B)

Figure 19 shows that aquifer flow results in highly stretched plumes. This is primarily influenced by the natural flow of the groundwater, the injection well, and to a lesser extent, other wells in the model. The control plume helps to assess the size of the thermal plume: in this model configuration, it measures exactly 50 cells, equivalent to 500m in length.

The four other situations represented on the figure are related to downstream pumping. This demonstrates that pumping also slightly influences the shape of the thermal plume, but to a lesser extent than the impact of the water flows. After 6 months, if the plume has passed the pumping well, the plume is slightly shorter as it is partially retained (see pumping at 100, 200, and 300 m from injection). Conversely, if the plume is still farther than the pumping well, it tends to stretch (see pumping at 500 m).

5.6.2. Energy transfer study

After verifying the operation of the MT3DMS model on the simplified models above, the complete model of LLN was used to study how thermal energy flows within the groundwater body at different injection locations. The results are shown for a modelling duration of 6 months.

5.6.2.1. Impact of injection position on thermal plumes

Injection wells were strategically placed across the model to provide an overall view of the study area. Thirty wells were evenly distributed across the entire model. To maintain a realistic model behaviour and balance, an equivalent amount of water was pumped through a well located a few cells south of the injection. Figure 20 shows the results with a thermal resolution of 0.1°C, depicting changes in colour for every 0.1°C change.

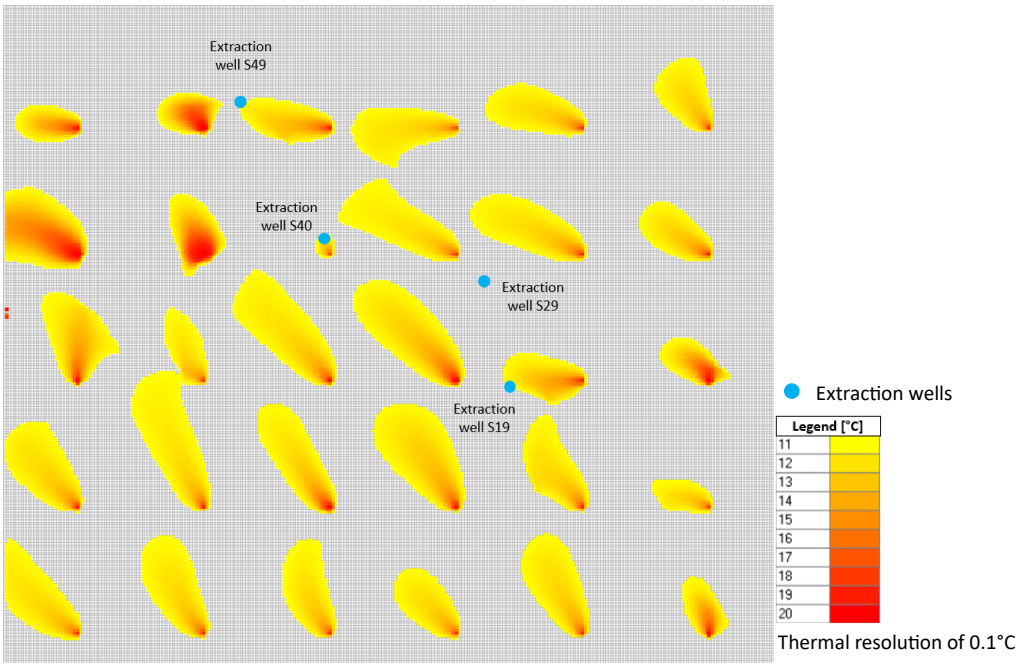

Figure 20 – Thermal plumes for different injection location over the entire study area

Figure 20 reveals significant variations in thermal plume size and shape based on the injection location. However, plumes generally extend in the Northwest direction. Plumes in the

Northwest part of the area disperse more in width, retaining more heat in their centre (i.e., energy tends to disperse less), while those in other areas extend more in length.

Finally, extraction wells tend to attract plumes, as shown by the plumes in contact with wells S49, S40, and S19. Notably, well S40, situated just downstream of the injection well, results in a much smaller corresponding plume.

5.6.2.2. Impact of UCLouvain extraction wells on thermal plumes

To specifically study the impact of extraction wells, a dedicated scenario was created. It involved injecting heat at 100 m (in a straight line or diagonally) around the existing groundwater extraction wells. This distance corresponds to the "distant prevention zone" that must be maintained around extraction wells to limit contaminations (cf. Appendix 9.1.2). The injection rate was limited to 25 m³/d to avoid overloading the wells and affecting the results, and an injection temperature of 50°C was specified to ensure visibility of heat dissipation with a low volume. Figure 21 shows the results of this scenario.

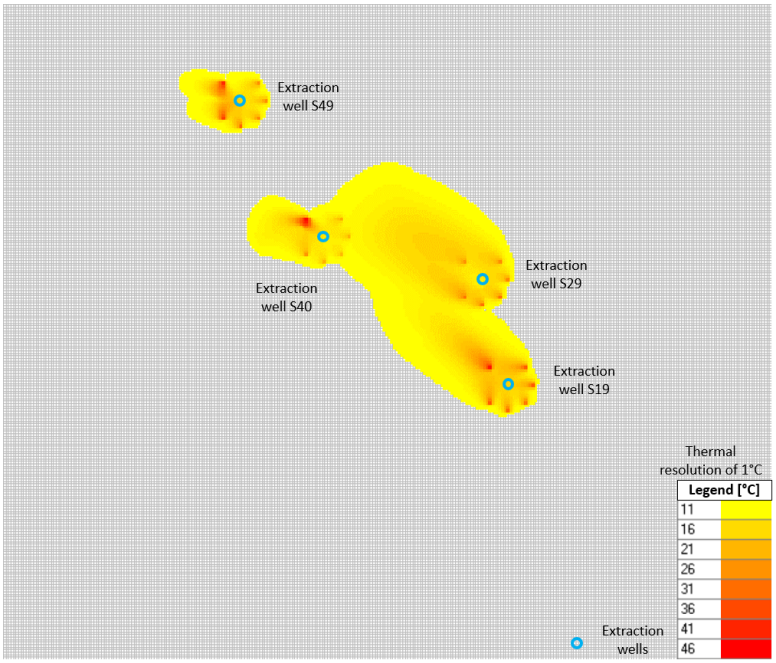

Figure 21 – Influence of water catchments on thermal plumes

The two extraction wells with higher pumping rates (S49 at 601.76 m³/d and S40 at 302.04 m³/d) tend to retain more heat injected downstream. The thermal plume is smaller, and the heat injected downstream of the extraction point dissipates minimally. In contrast, extraction wells with lower pumping rates generate larger thermal plumes.

Moreover, injected energy upstream or on the sides is still pumped, regardless of the extraction well.

5.6.2.3. Specific case of BSC and large buildings

a) Simplified scenario

The next step involved approaching the actual location of injection and extraction wells, specifically near buildings. A model was created with only injection (no extraction well) of 100 m³/d at 20°C near the major buildings in LLN to obtain a general idea of the heat transfer. The results of this simulation are presented in Figure 22.

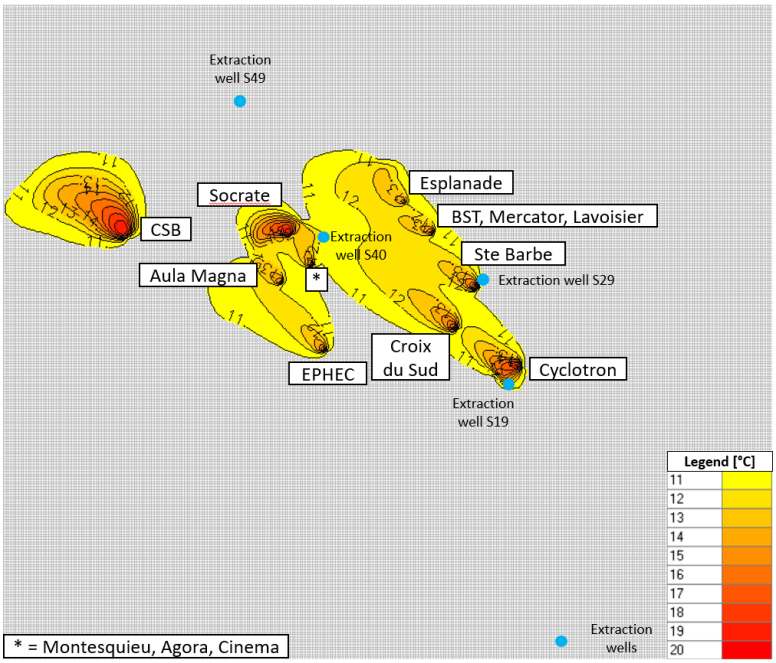

Figure 22 - Evolution of thermal plumes from injection (100 m³/d at 20°C) near large buildings located in LLN

Figure 22 illustrates that heat disperses less for the BSC compared to the injection closer to other buildings. Similarly, a thermal plume injected at Socrate, located near extraction well S40, generates a small thermal plume and maintains a high concentration of thermal energy. The same applies to the "Cyclotron" and the buildings "Ste Barbe", but to a lesser extent.

The figure also reveals that some buildings align along the same flow path. This is evident in the cases of "Cyclotron" with buildings of "Croix du Sud", "Ste Barbe" building with "BST-Mercator-Lavoisier and Esplanade", as well as "Ephec" with "Aula Magna".

b) Interconnection between buildings on the same flow line

Based on these results, a more realistic approach was followed. The three flow axes (from Figure 22) that were least impacted by extraction wells were chosen for further investigations. These are the flow axes originating from "Ephec", "BST-Mercator-Lavoisier", and the "Cyclotron" (the latter is retained because the well has a low discharge, and its impact is negligible if the injection is done on the other side of the Cyclotron building). Both injection

and extraction were integrated for simultaneous hot and cold water storage (in parallel), installed at a sufficiently large distance to prevent mutual impact.

The result of this scenario is presented in Figure 23. The proposed system initially pumps water (empty circle, blue or red depending on temperature) at 11°C just upstream of the injection wells, at a slight distance to try to limit their impact on the plume's shape. This pumped water is heated or cooled and then simultaneously injected (filled red or blue circle) in the upstream ATES well. Subsequently, downstream ATES wells pump (solid black circle) the stored water and reinject it (empty black circle) after recovering energy. This reinjection is done at 11°C to avoid impacting potential downstream ATES storage systems.

Yellow points in Figure 23 represent the UCLouvain extraction wells, red colour indicate hot water storage, and blue colour represents cold water storage.

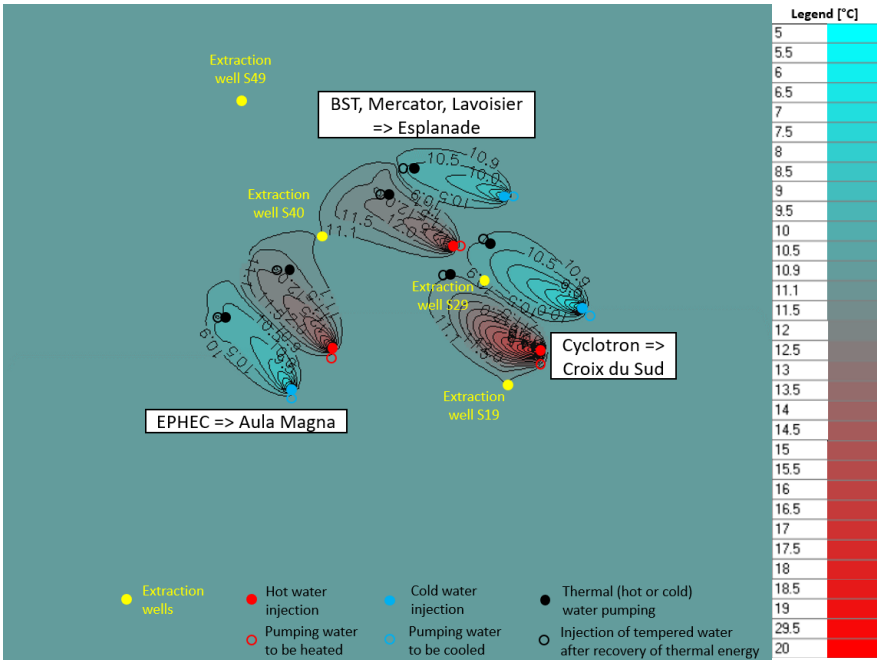

Figure 23 - Interconnection between buildings on the same flow axes (with two flow axes for each building)

Figure 23 demonstrates that interconnection between buildings (i.e. recovering the thermal energy injected at one building to another building) seems possible, potentially reducing the pipelines length connecting wells to buildings. The figure indicates that flow axes must be positioned at a sufficient distance from each other to avoid significant thermal contamination from the parallel line: several hundreds of meters are necessary.

5.6.3. Implementation of an ATES system for the Blocry Sport Centre

The purpose of this scenario is to closely imitate the operation of an ATES system implemented for the BSC throughout the year. Three different scenarios were implemented: one for the summer period, one for the winter period, and the last one for the interseasonal regime. The system contains only two wells, active during summer and winter (during pumping-injection periods), and inactive for the rest of the year. Consequently, this implies that the pumped downstream water is transported to the BSC through pipelines and reinjected upstream once the energy transfer is complete. This choice was made as the distance between the wells is relatively short, and installing pumping well upstream the BSC would attract the plume upstream, increasing its dispersion.

The results of the model, beginning at the start of summer with an operational flow rate of 100 m^3/d, and injection temperatures of 20°C in summer and 5°C in winter, are presented in Figure 24 for the first year at three-month intervals. Figure 25 depicts the state of thermal plumes in the first four years at the beginning of winter, just before starting to pump heat. Appendix 9.5.1 contains monthly results for the first three years of this scenario, starting with heat injection (see Figure 36), and results every three months for a 1-year modelling period starting with cold injection (see Figure 37).

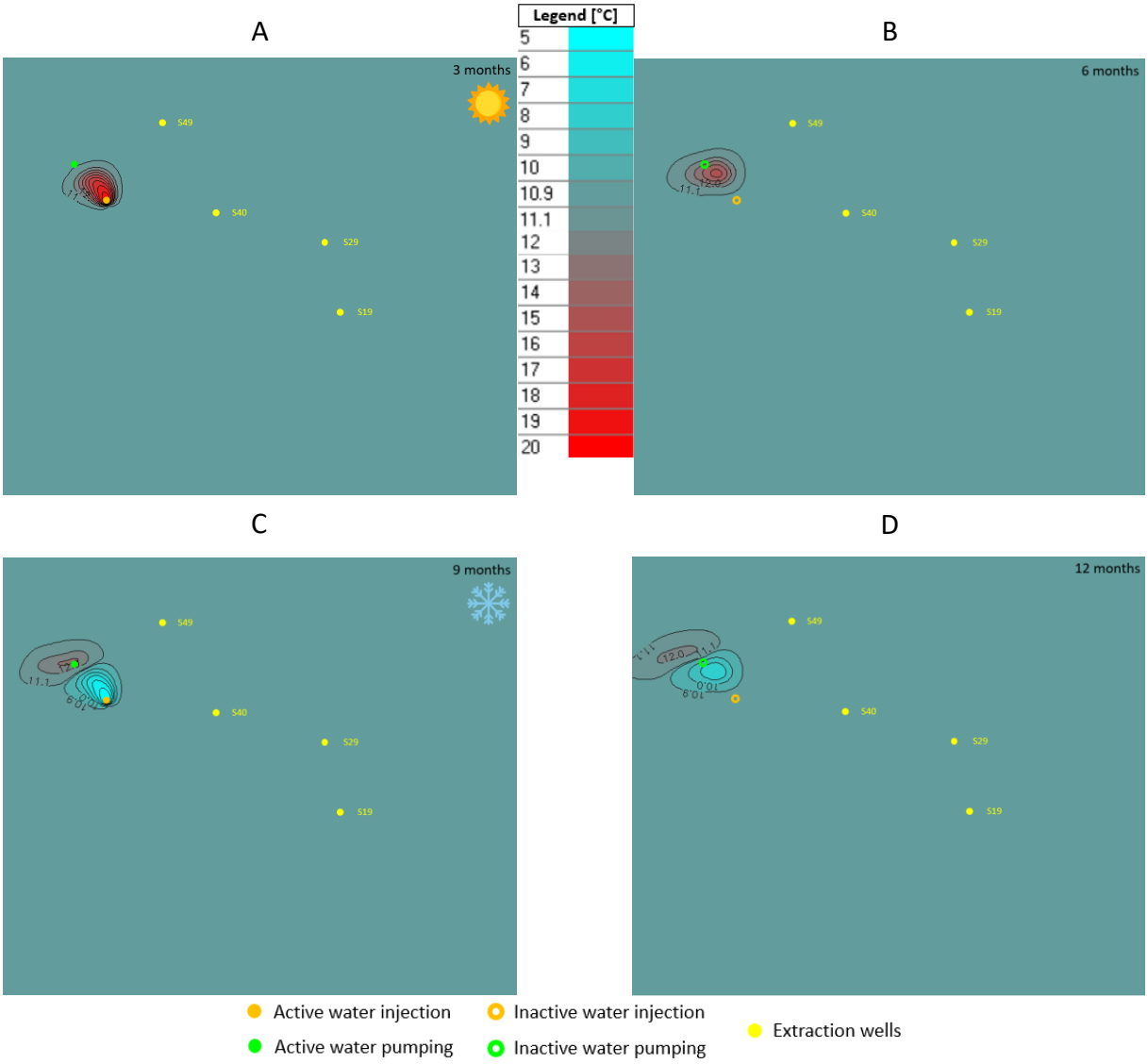

Figure 24 – Evolution of the thermal plume stored by the ATES after 3 months injection at 20°C (A), 6 months (3 months injection and 3 months rest) (B), 9 months (case B + 3 months injections at 5°C) (C) and 12 months (case C + 3 months rest) (D), starting with summer

Figure 24 and Figure 25, along with those in Appendix 9.5.1, show that the thermal plumes are quite wide, allowing flexibility in selecting the pumping well's location in case of surface obstacles. Furthermore, each hot/cold plume surpasses the well at the initiation of pumping (i.e., every 6 months), eliminating any interference from the preceding plume, as demonstrated in cases B and D in Figure 24, and particularly well in Figure 25.

Figure 25 also indicates that the thermal plumes remain identical from one year to the next. Moreover, these plumes are entirely replaced during the next flow periods, minimizing any residual impact from the previous year. Additionally, Figure 24 illustrates that, one year after the modelling begins, the plumes reach the model's boundaries and are subsequently pumped by the lateral wells (i.e. boundary cells removing water from the modelled water table).

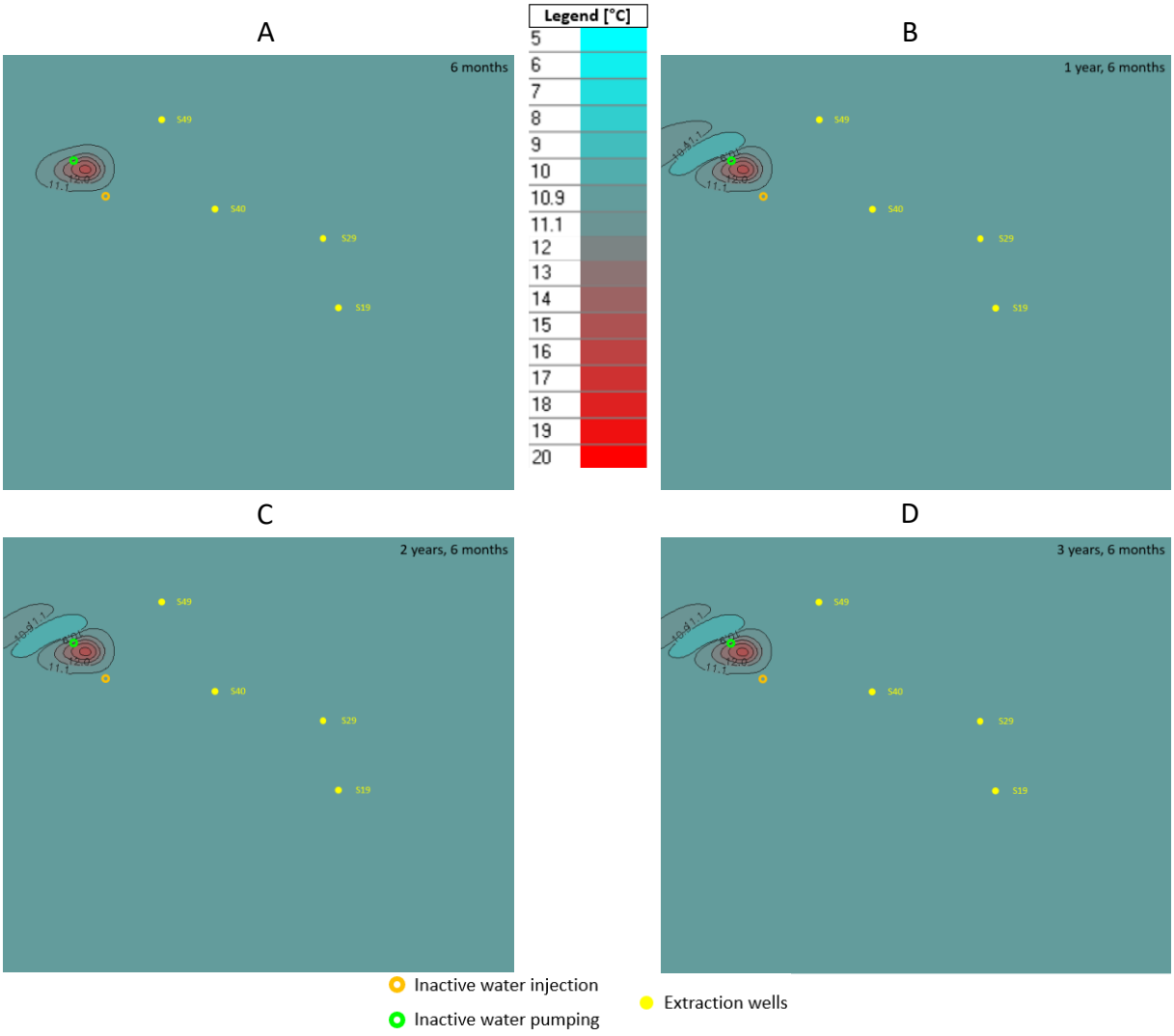

Figure 25 - Evolution of the thermal plume stored by the ATES after 6 months (A), 1.5 year (B), 2.5 years (C) and 3.5 years (D), starting with summer.

Efficiency calculations were based on the energy injected in the first stage (between 0 and 3 months) and that pumped in the third stage (between 6 and 9 months), because after this point, the pumped energy also measures the amount of energy pumped by the simulated lateral wells, which is not recovered but lost to the environment. The modelling was conducted twice: once starting with hot injection and once with cold injection, to calculate the efficiency of both hot and cold storage.

The optimal pumping area, found in relation to injection between BSC and Blocry parking (coordinates: 166 610 m, 151 160 m), is located near the cell with coordinates 166 420 m, 151 370 m, situated close to the outdoor athletics track (not far from “Bois de Lauzelle”). The distance between these two wells is 283 m (calculated using the Pythagorean theorem).

Table 9 summarizes individual and overall system efficiencies for various modelling scenarios, including variations in summer injection temperature and operational discharges. Figures corresponding to these scenarios are provided in Appendix 9.5.

Table 9 – BSC's ATES system performances for different operating flow scenarios and summer injection temperatures (sensitivity analysis)

Scenario	Injection characteristics		Distinct thermal plumes (flow line)	Distinct thermal plumes performance		Complete cycle system performance		
	Q [m³/d]	T_{inj} [°C] summer / winter		$\overline{T}_{pumped}$ [°C]	$\eta_{flow\ line}$ [%] (until 11°C)	ΔT_{in} [°C]	ΔT_{out} [°C]	$\eta_{complete\ cycle}$ [%]
A	**100**	**20 / 5**	Heat	13.6	29.20	10.8	8.6	79.96
			Cold	9.2	29.85			
B	100	**15** / 5	Heat	12.2	28.88	5.8	7.2	123.53
			Cold	9.2	29.87			
C	100	**25** / 5	Heat	15.1	29.32	15.8	10.1	64.00
			Cold	9.2	29.82			
D	**50**	20 / 5	Heat	12.6	17.77	10.1	7.6	74.91
			Cold	9.9	19.08			
E	**200**	20 /5	Heat	14.6	40.10	11.4	9.6	84.30
			Cold	8.6	39.98			

In Table 9, the efficiency of the distinct thermal plumes corresponds to the proportion of injected energy recovered during pumping. For heat storage, ΔT_{in} determines the total energy injected into the system in summer (i.e., the energy to raise the temperature of the pumped stored cold water to the injected hot water temperature), and ΔT_{out} determines the total recovered energy (i.e., to lower the temperature of pumped stored hot water to the injected cold water temperature during winter). For heat storage of configuration A, this involves heating the water to raise it from 9.2°C (temperature of the pumped stored cold water in summer) to 20°C (injection temperature) and, in winter, cooling it from 13.6°C (temperature of the pumped stored hot water water) to 5°C (injection temperature).

Table 9 shows that the efficiency of the distinct thermal plumes is approximately 30% for configuration A. It varies significantly with the system flow rate (increasing with the flow rate), while efficiency varies little with changes in injection temperature. Indeed, the efficiency is similar for the hot and cold parts of the same configuration and does not vary with the hot injection temperature.

When taking an overall view of the system (i.e., combining hot and cold storage), the (complete cycle) efficiency approaches 80% and even exceeds 100% in configuration B, where the summer injection temperature is 15°C. This occurs because the quantity of injected energy is lower than that recovered during water extraction. Additionally, the discharge also has a slight impact on the overall efficiency, ranging within a few percentage level.

6. Discussion

6.1. Quality analysis of the lithostratigraphic model results

As described in section 4.1, the methodology followed was as precise and relevant as possible, but the results indicate imperfections in the predictions.

The initial dataset, with only 30 measurement points lacks uniform distribution due to some piezometers being grouped together, potentially providing conflicting information. This dataset was not sufficient to make a good prediction/interpolation across the 8 km² study area, especially since some data have been considered as outliers. The proximity of only two piezometers (S25 and S26) near the BSC perimeter limited data coverage in this area.

Several sources of error further impact the model:

Firstly, some variograms created exhibit a short range, significant nugget effect, and variogram functions exceeding data variance and not correctly representing the dataset (cf. Table 5 and Figure 7). Variance related to residue prediction demonstrates increased variability away from measurement points (cf. Figure 8), a consequence of kriging's limitation due to its poor extrapolation capabilities.

Secondly, calculating layer altitude based on the basis of the altitude and thickness of the previous layer propagates errors from one layer to the following (cf. Figure 12 (and Figure 31)). This transmission of errors can transmit the previous altitude differences (if the predicted thickness error is zero), amplify it, or, conversely, attenuate it (if the altitude error decreases compared to the previous layer). Consequently, the precision and accuracy of altitude predictions for geological layers decreases progressively as layers progress, given that errors from preceding layers influence subsequent ones (cf. Table 7). This phenomenon is confirmed by the fact that statistics are not necessarily improved for these deeper layers when outliers and points located beneath the concrete slab are removed (cf. Table 8), the concrete slab introducing an unavoidable error (as the DTM cannot ignore it), shifting all altitude values in that zone by approximately 7.5 meters upwards (cf. Figure 12). This observation is consistent with the Leave-One-Out Cross-Validation (LOOCV), which revealed that the prediction for the Bedrock's altitude is overestimated by 20 and 10 meters for piezometers S25 and S26 (located near the BSC), respectively, when compared to their measured values.

Despite all these sources of error, the spatial prediction achieved a detailed 10-meter resolution, facilitating the subsequent hydrogeological model's spatial precision and accuracy.

Further improvements to the model and its overall quality could involve obtaining more measurement data for the area (and following the same methodology) or integrating covariables correlated with the variable to interpolate through methods like cokriging

(Knotters et al., 1995). An alternative approach could employ Python's Gempy library, capable of constructing complex 3D geological models and conducting uncertainty analysis (de la Varga et al., 2019). However, this method requires additional data, such as the orientation of measurement points, indicating the direction of the steepest gradient.

In summary, while recognising the limitations of the available data, the lithostratigraphic model's methodology was meticulous and relevant, providing acceptable results for progressing to the next phase of the master thesis. This model, despite its imperfections, added constraints on the subsequent work. Considering that only one layer was used in the hydrogeological model, predicting total thickness rather than individual layers might have been preferable. This approach could have mitigated issues associated with negative thickness in the Tongrian layer.

6.2. Critical analysis of the hydrogeological model

6.2.1. Regional scale model

As explained in section 4.2.1, the simplified hydrogeological model at the catchment scale considered all known hydrogeological characteristics of the Bruxellian sands aquifer or the watershed, except the total soil thickness down to the bedrock for each model cell. This total soil thickness is not known at the catchments scale, since no generic data are available of altitude at which the bedrock begins. In the regional model, the total soil thickness was estimated by assuming a constant average soil thickness in the study area. While this assumes a bedrock perfectly parallel to the surface, which is not realistic (as the surface is subject to constraints that the bedrock does not experience), this simplification is acceptable, especially near the study area where this estimation approaches the reality. The constant thickness assumption was considered acceptable, given the objective of the regional hydrogeological modelling, i.e. defining the hydrogeological boundary conditions for the local model for the site of LLN.

The hydrogeological model performed better near the LLN study area, given the availability of several piezometric observations for calibration. Yet, most piezometers are situated in the Southern half part (i.e., upstream part) of the watershed. Model performance is therefore worser Northwards. Additionally, due to the model's boundary conditions, water accumulated in the Northern part of the model (i.e., the downstream part of the watershed), and the water level was even higher than the ground surface (cf. Figure 14). This accumulation occurred through gravity-driven flow; the river alone was insufficient to drain all the water. However, it is assumed that this does not impact the flow of the local LLN study area, as it is downstream and far from the study zone.

The assumption of a constant soil thickness across the entire regional model had non-negligible impacts. Despite the apparently gradual evolution of the predicted hydraulic head in Figure 13, a constant thickness engendered a rapid variation in both the thickness and depth of the water table (cf. Figure 14). This was a consequence of the model's bedrock being strictly parallel to its surface, a condition that cannot be true. The areas where this is most noticeable are in the valleys of the secondary rivers, primarily situated on the model's edges.

The impact of grid resolution was also noticeable. Figure 13 revealed slight variations in hydraulic head from one cell to another along the river, a result of the 100 m resolution causing mismatches between the surface altitude of the cell node and that of the river.

Despite these challenges, Figure 34 (Wallonie.be, 2006) and Figure 35 (Fasbender, 2008) exhibited piezometric curves similar to those in Figure 13 for the watershed, generally parallel to the modelled river, reflecting the outcropping of the water table. However, the gradient obtained was not exactly corresponding to reality because, to the East of LLN, the actual flows deviate to the right, driven by the Train river (cf. Figure 34). Nevertheless, the impact on the estimation of the hydrogeological boundary conditions for the local study area in LLN was assumed to be negligible, since it takes place far from LLN.

In summary, the model was confronted with numerous simplifications, and inconsistencies, particularly when situated far from the study zone. However, these differences became less marked as distance from the study area decreases.

6.2.2. Local scale model

As discussed in section 5.5 (refer to Figure 16), some boundary cells simulating the lateral inflow of water into the groundwater body are located on the Northern edge of the model. This phenomenon is likely attributed to the S65 piezometer, which appears to induce a minor water flow towards the South in the watershed model. Although these are low flow rates, they may distort the flow results, generating a flow from downstream (outside the model) towards the study area.

Furthermore, the overall number of piezometric observations used to calibrate the model (based on groundwater level measurements) is relatively low, leading to large areas without calibration data. This local data scarcity impacts predicted groundwater level results (refer to Figure 16). Due to the limited number of piezometers, local variations in hydraulic head (see predicted piezometers heads in Figure 16) are predicted to fit the measured water levels in the calibration process. However, the influence of the calibration on head variation decreases when moving away from these piezometers, approaching the natural balance of the water table. These local variations may not accurately represent reality, except, perhaps, in the case of groundwater extraction points.

Figure 16 also indicates a lower gradient of the water table in the upper left (downstream part) compared to upstream. One possible explanation is the slight accumulation of water due to the boundary cells simulating lateral water inflow or outflow. The flow rates, determined at the watershed scale, may not perfectly simulate the actual water discharge. However, the few available piezometers upstream do not show significant variations, suggesting that the final water table level is not far from the values measured by the piezometers (cf. Figure 16).

Another noteworthy observation is the abnormally low or high thicknesses highlighted in Figure 17 in certain parts of the model. Firstly, the area around the BSC exhibits a low water thickness compared to the rest of the study area. This is linked to the lower predicted soil thickness than the expected reality, likely due to an overestimation of the bedrock altitude in this area, as explained in section 6.1. Similarly, negative water depths, indicating higher water levels than the land surface, are observed in the lowest areas on the model's edges (as shown on Figure 17), where no piezometric observations are available nearby.

Finally, the chosen 10-meter resolution for this model yields finer results as calculations are performed on more closely spaced cells. The finite difference calculation between cells is more efficient, providing greater precision in locating UCLouvain extraction points, piezometers, boundary cells where the developed model feeds or removes water (modelled as lateral wells), as well as injection/pumping wells for the subsequent heat storage study.

6.3. Performance analysis of the heat transport model

6.3.1. Model analysis

Firstly, it's crucial to note that, given the model's single-layer nature, only 2D heat transport was considered, and vertical heat transport is ignored. In addition, the heat transport model heavily relies on all data, methodologies, and assumptions considered in the previous parts of the work. Note that the constraints of the lithostratigraphic model impose a thin groundwater body near BSC (cf. Figure 17). This generates broad thermal plumes, since for a given injected water volume, heat spreads more laterally in shallow groundwater bodies as compared to thick groundwater bodies. Another reason explaining the significant lateral dispersion is the utilization of a higher value for transverse dispersivity (α_T) compared to longitudinal dispersivity (α_L) (cf. section 2.3.2), whereas normally the opposite is expected (Bear, 1979; Domenico & Schwartz, 1998).

The simulations used to verify the proper functioning of the software revealed important insights. They highlighted the importance to specify boundary conditions to avoid edge effects, as shown in Figure 18. It is crucial to ensure that the water level remains constant throughout the model's boundary to simulate model continuity (i.e., preventing it from being isolated).

Additionally, Figure 18 and Figure 19 demonstrated that pumping and injection wells do have an influence on energy travel distance, corresponding to expectations (Bloemendal & Olsthoorn, 2018). However, this influence is not significant, since the control plume (without pumping wells) in Figure 19 is not very different from those influenced by a pumping well. Therefore, the gradient of the water table at LLN significantly influences thermal plume size, with wells having only a minor effect.

While several verifications were performed on simplified scenarios, a more in-depth exploration of slope and well flow rate impacts on plume shapes could have been beneficial. Examining the impact of a slope at the model's bottom boundary, instead of assuming it to be flat, would also be interesting.

6.3.2. Identification of zones to be preferred or avoided

Observations from the "pumping-injection simulation experiments" in the LLN area revealed important considerations:

Firstly, Figure 20, Figure 21 and Figure 22 highlighted that heat injection must be avoided near UCLouvain's extraction wells, both upstream and downstream, especially for high-flow wells like S49 and S40 (cf. Figure 21). High pumping rates tend to retain heat injected downstream and attract lateral and upstream injections. To prevent contamination, pumping wells should be placed sufficiently far from extraction wells (minimum 100 m) (Ruthy et al., 2017) (cf. Appendix 9.1.2).

Next, the different shapes of thermal plumes in Figure 20 and Figure 22 are directly linked to the water table gradient, indicating flow velocity variations (cf. Figure 16). Plumes in the Northwest part of the area disperse more in width compared to others that extend more in length. Notably, thermal plumes in this Northwest part retain higher temperatures at their centre, suggesting less mixing with ambient water, potentially offering higher energy recovery as the surface area over which losses occur decreases (Bloemendal & Olsthoorn, 2018). This observation implies that the Northwest region could offer a more efficient performance for the ATES system, as the amount of recovered energy might be higher. Given that the heat pump's efficiency is directly linked to the water temperature, it seems that the efficiency would be superior in the northwest part than in the rest of the area where thermal losses are more significant. Thus, this suggests that the BSC region could be a suitable zone for installing an ATES system.

Section 5.6.2.3, exploring the possibility of interconnecting buildings, revealed that some buildings share the same flow path. This implies the potential for using one (UCLouvain) building to inject thermal energy into the groundwater body, benefiting another building (also from UCLouvain) (refer to Figure 23) and reducing the overall university energy balance and

the total pipes length. However, these are preliminary results from a simplified model, requiring further study similar to the one conducted for BSC. Preliminary results show, though, that to avoid (thermal) contamination of one storage flow line by another, they need to be placed at a large distance from each other. Additionally, in this particular area of the study, the higher flow velocity appears to permit the pumping of water at 11°C upstream of the injection without pulling the thermal plume in the upstream direction. This provides the advantage of separating the pumping period from the injection period and offering greater flexibility in selecting the pumping location.

6.3.3. Performance estimation of ATES system applied to the BSC

6.3.3.1. Modelling analysis

While detailing the aspects of the modelling, it is crucial to analyse both the disadvantages as well as the advantages inherent to this approach.

The model's configuration involved downstream pumping with water reinjected upstream, making it impossible to separate pumping and injection periods. This limitation exposes the system to a potential risk of contaminant displacement since water is extracted from one location and injected quite a distance away. Another drawback is related to the studied scenario's configuration, following a constant injection and pumping pattern for three months, which does not entirely reflect reality. In real conditions, building energy demands can vary over time (on a daily as well as hourly scale), implying that changing flow rates would be more representative of the system. Therefore, intermittent injection, often more realistic, could create smaller thermal plumes surrounded by ambient water, likely resulting in increased thermal losses (Bloemendal & Olsthoorn, 2018). Lastly, the efficiencies were computed based on the average water temperature pumped by the downstream well, offering no information on the temporal evolution of the pumped temperature profile over time. This could potentially distort the efficiency calculations, particularly for the heat pump.

However, this scenario has some advantages that have to be noted. Firstly, the reduced groundwater flow velocity beneath the BSC minimizes the distance travelled by the thermal plumes, thereby reducing the distance between ATES wells and also diminishing the required pipe length needed to connect the wells to the BSC. Additionally, the large thermal plumes offer increased flexibility in well placement, useful in case surface obstacles prevent well installation at the desired location. Finally, the 10-meter precision grid allows for a detailed study of the thermal plume's flow within the groundwater body.

6.3.3.2. Performances

The efficiency is calculated for the first cycle because afterward, thermal plumes reach the model's edge and are pumped by lateral wells, simulating water outflow. This introduced

distortion to the results concerning the amount of energy pumped by all wells in the model. Moreover, efficiency cannot increase over the years because the entire thermal plume is replaced by groundwater flow and subsequent plumes. As shown by the plumes in Figure 25 (and Figures in Appendix 9.5), which are identical year after year, the system is in balance (and efficiencies therefore remain constant, not increasing with years). This proves that intermittent injection of hot and cold water through the same wells on the same flow line does not pose any efficiency problem (since everything is replaced).

Results from Table 9 show that the efficiency, i.e., the amount of recovered energy compared to injected energy, is approximately 30% for the studied scenario (injecting 100 m^3/d at 20°C in summer and 5°C in winter), both for heat and cold energy storage. This is low compared to the 80% that ATES systems can achieve, even if efficiency decreases with increasing flow velocity (Bloemendal & Olsthoorn, 2018). Another parameter influencing efficiency and explaining this large difference is the significant transverse dispersivity characterizing the aquifer (Ruthy et al., 2017).

Sensitivity analysis results from Table 9 also indicate that efficiency does not seem to vary with injection temperature but varies significantly with the flow rate of the ATES system:

Regarding the temperature effect, it does not align with expectations as losses should increase with rising temperatures (Fleuchaus et al., 2020; Sommer et al., 2013; Tatsidjodoung et al., 2013). One possible explanation is that vertical transfers are not considered in the 2D model, therefore reducing total losses.

Regarding the impact of the operating discharge variation, it is confirmed that the energy recovery factor increases as the injection/pumping rate rises (Vidal et al., 2022). There is a reasonable assumption explaining why the discharge significantly influences efficiency: the larger/bigger the plume, the better it can protect itself from the environment, thus retaining its energy at a temperature closer to the injection temperature.

Looking at the overall system efficiency over a year, the efficiency values are much better. In the case studied, the discharge has a less significant impact on overall efficiency, but efficiency increases with decreasing injected temperature (and 100% efficiency can be exceeded, as shown for configuration B in Table 9), as the injected energy is lower than the recovered energy during pumping, indicating that the groundwater provided the energy by warming the cold water more than the hot water was cooled: energy comes from the environment.

6.3.3.3. System use recommendations

In summary, it looks advisable to inject water that is not too hot at a high flow rate to promote energy transfer from the groundwater body to the system (and not the other way around) and thus maximize efficiency.

However, this does not mean it is the best solution to maximize the overall efficiency of the entire system, which transfers energy between buildings and the groundwater body (and vice versa). Indeed, the heat pump (which is the core of the heating system), operates better (i.e., has a better COP) when the energy source temperature is as high as possible. Therefore, it is preferable to prioritize a high injection temperature and a lower flow rate, even if the efficiency of storage in the aquifer is lower.

6.4. Perspectives

There are several ways to enhance the methodology used in this work to achieve more conclusive and comprehensive results.

Firstly, it would be highly beneficial to study the implementation of ATES systems for the large buildings in LLN through a more realistic scenario than the one already examined. This involves distinguishing the pumping, injection, and flow seasons to correspond to a more plausible operation, as was done for the BSC.

Secondly, it is crucial to explore the situation using a multi-layer model that incorporates the vertical component, simulating the 3D environment, because this adjustment could potentially impact the final conclusions on efficiency results. This approach would also allow for considering the storage of hot and cold at different depths (Bloemendal & Olsthoorn, 2018) (if there is no risk of mixing), therefore eliminating the need for two parallel flow lines that have to be quite distant from each other to avoid mutual interference, as currently depicted in Figure 23.

Thirdly, it would be valuable to study the heat pump system in detail, considering the input temperature (recovered from the groundwater), circuit components (discharge, compression, fluid type), and so on. This analysis would aim to determine the overall system efficiency and identify the actual injected flow rate over time. It would help verify whether it is really worthwhile to install the system for the needs of BSC and potentially other UCLouvain buildings.

Furthermore, the implemented scenario studied for BSC includes only one pumping well and one injection well. However, considering that the system does not operate at a constant flow rate would imply that the thermal plume may not always be at the pumping well's location when needed. Therefore, studying a scenario with multiple downstream wells would be useful to increase the chances of accessing a plume when necessary (Bloemendal & Olsthoorn, 2018).

Moreover, obtaining more geological data (or verifying the erroneous ones in the database) is essential to create a better lithostratigraphic model of higher overall quality. This would also

enable the construction of a larger model for LLN (if geological and piezometric data are available) to attempt expanding the model's boundaries and moving them away from the BSC.

Lastly, it would be interesting to calculate the economic and environmental profitability of the systems to provide a more comprehensive overview of their contributions and costs. This involves comparing the costs (both economic and environmental) of system design, implementation, and maintenance/repair with the potential costs savings and emissions reduction (Bloemendal et al., 2018).

7. Conclusion

The primary objective of this master thesis was to evaluate the potential of storing surplus heat collected in the summer in the dynamic groundwater system of Louvain-la-Neuve (LLN) for subsequent recovery in the winter.

The most suitable storage system identified for the interseasonal thermal energy study in the LLN configuration is the Aquifer Thermal Energy Storage (ATES) system, owing to the urban environment and the presence of the Brussels sands groundwater body flowing underground.

The study started with the development of a lithostratigraphic model for the entire study area using kriging, based on scattered measurement points. Subsequently, a hydrogeological model of one layer in the study area was created using MODFLOW software and calibrated with piezometric observations conducted by technical services of UCLouvain. Estimations of fluxes at the boundaries of the study area were made through simplified watershed-scale modelling to ensure the model's integration with its surroundings.

The heat transfer study within the groundwater body of the aquifer utilized the MT3DMS model. Preliminary results indicated that the positioning of injection and pumping wells has a limited impact on thermal plume behaviour compared to the significant influence of groundwater flow in LLN. Consequently, the well locations remain consistent regardless of the ATES system's operating flow rate, providing flexibility for system adjustments based on needs.

Further investigation revealed distinct thermal plume behaviour in two zones. The first zone, located upstream in the groundwater flow and covering the majority of LLN buildings, showed highly stretched thermal plumes causing substantial energy dissipation due to a significant hydraulic head gradient. In the second zone, downstream of the hydrogeological flow and including the BSC, thermal plumes were less stretched and wider, suggesting that this zone of the study area might offer greater suitability for an ATES system, as these plumes were retaining more energy at their centre. The study also indicated that some buildings shared the same flow path, potentially allowing one building to benefit from the thermal energy stored by another building. Lastly, this work highlighted the importance of avoiding water extraction wells that could pump out stored energy.

The results for a more realistic scenario studied for the BSC showed that, with an injection well at coordinates 166 610 m; 151 160 m (next to the Blocry's parking), the pumping well location that allows to improve the storage performance is at coordinates 166 420 m; 151 370 m. This would allow to recover 30% of the injected thermal energy for an operating flow rate of 100 m^3/d at 20°C in summer and 5°C in winter. However, efficiencies varied with injection flow rate, increasing when the flow rate was higher. When considering the complete cycle (on an annual scale), the efficiency of the initial scenario increased to 80%, further improving with higher

flow rates and lower injection temperatures in summer. However, the heat pump operates with a better COP when the energy source is warmer. It is therefore advised to inject warmer water upstream for a warmer recovery downstream, even if thermal losses in the groundwater body are more significant.

Although focusing on single-layer models and ATES systems operating at a constant flow rate, this study leads to the conclusion that the LLN groundwater body offers storage potential to assist buildings in reducing their primary energy consumption, particularly in the BSC zone.

However, various simplifications and errors occurred throughout the study, notably in the lithostratigraphic model. The statistical LOOCV analysis of this prediction revealed decreasing altitude estimation quality with depth, transitioning from an R^2 of over 0.9 for the first three layers to only 0.57 for the last one. This has led to overestimations and underestimations of reality in different locations, resulting in a predicted thickness of the groundwater near the model's edges that is unrealistic, especially near the BSC where it is too thin. This impacts the quality of the study regarding the assessment of thermal storage potential.

In spite of its limitations, this work can serve as a starting point for more in-depth studies on interseasonal thermal energy storage in the LLN groundwater body. It can be utilized by UCLouvain and BSC authorities as a foundation for considering a comprehensive study on the feasibility of implementing an ATES system in LLN.

Future possibilities for expanding this work include: (i) improving the lithostratigraphic model, especially for deeper layers affecting the BSC region's aquifer thickness, (ii) exploring heat transfer performances for other LLN buildings, (iii) adopting vertical model discretization into multiple layers, and (iv) investigating an adaptive system of real-time energy needs Lastly, conducting an economic and environmental study on the system's usage and implications would be valuable to assess the true impact of ATES implementation.

8. References

Anibas, C., Kukral, J., Possemiers, M., & Huysmans, M. (2016). Assessment of Seasonal Aquifer Thermal Energy Storage as a Groundwater Ecosystem Service for the Brussels-Capital Region: Combining Groundwater Flow, and Heat and Reactive Transport Modeling. *Energy Procedia*, *97*, 179–185. https://doi.org/10.1016/j.egypro.2016.10.048

Aquanty. (n.d.). *HydroGeoSphere—Integrated Hydrologic Models*. Aquanty. Retrieved 26 March 2023, from https://www.aquanty.com/hydrogeosphere

Babura, B. I., Adam, M. B., Samad, A. R. A., Fitrianto, A., & Yusif, B. (2018). Analysis and Assessment of Boxplot Characters for Extreme Data. *Journal of Physics: Conference Series*, *1132*(1), 012078. https://doi.org/10.1088/1742-6596/1132/1/012078

Bartosiewicz, Y. (2020). *Introduction aux machines frigorifiques à compression (LBIR1325a, UCLouvain)*.

Bear, J. (1979). *Hydraulics of Groundwater*. Courier Corporation. https://www.google.be/books/edition/Hydraulics_of_Groundwater/ACQsDAAAQBAJ?hl=en&gbpv=1&printsec=frontcover

Bloemendal, M., & Hartog, N. (2018). Analysis of the impact of storage conditions on the thermal recovery efficiency of low-temperature ATES systems. *Geothermics*, *71*, 306–319. https://doi.org/10.1016/j.geothermics.2017.10.009

Bloemendal, M., Jaxa-Rozen, M., & Olsthoorn, T. (2018). Methods for planning of ATES systems. *Applied Energy*, *216*, 534–557. https://doi.org/10.1016/j.apenergy.2018.02.068

Bloemendal, M., & Olsthoorn, T. (2018). ATES systems in aquifers with high ambient groundwater flow velocity. *Geothermics*, *75*, 81–92. https://doi.org/10.1016/j.geothermics.2018.04.005

Boulvain, F., & Pingot, J.-L. (2023). *Une introduction à la GEOLOGIE de la WALLONIE*. https://www.geolsed.uliege.be/upload/docs/application/pdf/2023-02/geolwal.pdf

BRGM. (n.d.). *MARTHE: Modelling software for groundwater flows*. Retrieved 26 March 2023, from https://www.brgm.fr/en/software/marthe-modelling-software-groundwater-flows

Britannica. (n.d.). *Belgium—Temperate, Maritime, Rainfall*. Retrieved 21 July 2023, from https://www.britannica.com/place/Belgium/Climate

Cabeza, L. F. (2020). *Advances in thermal energy storage systems: Methods and applications* (2nd ed.). Woodhead Publishing. https://ils.bib.uclouvain.be/global/documents/3232255

Chiang, W.-H. (2005). *3D-Groundwater Modeling with PMWIN* (Second). Springer-Verlag. https://doi.org/10.1007/3-540-27592-4

Chiang, W.-H., & Kinzelbach, W. (1998). *Processing Modflow—A simulation system for modeling groundwater flow and pollution*. https://ethz.ch/content/dam/ethz/special-interest/baug/ifu/ifu-dam/softwares/pmwin/pm5.pdf

Climat.be. (2019a). *Accord de Paris*. Klimaat | Climat. https://climat.be/politique-climatique/internationale/accord-de-paris

Climat.be. (2019b). *Le climat en Belgique*. Klimaat | Climat. https://climat.be/en-belgique/climat-et-emissions/climat

Couly, B. (2022). *Données piézométriques et géologiques* [dataset].

Dahash, A., Ochs, F., Janetti, M. B., & Streicher, W. (2019). Advances in seasonal thermal energy storage for solar district heating applications: A critical review on large-scale hot-water tank and pit thermal energy storage systems. *Applied Energy*, *239*, 296–315. https://doi.org/10.1016/j.apenergy.2019.01.189

Dahash, A., Ochs, F., & Tosatto, A. (2021). Techno-economic and exergy analysis of tank and pit thermal energy storage for renewables district heating systems. *Renewable Energy*, *180*, 1358–1379. https://doi.org/10.1016/j.renene.2021.08.106

Dassargues, A. (2022). *Formation en modélisation hydrogéologique*. https://orbi.uliege.be/bitstream/2268/295273/2/Burkina_FormMod%C3%A9lisation_Sept2022.pdf

Dassargues, A., & Walraevens, K. (2014). *Watervoerende lagen & grondwater in België = Aquifères & eaux souterraines en Belgique*. Academia. https://ils.bib.uclouvain.be/global/documents/1834353

De Boever, E., Lagrou, D., & Laenen, B. (2012). *Guide de la Géothermie en Belgique*. https://ds.static.rtbf.be/article/pdf/franse_versie_boek_geothermie-1537532771.pdf

de la Varga, M., Schaaf, A., & Wellmann, F. (2019). *GemPy 1.0: Open-source stochastic geological modeling and inversion*. https://gmd.copernicus.org/articles/12/1/2019/gmd-12-1-2019.pdf

de Marsily, G. (1986). *Quantitative hydrogeology: Groundwater hydrology for engineers*. Academic press. https://ils.bib.uclouvain.be/global/documents/259380

DHI. (n.d.). *FEFLOW: All-in-one groundwater modelling solution*. Retrieved 26 March 2023, from https://www.mikepoweredbydhi.com/products/feflow

Domenico, P. A., & Schwartz, F. W. (1998). *Physical and chemical hydrogeology* (2nd ed.). Wiley. https://ils.bib.uclouvain.be/global/documents/817272

Drake Landing Solar Community. (2019, June 30). *Borehole Thermal Energy Storage (BTES): DLSC*. https://www.dlsc.ca/borehole.htm

EPFL. (n.d.). *Chapitre 6: LE STOCKAGE ET SES VARIATIONS (Résumé)*. Retrieved 3 October 2023, from https://echo2.epfl.ch/e-drologie/resumes/chapitre6/resume6.pdf

epsg.io. (2022). *BD72 / Belgian Lambert 72—Belgium—EPSG:31370*. https://epsg.io/31370

Equans Nederland (Director). (2019, March 28). *Animation of seasonal thermal storage | EQUANS*. https://www.youtube.com/watch?v=1f26sfj7uBM

European Parliament. (2018, March 8). *Reducing carbon emissions: EU targets and policies*. https://www.europarl.europa.eu/news/en/headlines/society/20180305STO99003/reducing-carbon-emissions-eu-targets-and-policies

Eurostat. (2020, December 29). *Just over 20% of energy used for heating and cooling is renewable*. Eurostat. https://ec.europa.eu/eurostat/web/products-eurostat-news/-/ddn-20201229-1

Fasbender, D. (2008). *Bayesian data fusion in environmental sciences: Theory and applications* [UCL - Université Catholique de Louvain]. http://hdl.handle.net/2078.1/19713

Fleuchaus, P., Schüppler, S., Bloemendal, M., Guglielmetti, L., Opel, O., & Blum, P. (2020). Risk analysis of High-Temperature Aquifer Thermal Energy Storage (HT-ATES). *Renewable and Sustainable Energy Reviews*, *133*, 110153. https://doi.org/10.1016/j.rser.2020.110153

Foglia, L., Lacopo, B., & Rossetto, R. (n.d.). *Introduction to MODFLOW Packages*. Retrieved 5 November 2023, from https://wis.orasecom.org/content/study/UNESCO/STAS/Meetings/GGRETA%20Phase%202/4%20-%20UNESCO-SADC%20GW%20Modelling%20Training%20-%20March%202017/2%20-%20Presentations/MODFLOW_lecture_2.pdf

Fossoul, F., Orban, P., & Dassargues, A. (2011). *NUMERICAL SIMULATION OF HEAT TRANSFER ASSOCIATED WITH LOW ENTHALPY GEOTHERMAL PUMPING IN AN ALLUVIAL AQUIFER*. https://popups.uliege.be/1374-8505/index.php?id=3228&file=1&pid=3212

Freeze, A., & Cherry, J. (1979). *Groundwater*. Prentice Hall. https://hydrogeologistswithoutborders.org/wordpress/wp-content/uploads/Freeze_and_Cherry_1979-smaller.pdf

Gao, Z., Hu, Z., Chen, T., Xu, X., Feng, J., Zhang, Y., Su, Q., & Ji, D. (2022). Numerical study on heat transfer efficiency for borehole heat exchangers in Linqu County, Shandong Province, China. *Energy Reports*, *8*, 5570–5579. https://doi.org/10.1016/j.egyr.2022.04.012

Géoportail de la Wallonie. (2015, February 17). *Relief de la Wallonie—Modèle Numérique de Terrain (MNT) 2013-2014*. Géoportail de la Wallonie, Le site de l'information géographique wallonne. http://geoportail.wallonie.be/catalogue/6029e738-f828-438b-b10a-85e67f77af92.html

Gringarten, A. C., Landreau, A., Lienhardt, M. J., & Peaudecerf, P. (1976). *ÉTUDE DES POSSIBILITÉS DE STOCKAGE D'EAU CHAUDE EN PROVENANCE DE CENTRALES THERMIQUES*. https://infoterre.brgm.fr/rapports/76-SGN-389-AME.pdf

Hecht-Méndez, J., Molina-Giraldo, N., Blum, P., & Bayer, P. (2010). Evaluating MT3DMS for Heat Transport Simulation of Closed Geothermal Systems. *Groundwater*, *48*(5), 741–756. https://doi.org/10.1111/j.1745-6584.2010.00678.x

IEA. (2023, May). *Belgium Climate Resilience Policy Indicator – Analysis*. IEA. https://www.iea.org/reports/belgium-climate-resilience-policy-indicator

INOWAS. (2018, April 3). *Numerical groundwater modelling and optimization using MODFLOW-2005 – INOWAS*. https://inowas.webspace.tu-dresden.de/t03-modflow-model-setup-and-editor/

IPCC. (1992). *Climate Change: The IPCC 1990 and 1992 Assessments — IPCC*. https://www.ipcc.ch/report/climate-change-the-ipcc-1990-and-1992-assessments/

IRM. (2007). *Rapport annuel 2007*. https://www.google.com/url?sa=t&rct=j&q=&esrc=s&source=web&cd=&cad=rja&uact=8&ved=2ahUKEwj59fejuv6BAxUDh_0HHdt8C3sQFnoECCkQAQ&url=https%3A%2F%2Fwww.meteo.be%2Fmeteo%2Fdownload%2Ffr%2F6189781%2Fpdf%2Firm_web_rapport_annuel_2007.pdf&usg=AOvVaw1_-PArtoupSF8azwgJeNS8&opi=89978449

ISSeP. (2011). *ETUDE LOCALE DES AQUIFERES ET ECOULEMENT SOUTERRAINS AU DROIT DU CENTRE D'ENFOUISSEMENT DE MONT-SAINT-GUIBERT*. http://environnement.wallonie.be/data/dechets/cet/01msg/pdf/01_geo12.pdf

Jenne, E. A. (1992). *Aquifer thermal energy (heat and chill) storage* (PNL-8381; CONF-920801-). Pacific Northwest Lab., Richland, WA (United States). https://www.osti.gov/biblio/6866400

Jesußek, A., Grandel, S., & Dahmke, A. (2012). Impacts of subsurface heat storage on aquifer hydrogeochemistry. *Environmental Earth Sciences*, *69*. https://doi.org/10.1007/s12665-012-2037-9

Jonard, F. (2022). *HYDROLOGIE DES ZONES TROPICALES : TP – QGIS (LSGED2210, UCLouvain)*.

Kalaiselvam, S., & Parameshwaran, R. (2014). *Thermal Energy Storage Technologies for Sustainability*. https://shop.elsevier.com/books/thermal-energy-storage-technologies-for-sustainability/kalaiselvam/978-0-12-417291-

3?country=BE&format=print&utm_source=google_ads&utm_medium=paid_search&utm_campaign=belgiumshopping&gclid=EAIaIQobChMIsKeXyZnf_wIVC4yDBx3vQQ4eEAQYByABEgJ80PD_BwE&gclsrc=aw.ds

Knotters, M., Brus, D. J., & Oude Voshaar, J. H. (1995). A comparison of kriging, co-kriging and kriging combined with regression for spatial interpolation of horizon depth with censored observations. *Geoderma*, *67*(3), 227–246. https://doi.org/10.1016/0016-7061(95)00011-C

Lau, M. J., Zanil, M. F., Choong, S. Y., & Tan, J. (2020). Modelling and optimization of the heat pump system for the usage of swimming pool. *IOP Conference Series: Materials Science and Engineering*, *778*(1), 012097. https://doi.org/10.1088/1757-899X/778/1/012097

Lemlin, G. (2022). *Data on Blocry, given as part of the LBIRE2234 course* [dataset].

Lizana, J., Chacartegui, R., Barrios-Padura, A., & Valverde, J. M. (2017). Advances in thermal energy storage materials and their applications towards zero energy buildings: A critical review. *Applied Energy*, *203*, 219–239. https://doi.org/10.1016/j.apenergy.2017.06.008

Ministerie van de Vlaamse Gemeenschap. (1999). *HYDROLOGISCH JAARBOEK 1999—Ministerie van de Vlaamse Gemeenschap, Administratie Waterwegen en Zeewezen, Afdeling Waterbouwkundig Laboratorium en Hydrologisch Onderzoek*. https://publicaties.vlaanderen.be/view-file/4124

Morway, E., Feinstein, D. T., & Hunt, R. J. (2023). *MODFLOW-NWT, MT3D-USGS, and VS2DH models of 6 hypothetical 1-dimensional variably saturated systems to demonstrate the accuracy of new heat transport capabilities in MT3D-USGS* [Zip]. U.S. Geological Survey. https://doi.org/10.5066/P9PGFNY2

Nalau, J., & Verrall, B. (2021). Mapping the evolution and current trends in climate change adaptation science. *Climate Risk Management*, *32*, 100290. https://doi.org/10.1016/j.crm.2021.100290

Naumann, G. (n.d.). *Climate change impacts of heat and cold extremes on humans*. Retrieved 21 July 2023, from https://joint-research-centre.ec.europa.eu/system/files/2020-09/11_pesetaiv_heat_and_cold_sc_august2020_en.pdf

OECD. (2013). *Transition to Sustainable Buildings: Strategies and Opportunities to 2050*. Organisation for Economic Co-operation and Development. https://doi.org/10.1787/9789264202955-en

Panday, S., Langevin, C., Niswonger, R., Ibaraki, M., & Hughes, J. (2013). *MODFLOW–USG Version 1: An Unstructured Grid Version of MODFLOW for Simulating Groundwater Flow and Tightly Coupled Processes Using a Control Volume Finite-Difference Formulation—Techniques and Methods 6-A45*. https://pubs.usgs.gov/tm/06/a45/

Possemiers, M., Huysmans, M., & Batelaan, O. (2014). Influence of Aquifer Thermal Energy Storage on groundwater quality: A review illustrated by seven case studies from Belgium. *Journal of Hydrology: Regional Studies*, *2*, 20–34. https://doi.org/10.1016/j.ejrh.2014.08.001

Rapantova, N., Pospisil, P., Koziorek, J., Vojcinak, P., Grycz, D., & Rozehnal, Z. (2016). Optimisation of experimental operation of borehole thermal energy storage. *Applied Energy*, *181*, 464–476. https://doi.org/10.1016/j.apenergy.2016.08.091

Razas, M. A., Hassan, A., Khan, M. U., Emach, M. Z., & Saki, S. A. (2023). A critical comparison of interpolation techniques for digital terrain modelling in mining. *Journal of the Southern African Institute of Mining and Metallurgy*, *123*(2), 53–62. https://doi.org/10.17159/2411-9717/2271/2023

Ruthy, I., Dassargues, A., Rekk, S., & Hallet, V. (2017). *Carte hydrologique de Wallonie—Notice explicative: Wavre—Chaumont-Gistoux*. http://environnement.wallonie.be/cartosig/cartehydrogeo/document/Notices/4012.pdf

Sénat. (2016, July 20). *Mise en oeuvre de l'accord de Paris sur le climat*. Sénat. https://www.senat.fr/ue/pac/EUR000002464.html

Shackelford, C. D. (2013). Geoenvironmental Engineering☆. In *Reference Module in Earth Systems and Environmental Sciences*. Elsevier. https://doi.org/10.1016/B978-0-12-409548-9.05424-5

Simcore Software. (2012). *Processing Modflow 8—An Integrated Modeling Environment for the Simulation of Groundwater Flow, Transport and Reactive Processes*. https://www.simcore.com/files/pm/v8/pm8.pdf

Simcore Software. (2022). *Processing Modflow 11*. https://www.simcore.com/files/pm/v11/pm11.0.4.pdf?a=2022071101

Simcore Software. (2021). *Previous Versions*. https://www.simcore.com/wp/archive/

Simcore Software. (2023). *Processing Modflow 11*. https://www.simcore.com/wp/processing-modflow-11/

Sommer, W., Valstar, J., van Gaans, P., Grotenhuis, T., & Rijnaarts, H. (2013). The impact of aquifer heterogeneity on the performance of aquifer thermal energy storage. *Water Resources Research*, *49*(12), 8128–8138. https://doi.org/10.1002/2013WR013677

Spitzer, M., Wildenhain, J., Rappsilber, J., & Tyers, M. (2014). BoxPlotR: A web tool for generation of box plots. *Nature Methods*, *11*(2), Article 2. https://doi.org/10.1038/nmeth.2811

SPW. (2010). *Etat des lieux de la masse d'eau RWE053 « Sables du Landénien (Est)»*. http://eau.wallonie.be/fme/RWE053.pdf

Squilbin, A., Mulligan, F., Dame, H., Vander Linden, A., & Duy Thang, T. D. (2022). *Étude des enjeux de sobriété et d'efficacité thermique du centre sportif de Blocry (dans l'encadrement du cours LBIRE2234 dispensé à l'UCLouvain)*.

Tatsidjodoung, P., Le Pierrès, N., & Luo, L. (2013). A review of potential materials for thermal energy storage in building applications. *Renewable and Sustainable Energy Reviews*, *18*, 327–349. https://doi.org/10.1016/j.rser.2012.10.025

Tiéry, D. (2016). *Modélisation 3D du transport de masse et du transfert thermique avec le code de calcul MARTHE (version 7.5)*. https://www.brgm.fr/sites/default/files/documents/2020-11/logiciel-marthe-transport-masse-7-5-rp-64765-fr.pdf

UCLouvain. (2021). *Plan transition*. UCLouvain. https://uclouvain.be/fr/decouvrir/universite-transition/plan-transition.html

UCLouvain. (2022). *Distribution d'eau à Louvain-la-Neuve*. UCLouvain. https://uclouvain.be/fr/administrations/adpi/distribution-eau-lln.html

UNFCCC. (1995). *CONFERENCE OF THE PARTIES: First session*. https://unfccc.int/cop3/resource/docs/cop1/01.htm

United Nations. (n.d.). *L'Accord de Paris | CCNUCC*. Retrieved 11 March 2023, from https://unfccc.int/fr/a-propos-des-ndcs/l-accord-de-paris

USGS. (n.d.-a). *EarthExplorer*. Retrieved 15 October 2023, from https://earthexplorer.usgs.gov/

USGS. (n.d.-b). *Online Guide to MODFLOW-2005—WEL (Well Package)*. Retrieved 21 September 2023, from https://water.usgs.gov/ogw/modflow/MODFLOW-2005-Guide/wel.html

USGS. (2022, March 3). *MODFLOW and Related Programs*. USGS Science for Changing World. https://www.usgs.gov/mission-areas/water-resources/science/modflow-and-related-programs

Valstar, J., & Hoekstra, N. (n.d.). *Geothermal energy: Proven way of sustainable energy production | Deltares*. Retrieved 10 March 2023, from https://www.deltares.nl/en/expertise/areas-of-expertise/energy-transition/aquifer-thermal-energy-storage

Velraj, R. (2016). 15—Sensible heat storage for solar heating and cooling systems. In R. Z. Wang & T. S. Ge (Eds.), *Advances in Solar Heating and Cooling* (pp. 399–428). Woodhead Publishing. https://doi.org/10.1016/B978-0-08-100301-5.00015-1

Vidal, R., Olivella, S., Saaltink, M. W., & Diaz-Maurin, F. (2022). Heat storage efficiency, ground surface uplift and thermo-hydro-mechanical phenomena for high-temperature aquifer thermal energy storage. *Geothermal Energy*, *10*(1), 23. https://doi.org/10.1186/s40517-022-00233-3

Wallonie.be. (n.d.-a). *Auteurs Agréés d'Études d'Incidences—Catégories*. Retrieved 20 May 2023, from http://environnement.wallonie.be/cgi/dgrne/dppgss/aeie01.idc

Wallonie.be. (n.d.-b). *Outil de recherche des rubriques—Rubrique 41.00.04*. Retrieved 27 April 2023, from http://environnement.wallonie.be/cgi/dgrne/aerw/pe/__drup/rub_form.idc?chx_rubri=41.00.04

Wallonie.be. (2005). *MASSE D'EAU SOUTERRAINE RWE160—SOCLE DU BRABANT*. http://eau.wallonie.be/fme/RWE160.pdf

Wallonie.be. (2006). *MASSE D'EAU SOUTERRAINE RWE051—SABLES DU BRUXELLIEN*. http://eau.wallonie.be/fme/RWE051.pdf

Wallonie.be. (2023). *Niveau d'eau souterraine*. https://piezometrie.wallonie.be/home/observations/niveau-deau-souterraine.html?mode=table&search=sables

WATERINFO.be. (2023a). *Discharge (High resolution)—Stationnaam Wilsele/Dijle*. https://www.waterinfo.be/Meetreeksen?KL=en

WATERINFO.be. (2023b). *Waterlevel (High resolution)*. https://www.waterinfo.be/Meetreeksen?KL=en

Waterloo Hydrogeologic. (2023a). Groundwater Flow & Contaminant Transport Modeling Software. *Waterloo Hydrogeologic*. https://www.waterloohydrogeologic.com/products/visual-modflow-flex/

Waterloo Hydrogeologic. (2023b). Visual MODFLOW Flex. *Waterloo Hydrogeologic*. https://www.waterloohydrogeologic.com/product/visual-modflow-flex/

Weather Spark. (n.d.). *Climate and Average Weather Year Round in Louvain-la-Neuve (Belgium)*. Retrieved 21 July 2023, from https://weatherspark.com/y/51061/Average-Weather-in-Louvain-la-Neuve-Belgium-Year-Round

Woessner, W. W., & Poeter, E. P. (2020). *Specific Yield and Specific Retention*. https://books.gw-project.org/hydrogeologic-properties-of-earth-materials-and-principles-of-groundwater-flow/chapter/specific-yield-and-specific-retention/

Xu, J., Li, Y., Wang, R. Z., & Liu, W. (2014). Performance investigation of a solar heating system with underground seasonal energy storage for greenhouse application. *Energy*, *67*, 63–73. https://doi.org/10.1016/j.energy.2014.01.049

Yerdesh, Y., Toleukhanov, A., Mohanraj, M., Wang, H. S., Botella, O., Feidt, M., & Belyayev, Y. (2022). *Air-to-Water Cascade Heat Pump Thermal Performance Modelling for Continental Climate Regions*. *3*. https://doi.org/10.21494/ISTE.OP.2022.0836

Zheng, C., & Wang, P. P. (1999). *MT3DMS: A Modular Three-Dimensional Multispecies Transport Model for Simulation of Advection, Dispersion, and Chemical Reactions of Contaminants in Groundwater Systems; Documentation and User's Guide*. https://hydro.geo.ua.edu/mt3d/mt3dmanual.pdf

9. Appendices

9.1. Legislative aspects (related to the installation of the ATES system)

N.B. The informations provided below are based on preliminary research and may not be exhaustive.

9.1.1. Authorisations and licenses

In Wallonia, the implementation of an aquifer storage system requires specific authorisations. The concerned category for the project is section 41.00.04 ("Installation for the recharge or artificial recharge testing of groundwater"), classified in category 7 ("Water Management") (De Boever et al., 2012; Wallonie.be, n.d.-b, n.d.-a).

This section is also classified as class 1, indicating that the project may have a significant impact on the environment, requiring an application for an environmental permit (EP) and the completion of an environmental impact assessment (EIA). To initiate this process, various documents must be completed (Wallonie.be [a], n.d.):

- Two forms must be completed for this section of project:
  - "General Form for Environmental Permit and Single Permit".
  - "Form related to water intakes, drilling, well equipment, and for the recharge or artificial recharge testing of groundwater".
- 3 forms must be added in the case of a SEVESO establishment (i.e. linked to dangerous substances):
  - "Contents of the hazard identification notice in accordance with Article 61, § 1 and 3".
  - "Form relating to the structure and content of safety studies in accordance with Article 61, § 2 and § 3".
  - "Information on the criteria for determining the concepts of significant involvement, increase, significant change and process modification in accordance with Article 61, §4".

9.1.2. Protection zones

Consideration must also be given to protection zones within a legal framework. Perimeter zones are established to mitigate the risks of contamination of catchments (Ruthy et al., 2017). These areas involve the creation of zones progressively farther from the catchments (cf. Figure 26):

The **first zone** is the water intake zone, extending up to a distance of 10 meters from the catchment. Within this zone, only activities directly related to water production are allowed.

Following this are prevention zones, representing the geographical area in which the extraction well can be reached by any pollutant without sufficient degradation or dissolution and without effective recovery. It is divided into two zones: the close prevention zone (**zone 2a**) located at a distance corresponding to 24 hours of flow in a saturated environment (or 35 meters if data are insufficient). The distant prevention zone (**zone 2b**) has its limit at 50 days of flow in a saturated environment (or 100 m in a sandy aquifer if data are insufficient).

Finally, the **third zone** is the monitoring zone, which covers the entire hydrogeological basin upstream of the catchment.

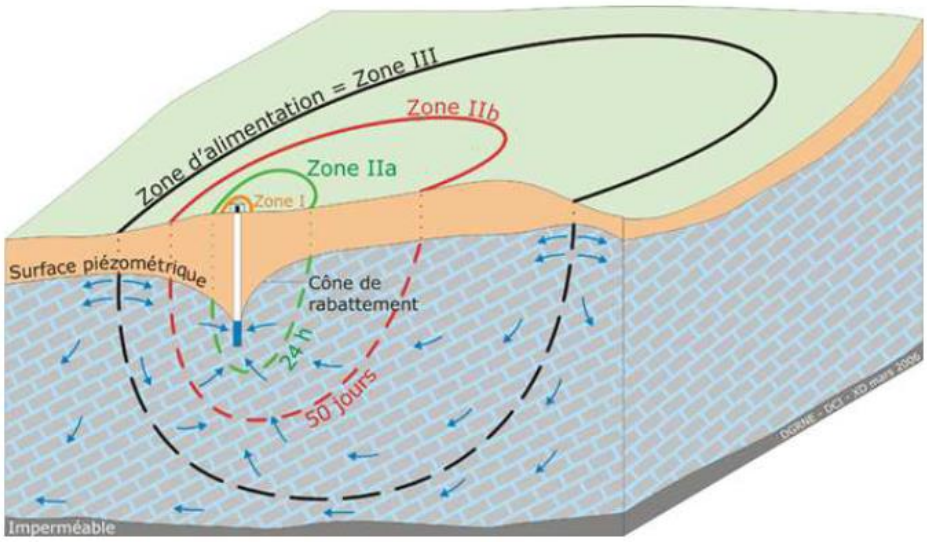

Figure 26 - Protection zones in the Walloon Region (Ruthy et al., 2017)

9.2. Further information about the lithostratigraphic model

9.2.1. Additional information about the methodology

9.2.1.1. Example of a piezometer description file (S20)

IDENTIFICATION

PIEZOMETRES UCL

FICHES DESCRIPTIVES

N° **S20**

Nom **PC1 piézo 1 (proche) (tour)**

LOCALISATION

Adresse :
Chemin du cyclotron, 1 B-1348 Louvain-la-Neuve

Commentaire(s) :
Piézo PC1 (proche) à côté de la tour de refroidissement du cyclotron

Coordonnées Lambert 72

X	168007,961	Mesurées	X
Y	150485,658	Estimées	
Z	147,35		

FORAGE & EQUIPEMENT

Date du forage :	5/05/1971	
Mesuré actuellement :	Mensuellement	
Télémesuré :	Non	
Etat actuel :	Ok	
Exploité actuellement :	OUI	
Côte altimétrique :	147,3	m
Profondeur du forage :	56,5	m
Longueur tube aveugle :	51,5	m
Longueur de la crépine :	5	m
Diamètre tube intérieur :	0,06	m
Niveau statique :	35,6	m
Repère pour la mesure :	Rebord béton de la taque	

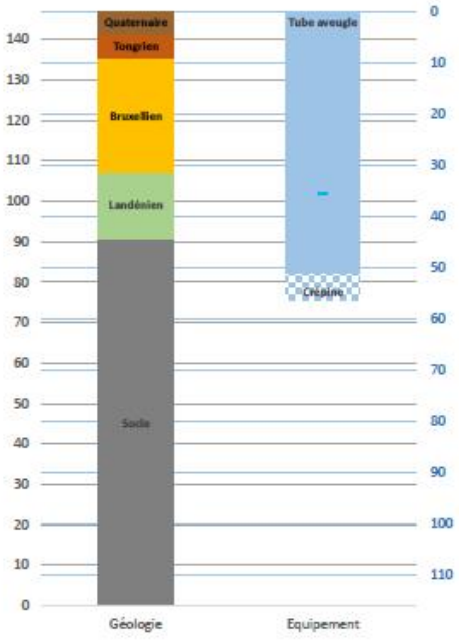

GEOLOGIE

Quaternaire	0	à	6,0	m, soit	6,00 m
Tongrien	6	à	12,0	m, soit	6,00 m
Bruxellien	12	à	40,0	m, soit	28,00 m
Landénien	40	à	56,5	m, soit	16,50 m
Socle	57	à	112,0	m, soit	55,51 m

CHRONIQUE PIEZOMETRIQUE

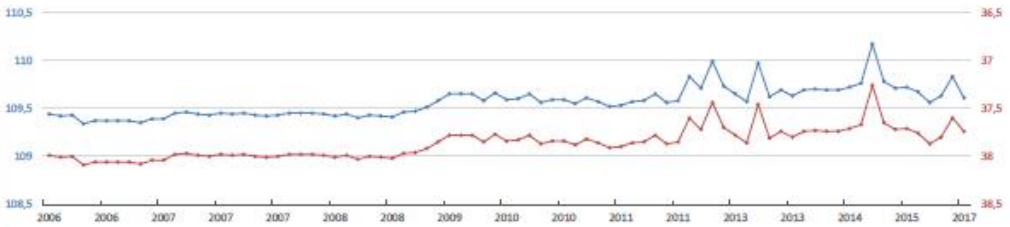

9.2.1.2. List of retained and removed piezometers for the lithostratigraphic model

30 retained piezometers: S19; S20; S21; S22; S24; S25; S26; S28; S29; S30; S36; S39; S40; S45; S47; S48; S49; S50; S58; S59; S60; S63; S64; S65; S70; S71; S72; S73; S74 & S241.

8 removed piezometers: S42; S51; S61; S62; S66; S67; S68; S69.

9.2.1.3. Belgian Lambert 72 - Belgium

Table 10 - Transformation of the coordinates of the origin (0;0) of the " Belgian Lambert 1972" system (epsg.io, 2022)

	Belgian Lambert 1972	**World Geodetic System 1984**
Longitude (X)	0 m	2°18'24.081" E
Latitude (Y)	0 m	49°17'36.007" N

Figure 27 – Limits of the Belgian Lambert 72 projection (epsg.io, 2022)

The origin of the BL72 projection is located far from LLN, approximately 45 km north of Paris in France.

9.2.2. Additional results

9.2.2.1. Additional figures and tables

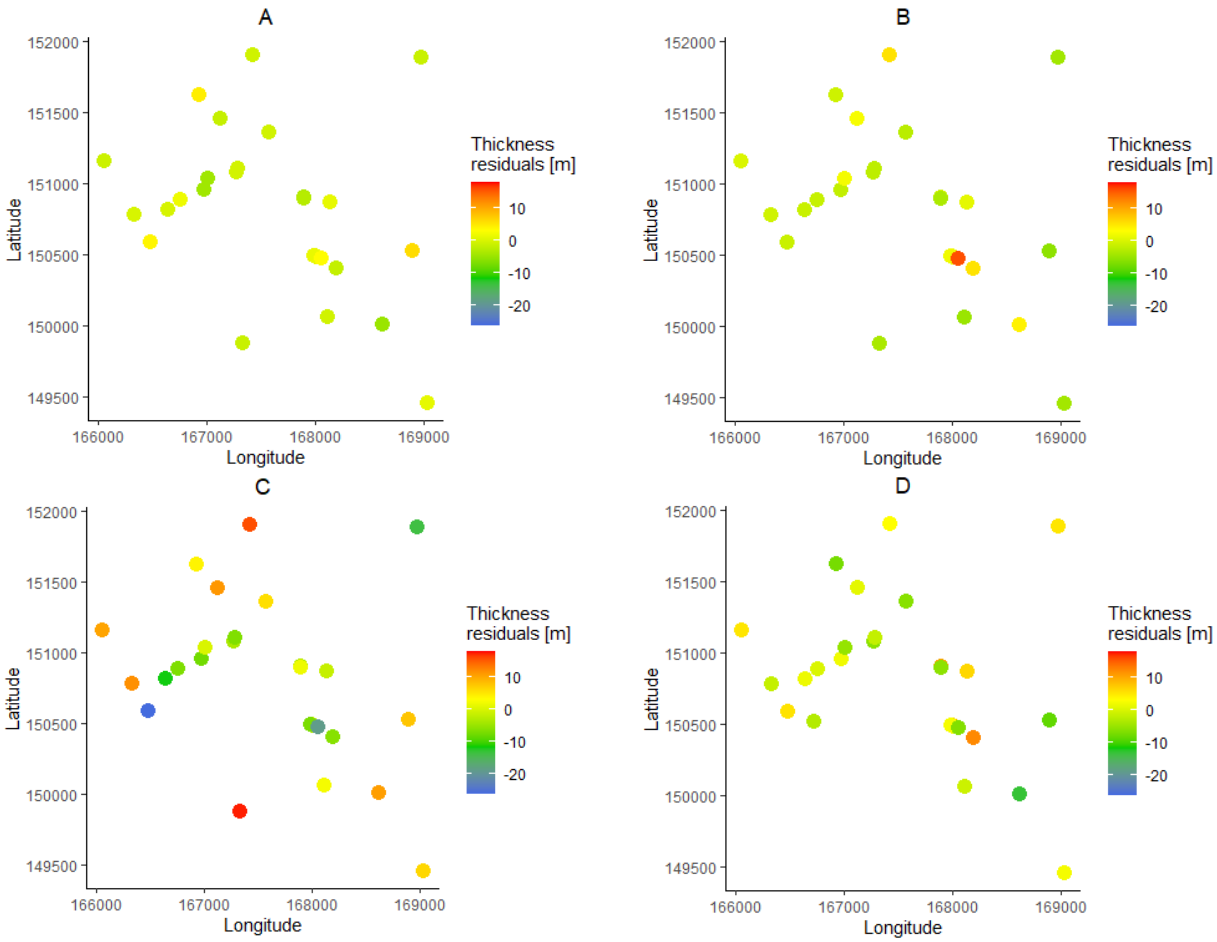

Figure 28 - Residuals from different geological layers at piezometer locations (A: Quaternary, B: Tongrian, C: Bruxellian, D: Landenian)

The linear trends in thickness residuals shown in Figure 28 correspond to an almost horizontally sloped plane due to the very distant from OLLN origin (cf. Table 10 in Appendix 9.2.1.3) (epsg.io, 2022). Figure 28 emphasizes the substantial thickness of the values for the Bruxellian layer compared to all other layers, where residuals appear more similar. This differentiation is also observable, to a lesser extent, for the Landenian layer.

Table 11 - Extreme variance values on the prediction grid

Geological layers	**Residuals variance [m²]**	
	Min	**Max**
Quaternary	0.50	8.10
Tongrian	0.40	9.41
Bruxellian	39.09	148.60
Landenian	32.92	90.93

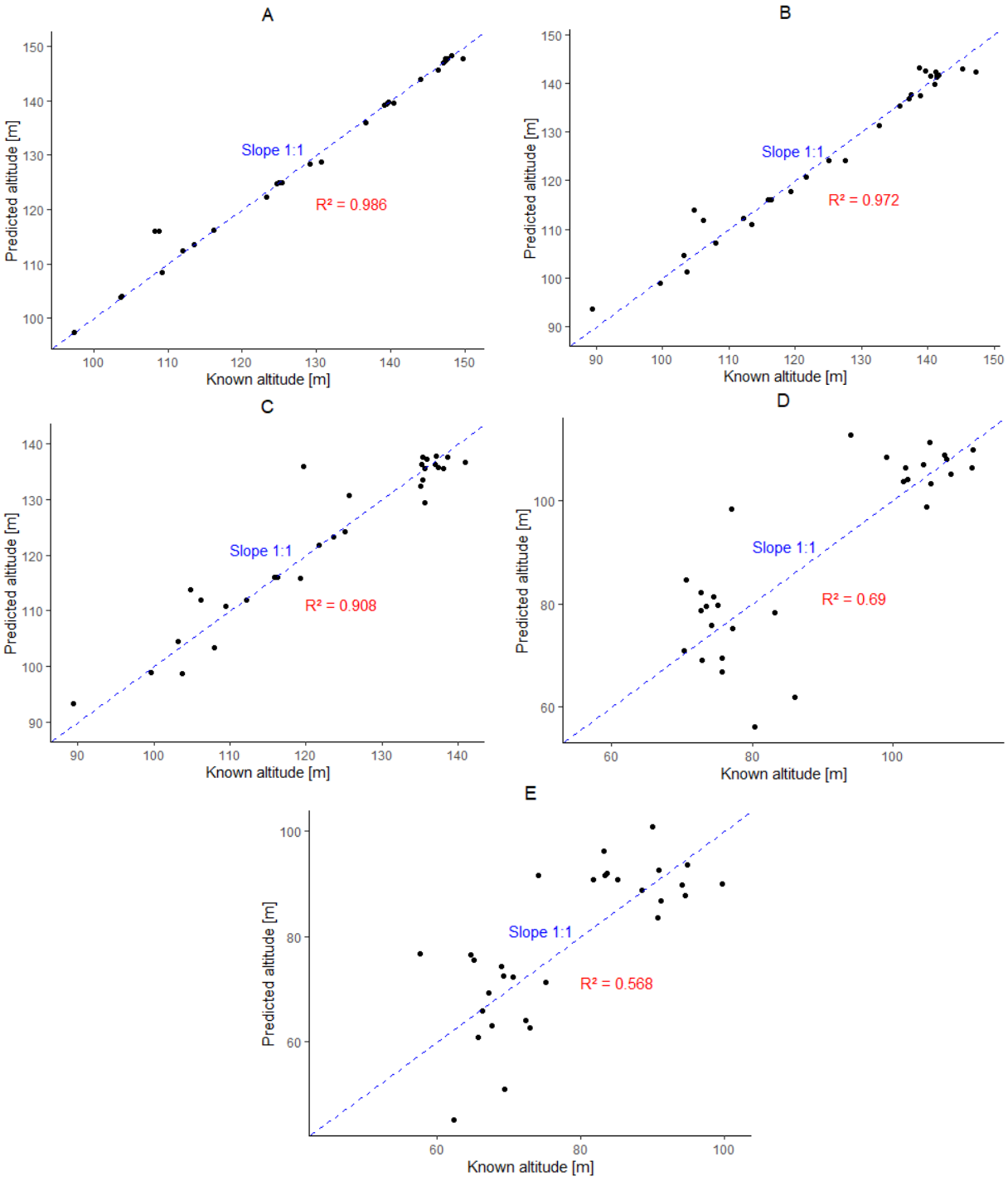

Figure 29 - Known and predicted layer altitude (A: Quaternary, B: Tongrian, C: Bruxellian, D: Landenian, E: Bedrock)

In Figure 29, the R^2 (coefficient of determination) values consider the differences between the predicted altitude values and the known values: it assesses the quality of the prediction model's fit to the observed data.

9.2.2.2. Uncertainty on thickness prediction

The Table 12 shows the general statistics calculated for each of the layers, and Table 13 shows the variance statistics of the LOOCV thickness prediction.

Table 12 - Thickness prediction quality statistics (all data)

Geological layer	RMSE [m]	R^2	SSE [m^2]
Quaternary	2.13	0.38	136.42
Tongrian	3.72	0.32	414.04
Bruxellian	9.82	0.17	2893.59
Landenian	6.51	0.24	1270.53

Table 13 - Variances statistics of LOOCV thickness prediction

Geological layer	Variance [m^2]		
	Minimum	Average	Maximum
Quaternary	0.26	5.22	8.12
Tongrian	0.29	5.23	9.46
Bruxellian	40.43	68.62	151.26
Landenian	33.71	42.75	82.91

This Table 12 shows that the R^2 values are quite low, because the predicted thicknesses do not correspond very much to those expected, as shown in Figure 30, which compares the values with each other. However, the prediction is the best for the Quaternary, followed by the Tongrian and the Landenian, and finally the Bruxellian, which is the layer for which the coefficient of determination is the smallest: indeed, the same conclusion can be made from Table 13 showing the variance of the prediction.

The statistics analysing the prediction errors (such as RMSE and SSE) show the same thing: the errors are, ranked from lowest to highest, the Quaternary, the Tongrian, the Landenian and finally the Bruxellian.

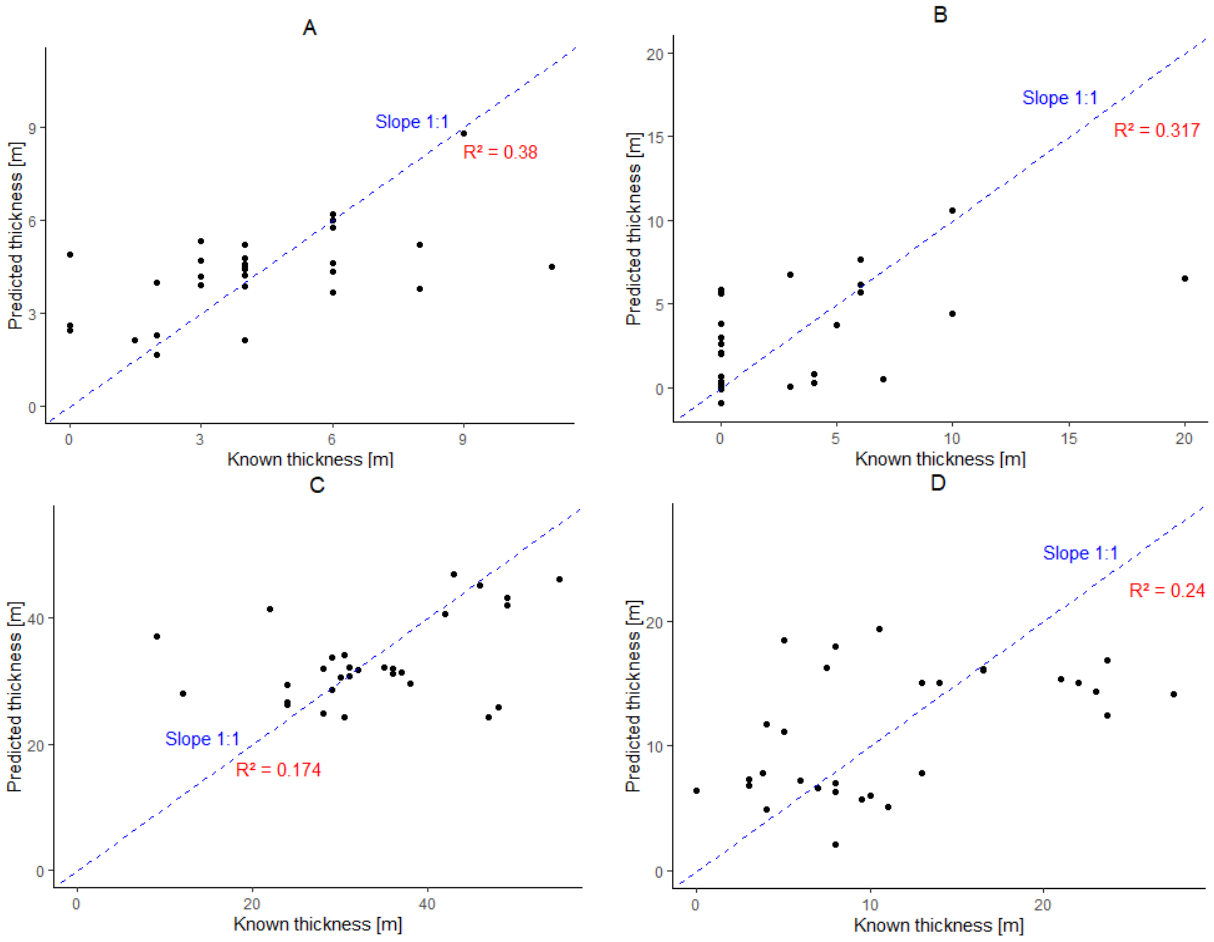

Figure 30 - Known and predicted layer thickness (A: Quaternary, B: Tongrian, C: Bruxellian, D: Landenian)

Figure 30 displays that the predicted thicknesses can be very different from one to another. The R^2 values (coefficient of determination) consider the differences between the predicted altitude values and the known values: it assesses the quality of the prediction model's fit to the observed data.

Figure 31 shows the difference calculated from the known and predicted data for each of the piezometers.

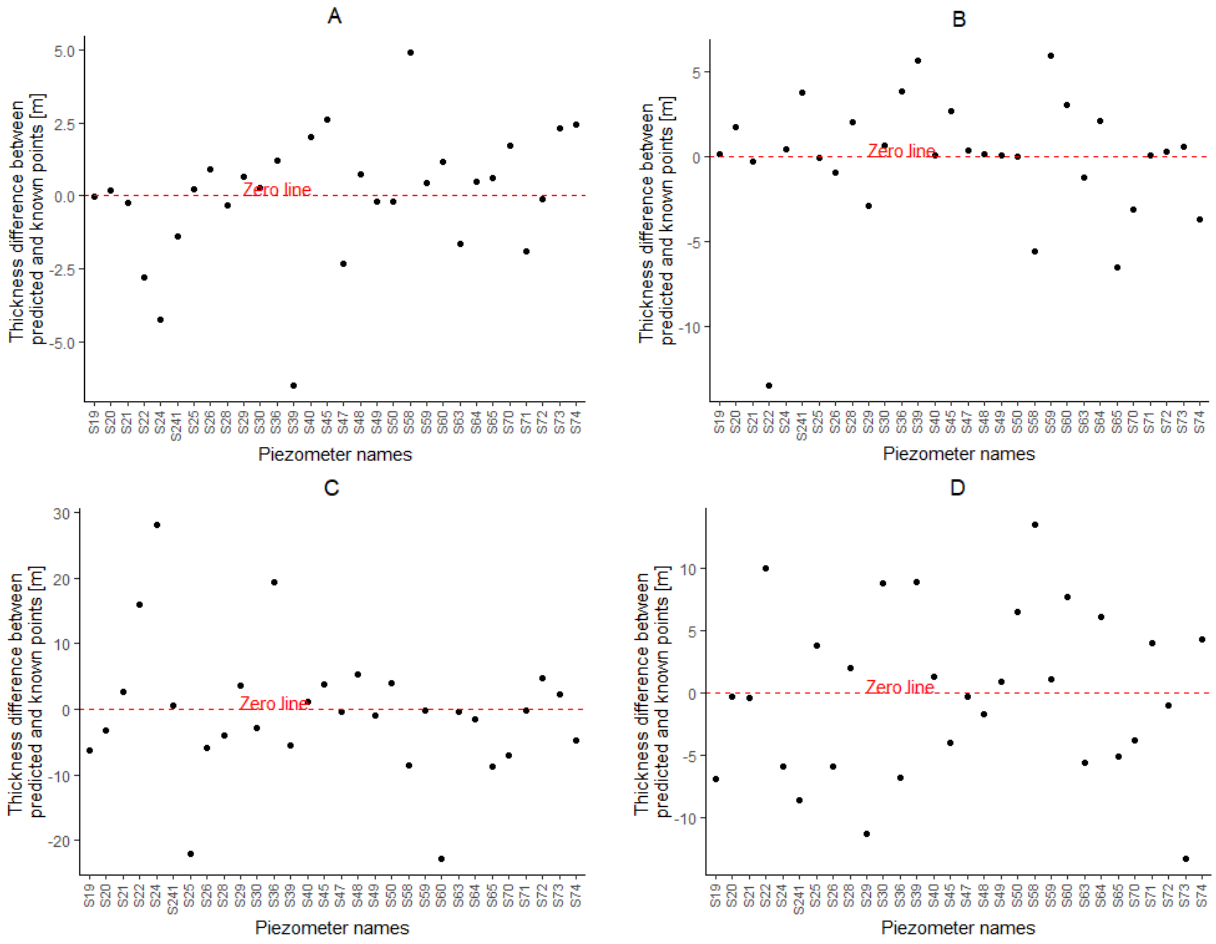

Figure 31 - Difference between predicted and known thicknesses of each layer by piezometer (A: Quaternary, B: Tongrian, C: Bruxellian, D: Landenian)

Negative differences in Figure 31 mean that the predicted thickness is too thin compared with the measured thickness, which will result in a positive difference in altitude (altitude too high compared with what is expected). Inversely, when the difference is positive (i.e. the predicted thickness is too high compared with that expected), the predicted altitude will be too small and the difference will therefore be a negative value (cf. Figure 12). Of course, when the difference is zero here, the difference in altitude of the previous layer will be transmitted on to the new layer.

Figure 31 shows that the differences are limited to around 5 meters maximum for the Quaternary and the Tongrian, with the exception of piezometer S39 for the Quaternary and S22 for the Tongrian, which are more negative. These are the two piezometers that were identified as outliers in section 5.3.2.2.

For the Bruxellian and the Landenian, most of the points are limited to a difference of 10 meters, but some of them are much further from the reality measured in the field (In the case of the Bruxellian, these are the differences obtained for piezometers S22; S24; S25; S36 and S60). For the Landenian, the maximum differences are of the order of 10 meters, but few of

them are actually very small (close to the "zero line"). However, 3 of them are more than 10 meters distant (these are the points corresponding to piezometers S29; S58 and S73).

And after having removing the points that were outliers (S39 for the Quaternary and S22 for the Tongrian), the statistics become as shown in Table 14.

Table 14 - Thickness prediction quality statistics (without outliers)

Geological layer	RMSE [m]	R^2	SSE [m^2]
Quaternary	1.80	0.47	94.34
Tongrian	2.83	0.33	232.23

Table 14 shows that the statistics have been globally improved compared to Table 12. For the Quaternary, the R^2 increased quite nicely and the RMSE and SSE decreased a little bit. Similarly for the Tongrian, the errors are smaller but the R^2 is not significantly increased, because although the point removed is far from the line with slope 1 (cf. Figure 32), the other remaining points are not well predicted and still generate a significant error.

However, the SSE values are not comparable because fewer points are taken into account, so the total error can only be smaller. On the other hand, the RMSE is still valid because it is based on an average.

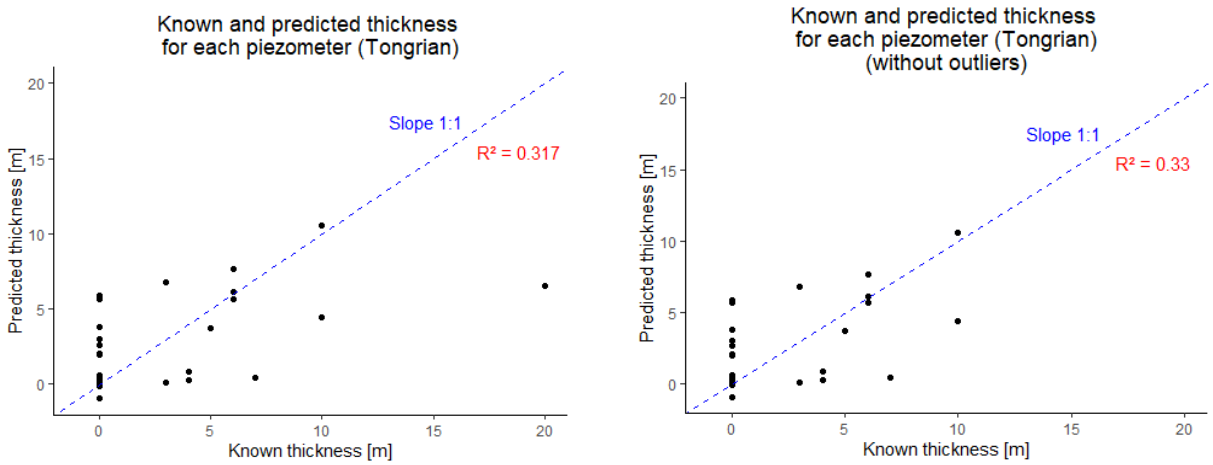

Figure 32 - Impact of the removal of the outlier S22 on Tongrian statistics

9.3. Additional MODFLOW models input data

9.3.1. Digital Terrain Model centred on the catchment area

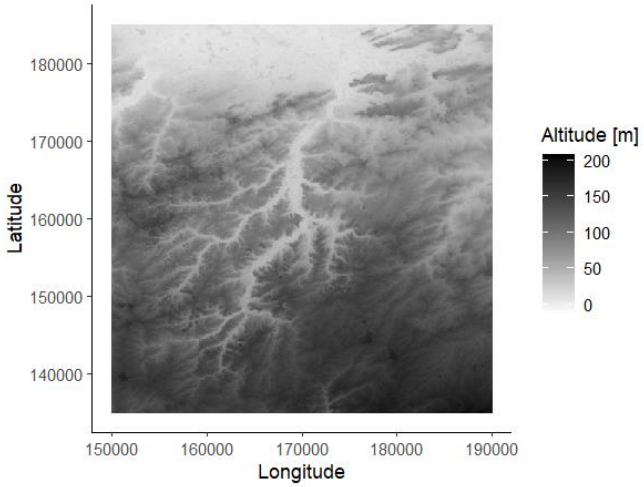

Figure 33 - Surface altitude (USGS) with 100 m resolution, centred on the catchment area

9.3.2. Piezometric data used for MODFLOW model calibration

List of piezometers used

1) Catchment-scale model

- S21; S22; S24; S25; S28; S36; S42; S50; S51; S58; S59; S61; S62; S63; S64; S65; S66; S67; S68; S70; S73; S74; S241.
- PZ3454; PZ83; PZ6677; PZ84; PZ7057; PZ2835; PZ6728; PZ1099; PZ6565
- No observations were considered for the Flemish part of the catchment area because the (altitude) reference may vary depending on the piezometers (WATERINFO.be, 2023b).

2) Study area-scale model

- S20; S21; S22; S24; S25; S26; S28; S30; S36; S39; S42; S45; S47; S48; S50; S51; S58; S59; S60; S61; S62; S63; S64; S65; S66; S67; S68; S69; S70; S71; S72; S73; S74; S241.

Piezometers data

Table 15 - Piezometers used for calibration of the MODFLOW models (Couly, 2022; Wallonie.be, 2023)

Location	Piezometers name	Coordinates		Z [m] (altitude)	Average water altitude [m]
		X [m]	Y [m]		
Study area (centred on LLN)	S20	169031.43	149454.28	147.120	109.59
	S21	167985.85	150494.47	147.274	109.34
	S22	168054.51	150474.45	147.651	110.52
	S24	166476.41	150590.31	97.423	88.4
	S25	166328.56	150785.16	129.009	86.49
	S26	166057.02	151156.00	124.694	83.14

	S28	167896.25	150901.35	139.446	106.85
	S30	167897.91	150891.12	139.075	107.25
	S36	168971.50	151891.39	112.506	95.98
	S39	168888.56	150524.55	149.693	115.40
	S42	166601.47	150559.67	100.451	98.64
	S45	166980.28	150958.81	103.740	88.84
	S47	166754.64	150883.67	109.170	88.50
	S48	166642.59	150819.56	103.662	88.16
	S50	166931.99	151624.45	124.883	84.55
	S51	166952.35	151602.80	125.367	85.62
	S58	168620.63	150011.17	147.137	114.44
	S59	168107.50	150065.02	139.721	112.64
	S60	167328.01	149878.83	143.971	104.31
	S61	166863.43	150664.08	107.531	90.54
	S62	166721.50	150519.40	108.383	90.5
	S63	168133.81	150870.56	146.338	109.8
	S64	167574.25	151364.76	123.261	89.48
	S65	167420.98	151905.20	136.673	87.48
	S66	168203.62	150326.55	146.706	112.05
	S67	168253.95	150448.47	148.169	111.94
	S68	167661.16	150664.84	142.259	106.2
	S69	168175.00	150429.00	148.830	111.12
	S70	167127.51	151458.89	130.597	88.52
	S71	167271.00	151084.00	108.790	87.51
	S72	167290.41	151104.45	116.149	88.10
	S73	168189.64	150402.56	148.158	110.63
	S74	167009.84	151039.71	113.518	88.21
	S241	169031.43	149454.28	147.120	117.02
Water catchment area	PZ83	174572	146165	158.96	148.655
	PZ84	155330	151170	130.89	97.025
	PZ1099	161849	139515	156.86	133.825
	PZ2835	160280	150020	134.07	92.31
	PZ3454	172411	157358	69.08	46.85
	PZ6565	154870	146950	144.66	127.605
	PZ6677	156327	154031	122.74	73.135
	PZ6728	169489	157813	40.17	40.185
	PZ7057	160504	152858	124.55	84.985

9.4. Piezometric maps of the Brussels sands aquifer

Figure 34 (centred on LLN) and Figure 35 (located north of LLN), allow result comparisons. They show piezometric curves similar to those in Figure 13, parallel to the Dyle, but influenced by others river or valley impacts. For instance, in east of LLN, the aquifer partially flows towards the east, drained by the Train, located outside the model's catchment area.

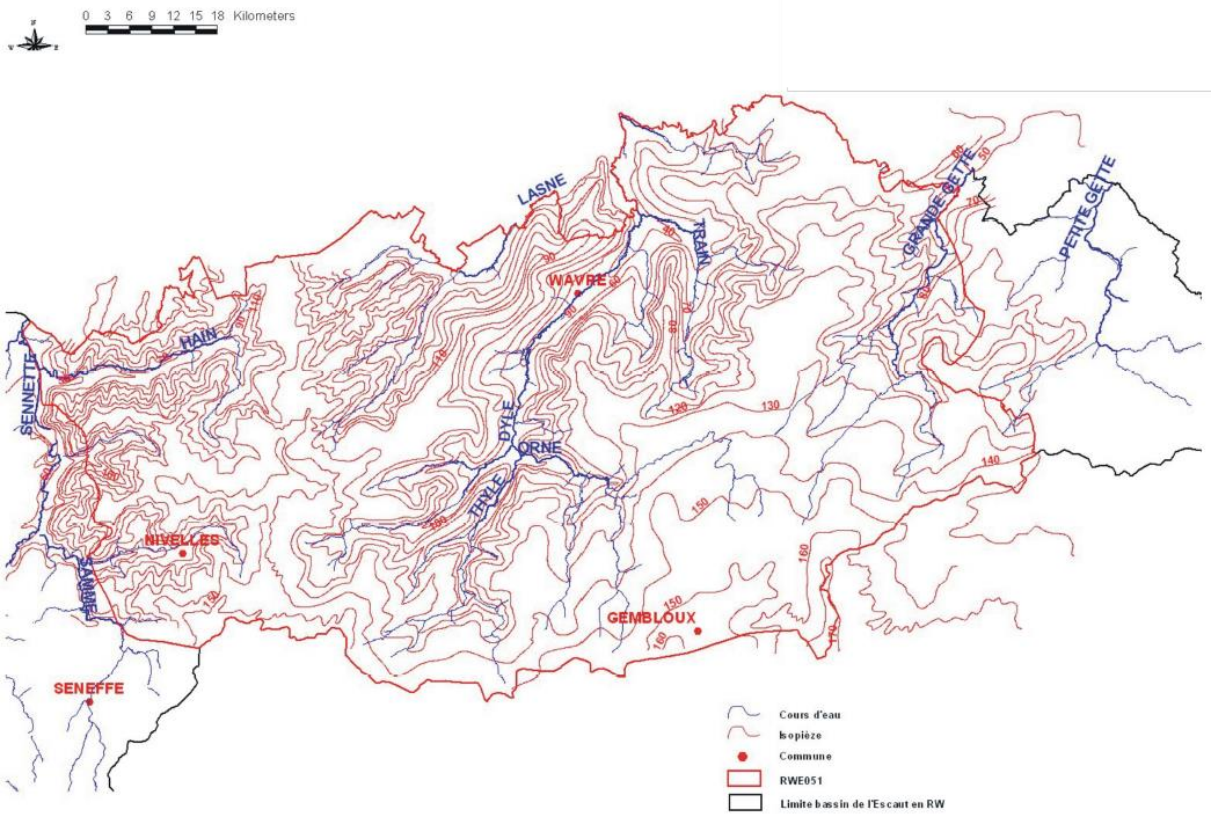

Figure 34 – Piezometric maps of the Brussels sands aquifer (RWE051) (Wallonie.be, 2006)

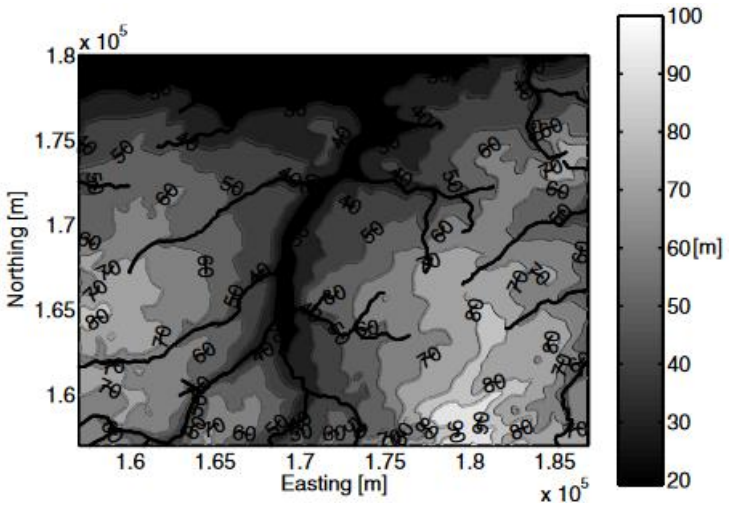

Figure 35- Prediction of the water table using the Bayesian data fusion approach (Fasbender, 2008)

9.5. Additional thermal plumes results regarding the implementation of an ATES system for the Blocry Sport Centre

This appendix presents figures illustrating the temporal evolution of thermal plumes in the groundwater body of LLN. Table 16 summarizes the input parameters for each of the studied scenarios.

Table 16 – Summary of modelling parameters for various scenarios in Appendix 9.5 (sensitivity analysis). Specific characteristics of each scenario are highlighted in bold.

Appendix	ATES system operating flow rate [m³/d]	Start of modelling	Injection temperature during the 1st season [°C]	Injection temperature during the 3rd season [°C]
9.5.1	100	Summer	20	5
		Winter	5	20
9.5.2	100	Summer	**15**	5
		Winter	5	**15**
9.5.3	100	Summer	**25**	5
		Winter	5	**25**
9.5.4	**50**	Summer	20	5
		Winter	5	20
9.5.5	**200**	Summer	20	5
		Winter	5	20

9.5.1. Initial configuration of the studied ATES system

The results of the operation of the ATES system with a flow rate of 100 m³/d, injecting water at 20°C in summer and 5°C in winter, are provided below. This corresponds to the initial studied scenario. Figure 36 shows the results over 3 years with a monthly temporal resolution, starting the modelling at the beginning of summer. Figure 37 displays the results for one year of modelling, starting at the beginning of winter, with a 3-month temporal resolution.

Year 1, Season 1: Summer period

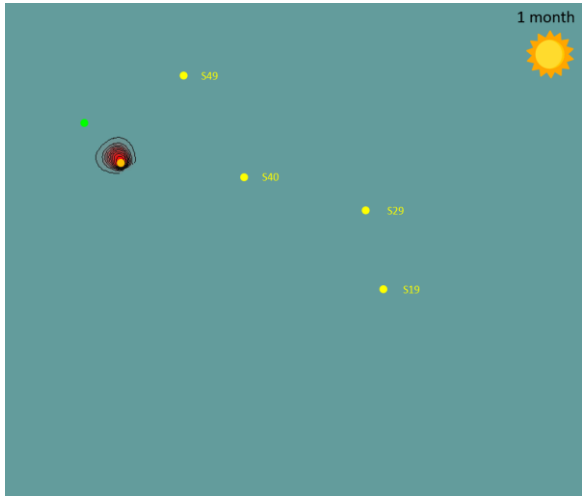

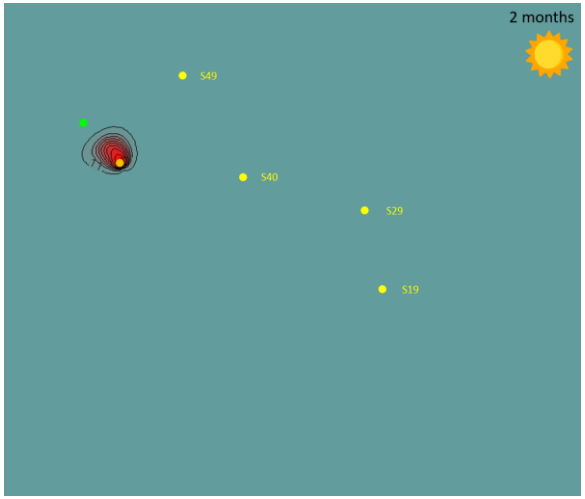

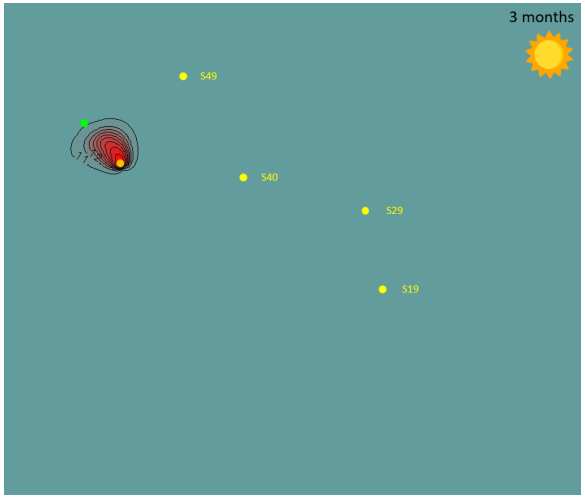

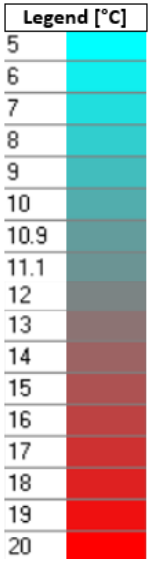

Year 1, Season 2: Autumn period (Interseasonal regime)

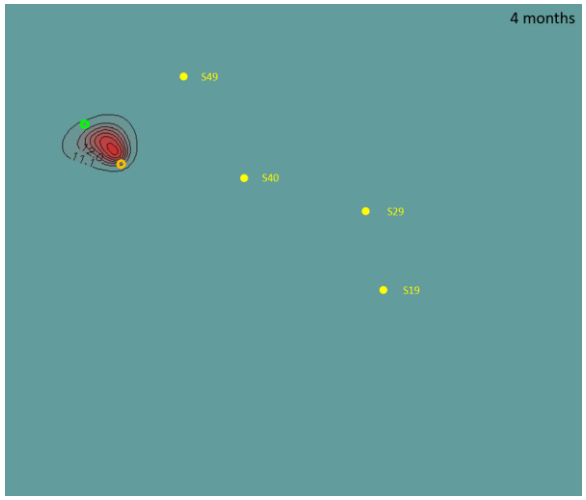

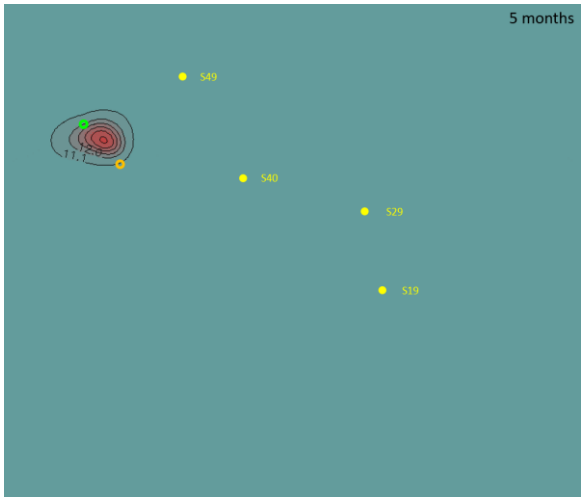

Active water injection
Inactive water injection
Extraction wells
Active water pumping
Inactive water pumping

Year 1, Season 3: Winter period

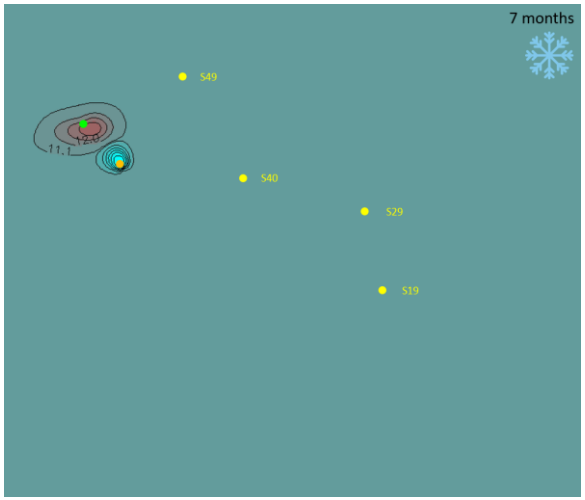

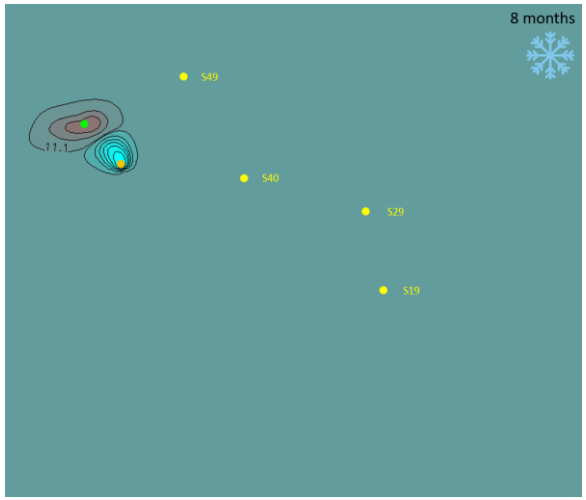

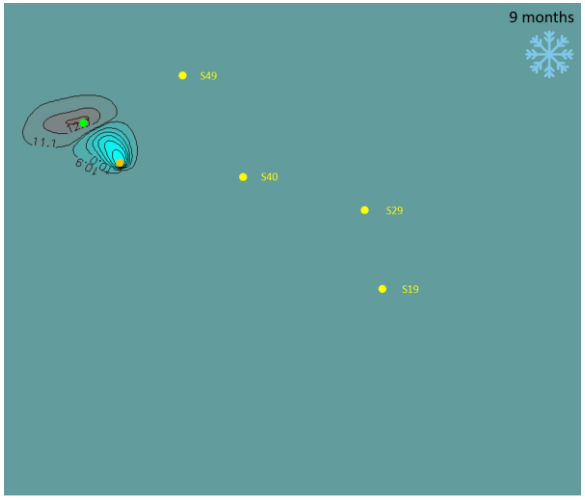

Year 1, Season 4: Spring period (Interseasonal regime)

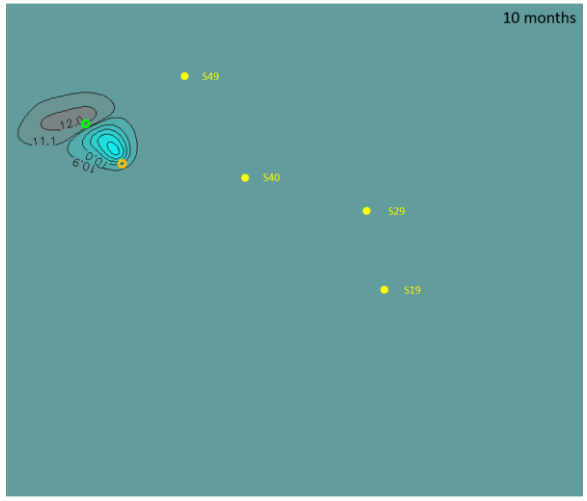

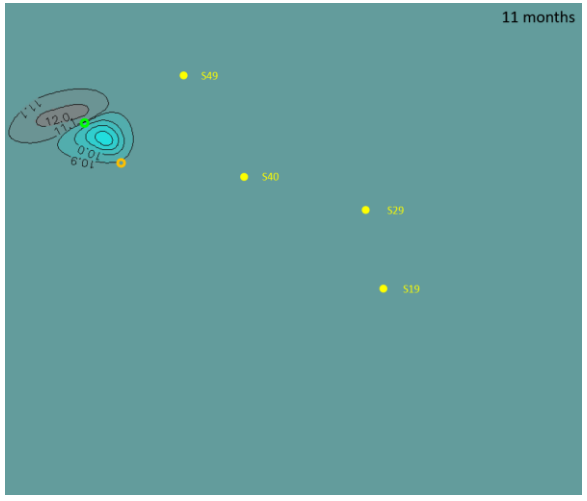

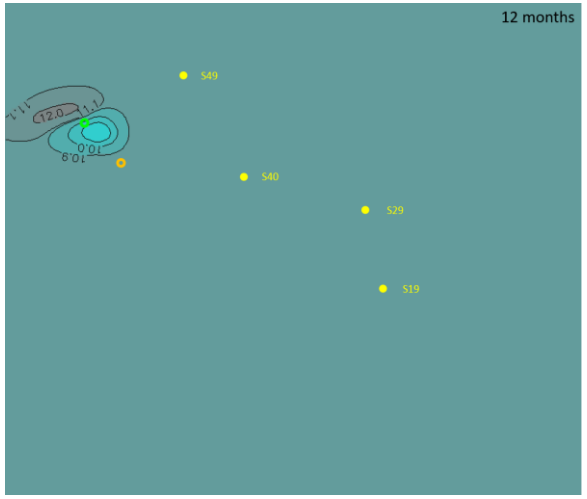

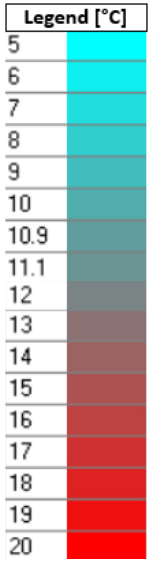

Active water injection
Inactive water injection
Extraction wells
Active water pumping
Inactive water pumping

Year 2, Season 1: Summer period

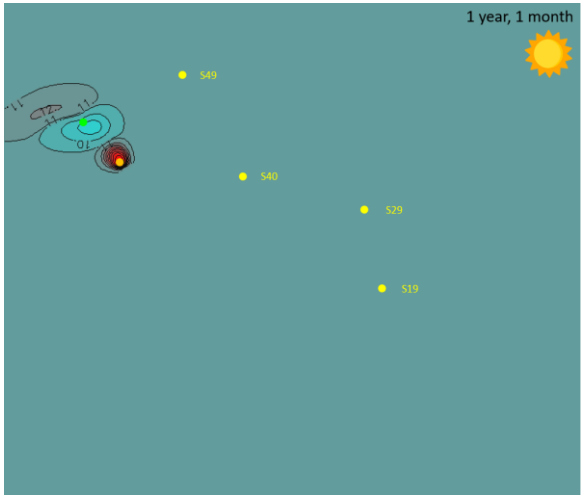

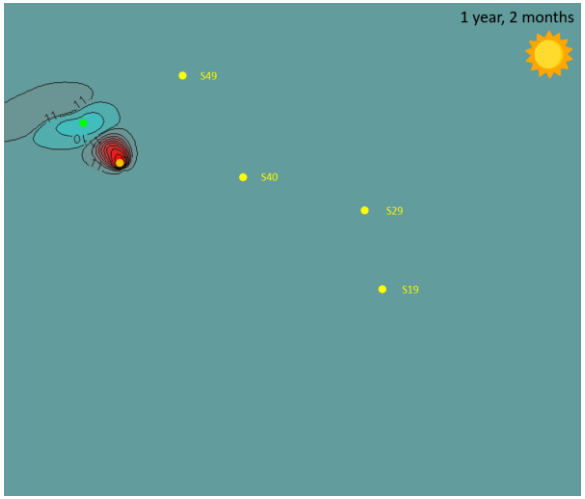

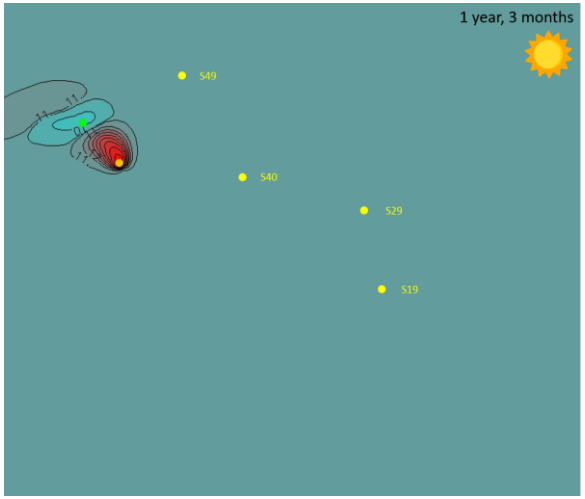

Year 2, Season 2: Autumn period (Interseasonal regime)

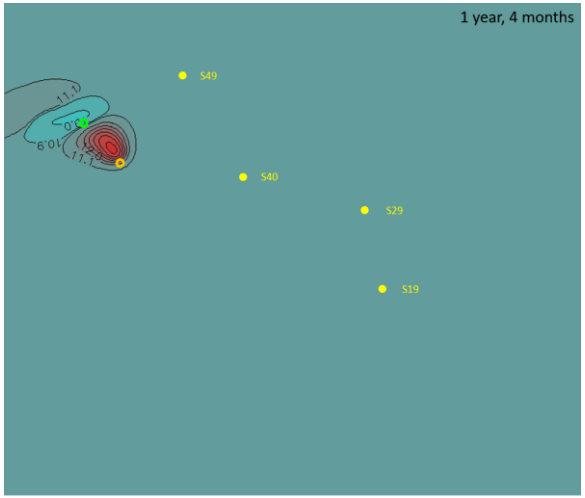

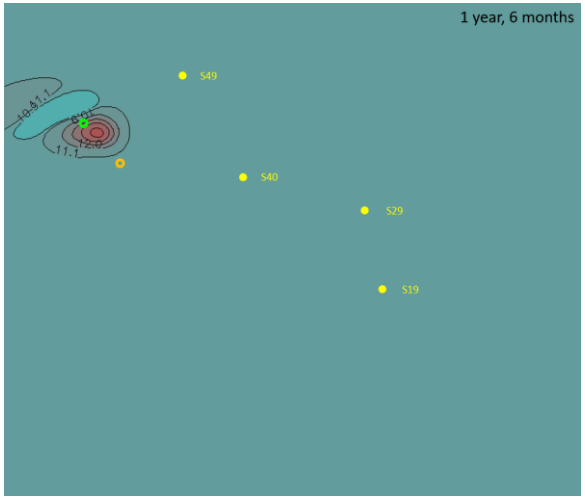

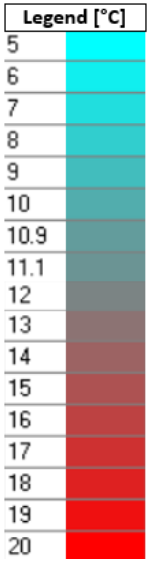

Active water injection
Inactive water injection
Extraction wells
Active water pumping
Inactive water pumping

Year 2, Season 3: Winter period

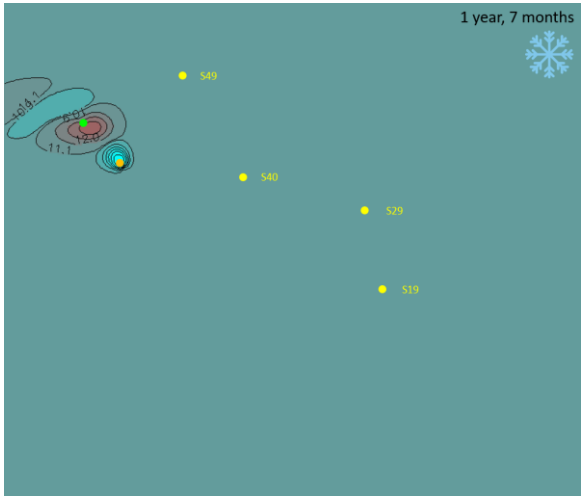

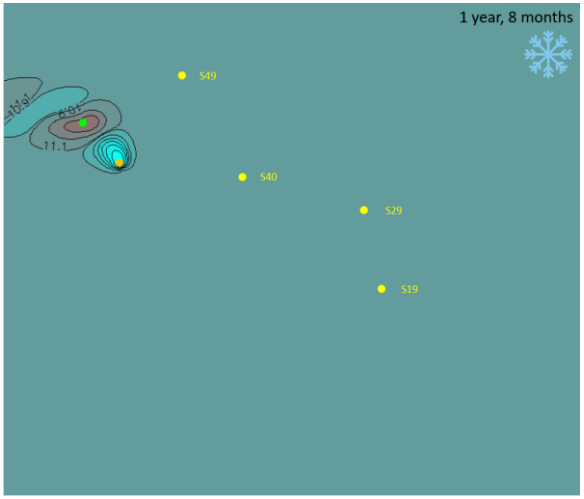

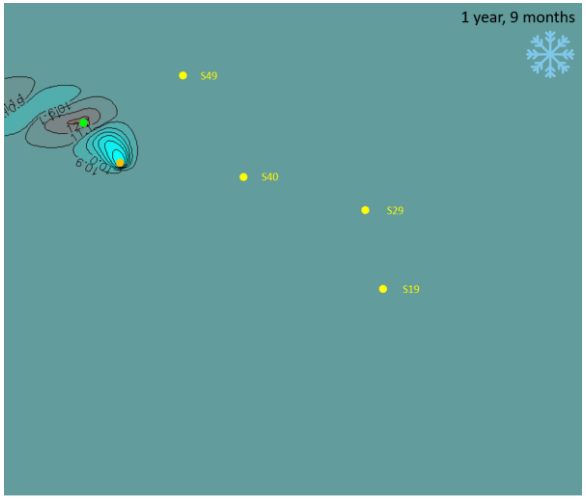

Year 2, Season 4: Spring period (Interseasonal regime)

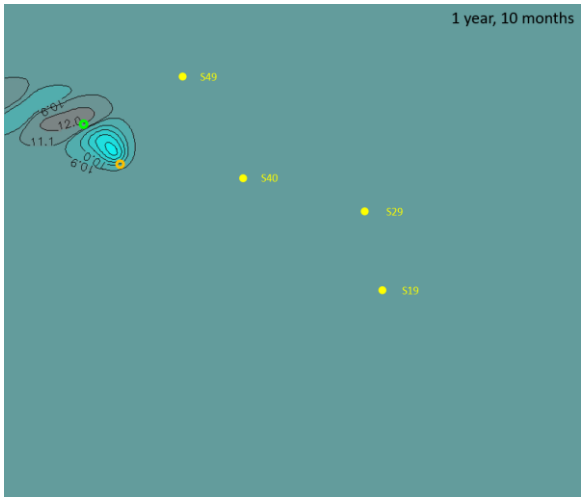

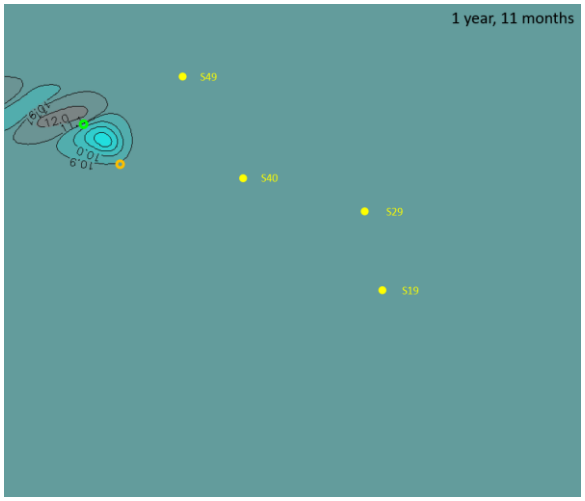

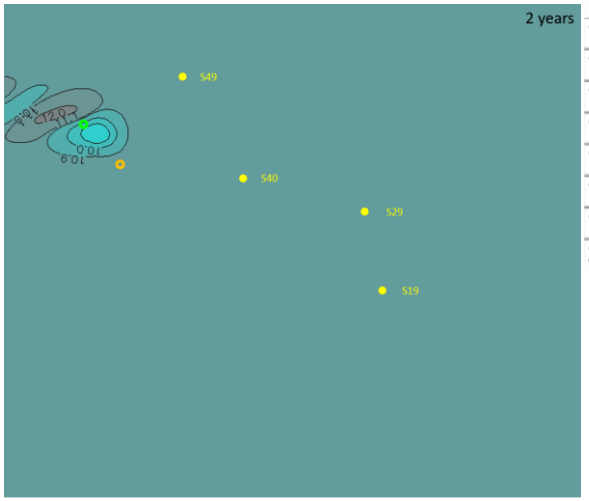

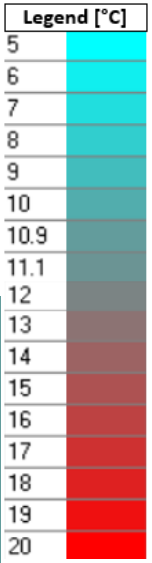

Active water injection
Inactive water injection
Extraction wells
Active water pumping
Inactive water pumping

Year 3, Season 1: Summer period

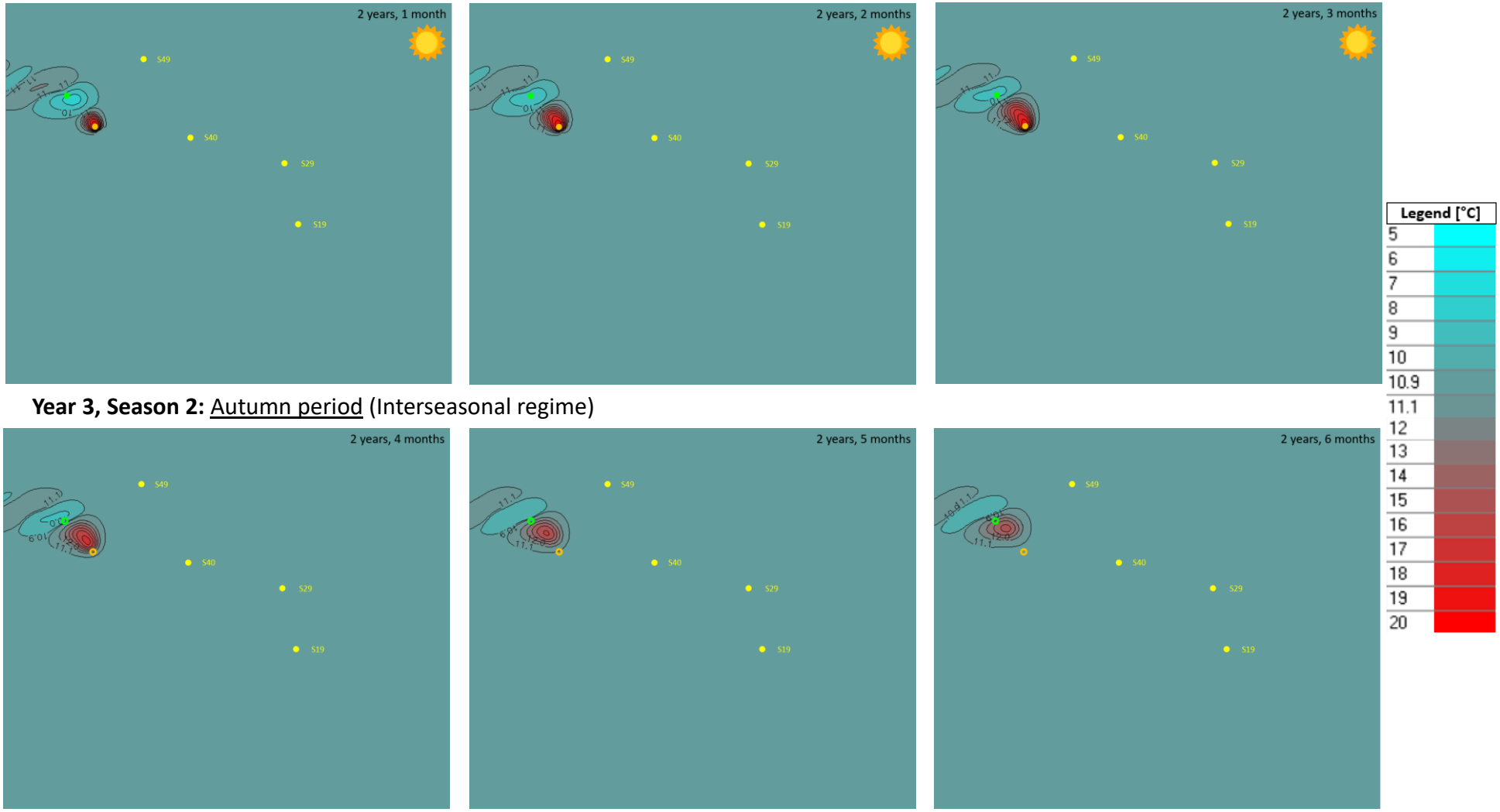

Year 3, Season 2: Autumn period (Interseasonal regime)

Active water injection
Inactive water injection
Extraction wells
Active water pumping
Inactive water pumping

Year 3, Season 3: Winter period

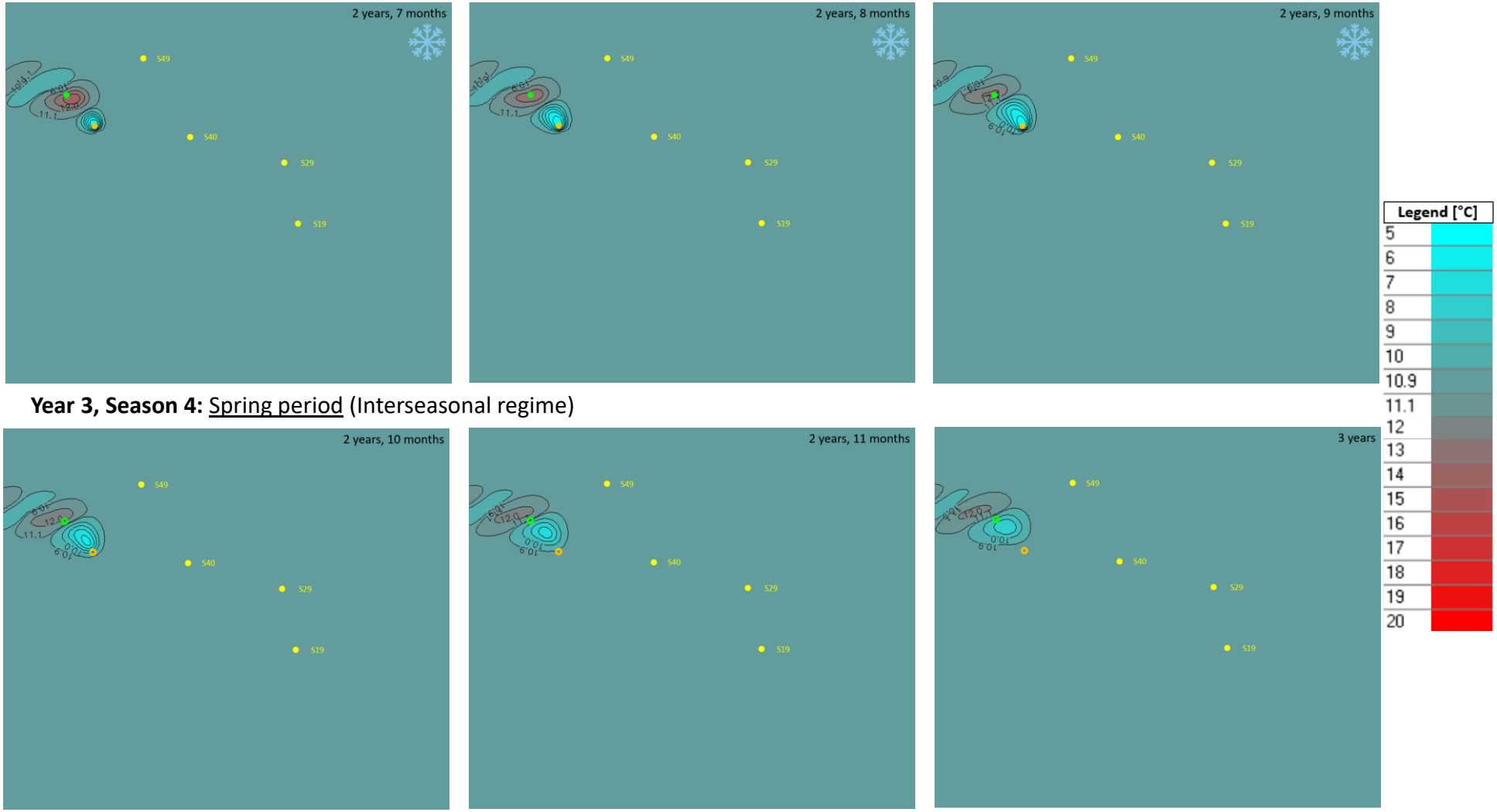

Year 3, Season 4: Spring period (Interseasonal regime)

Active water injection
Inactive water injection
Extraction wells
Active water pumping
Inactive water pumping

Figure 36 - Temporal evolution of the thermal plume stored by the ATES over 3 years (operating at a flow rate of 100m³/d at 20°C in summer and 5°C in winter), starting with summer. Each image corresponds to the situation after 1 month, and each row of images corresponds to a season.

Starting with winter:

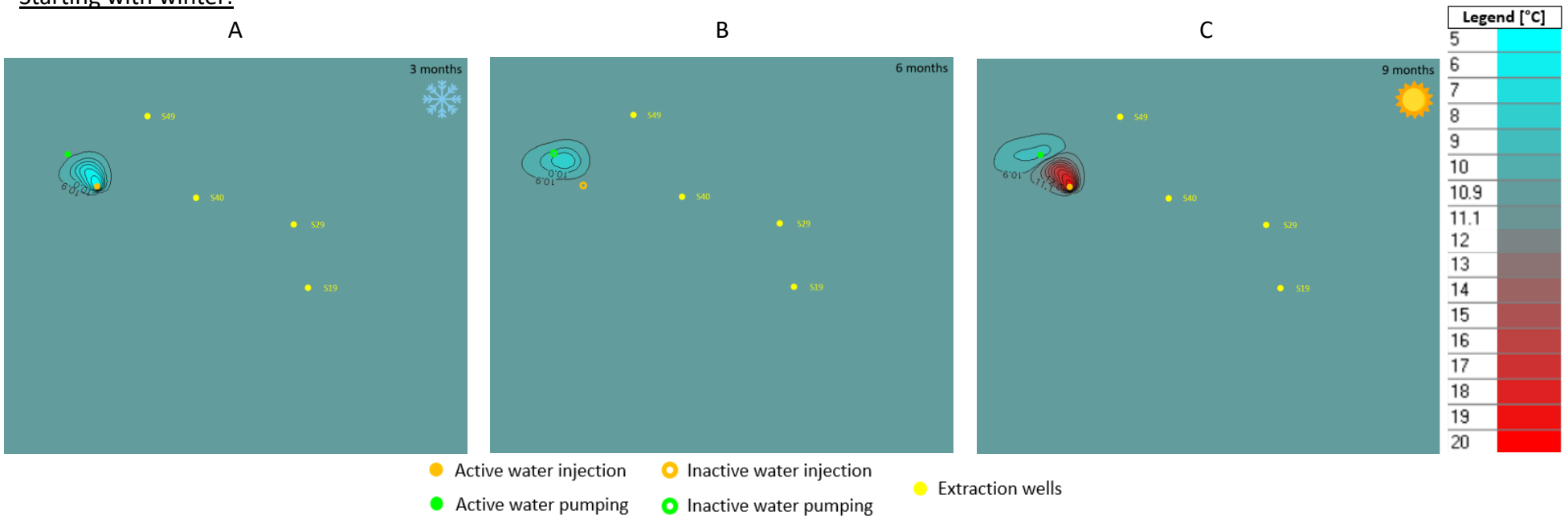

Figure 37 - Evolution of the thermal plume stored by the ATES system (operating at a flow rate of 100 m³/d) after 3 months injection at 5°C (A), 6 months (case A + 3 months rest) (B), 9 months (case B + 3 months injection at 20°C) (C), starting with winter

9.5.2. Lower summer injection temperature (15°C)

Configuration features: operational flow rate of 100 m³/d, with injection at 15°C in summer and 5°C in winter.

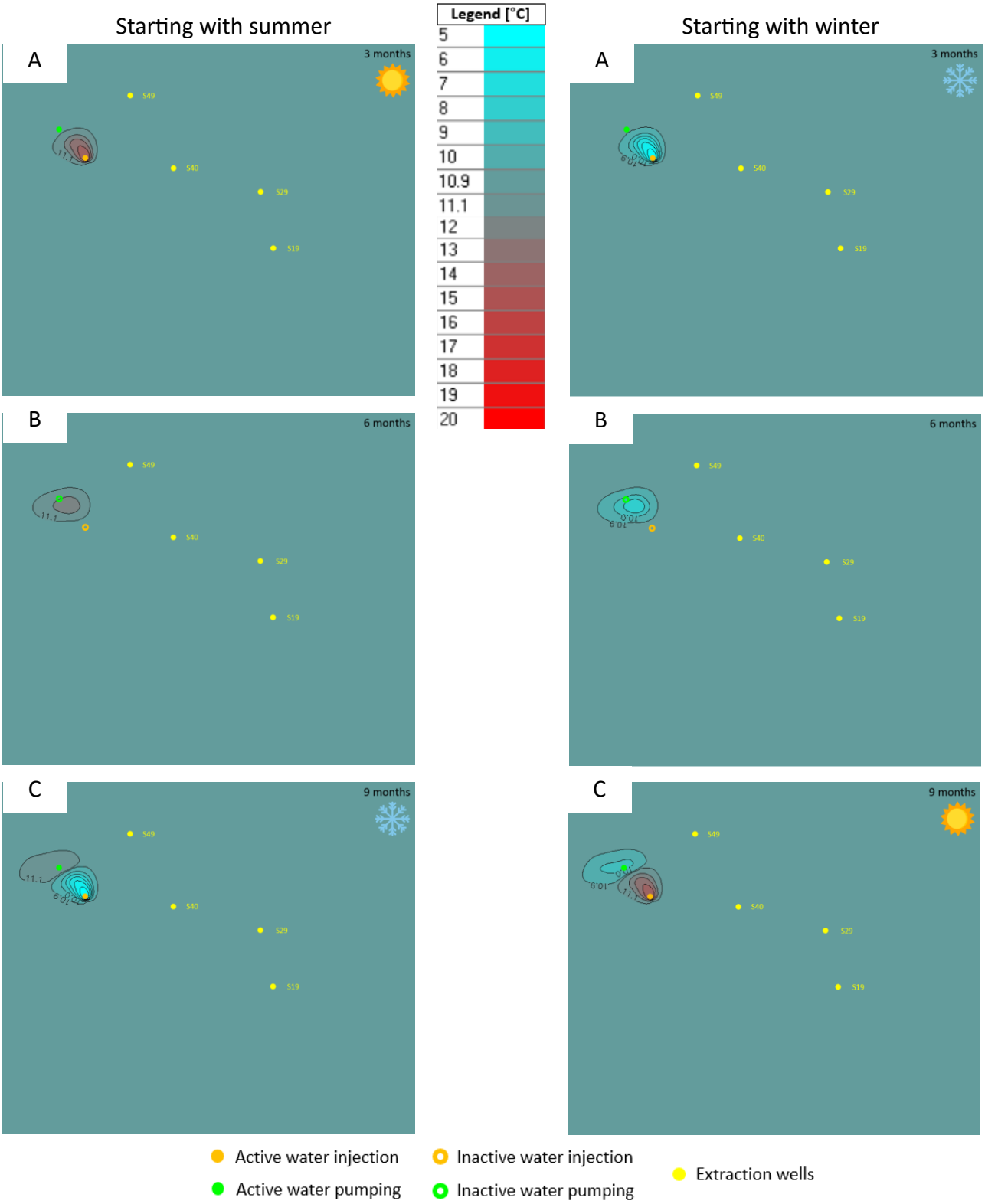

Figure 38 – Evolution of the thermal plume stored by the ATES system (operating at 100 m³/d) after 3 months injection (at 15°C in summer and 5°C in winter) (A), 6 months (case A + 3 months rest) (B), 9 months (case B + 3 months injection at 15°C in summer and 5°C in winter) (C).

9.5.3. Higher summer injection temperature (25°C)

Configuration Features: operational flow rate of 100 m³/d, with injection at 25°C in summer and 5°C in winter.

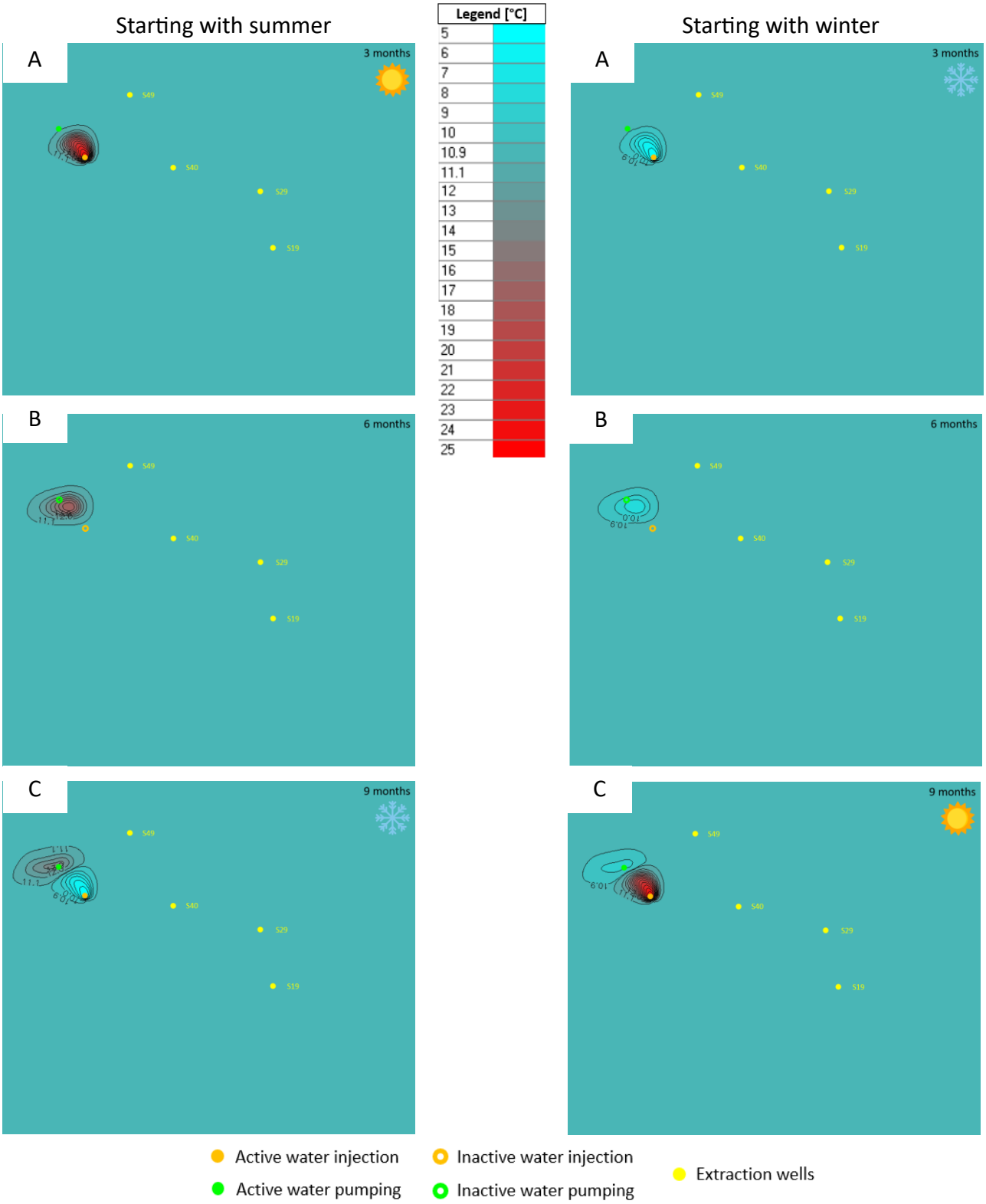

Figure 39 - Evolution of the thermal plume stored by the ATES system (operating at 100 m³/d) after 3 months injection (at 25°C in summer and 5°C in winter) (A), 6 months (case A + 3 months rest) (B), 9 months (case B + 3 months injection at 25°C in summer and 5°C in winter) (C).

9.5.4. Lower operating flow rate (50 m³/d) of the system

Configuration Features: operational flow rate of 50 m³/d, with injection at 20°C in summer and 5°C in winter.

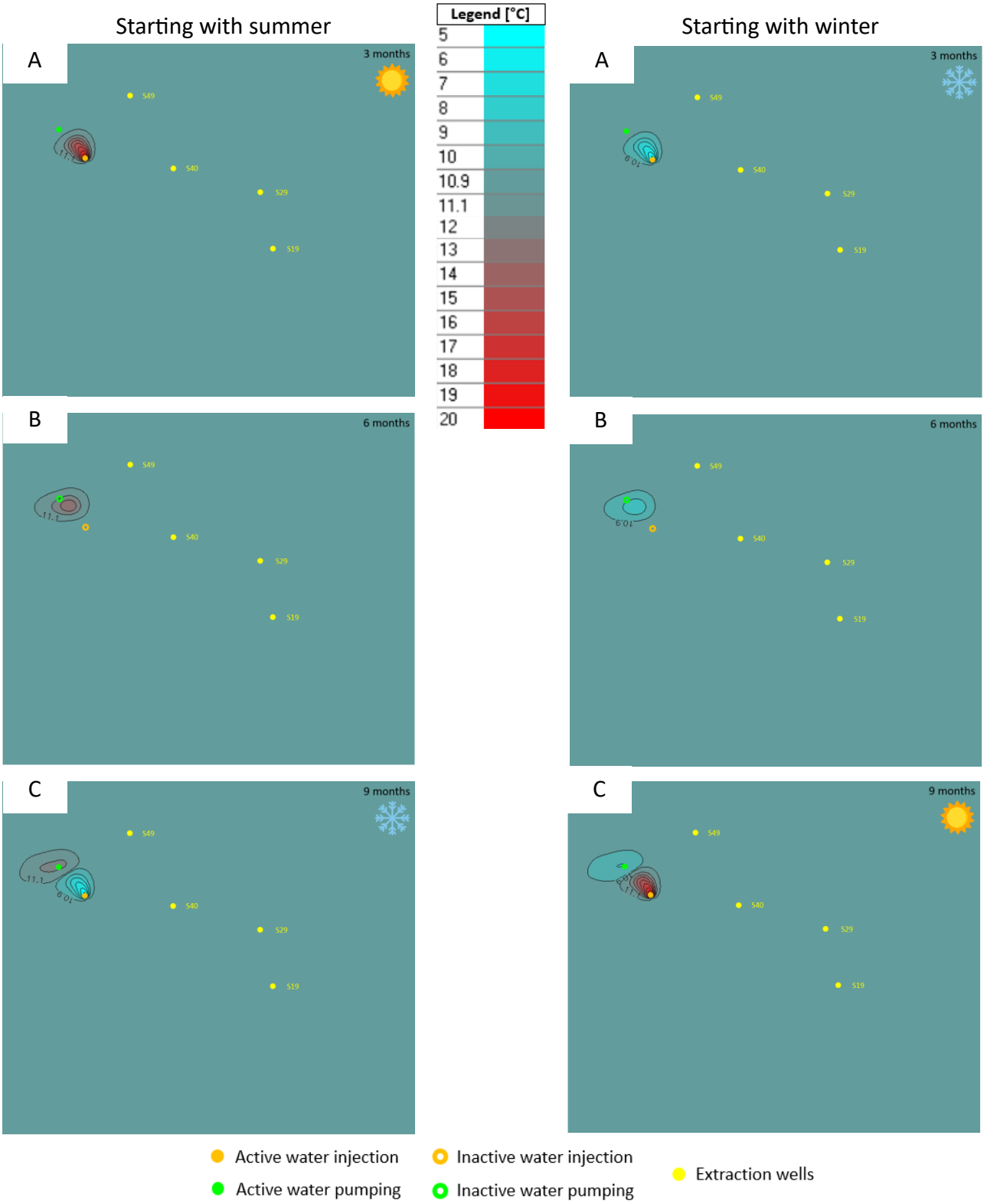

Figure 40 - Evolution of the thermal plume stored by the ATES system (operating at 50 m³/d) after 3 months injection (at 20°C in summer and 5°C in winter) (A), 6 months (case A + 3 months rest) (B), 9 months (case B + 3 months injection at 20°C in summer and 5°C in winter) (C).

9.5.5. Higher operating flow rate (200 m³/d) of the system

Configuration Features: operational flow rate of 200 m³/d, with injection at 20°C in summer and 5°C in winter.

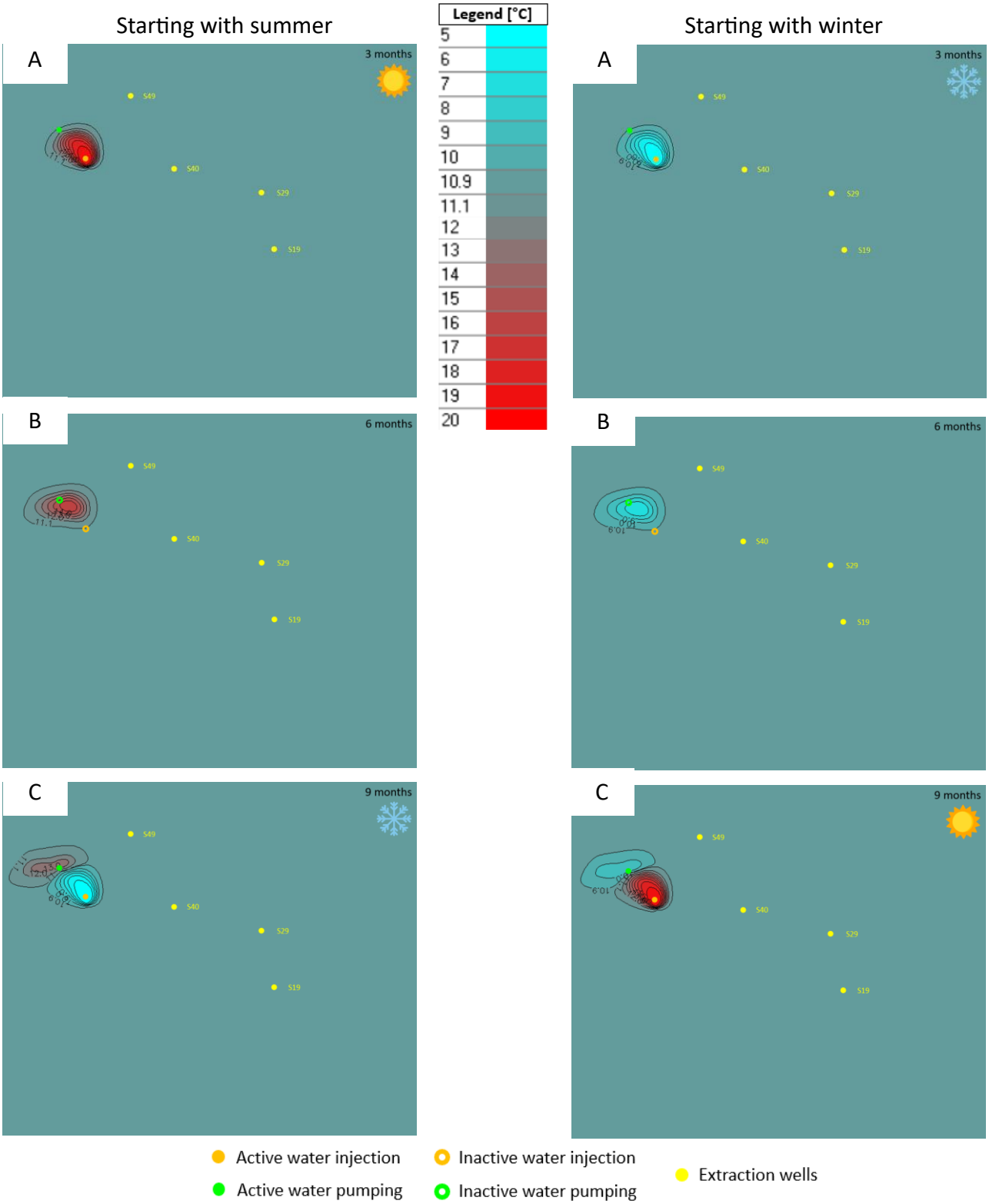

Figure 41 - Evolution of the thermal plume stored by the ATES system (operating at 200 m³/d) after 3 months injection (at 20°C in summer and 5°C in winter) (A), 6 months (case A + 3 months rest) (B), 9 months (case B + 3 months injection at 20°C in summer and 5°C in winter) (C).

Assessing thermal energy storage potential in the groundwater body of Louvain-la-Neuve

Quentin VAN BAMBEKE

Within a context of global warming, there is a need for an energy transition implying a reduction of primary energy consumption. This is particularly important in building environments, which are responsible for one-third of the world's final energy consumption.

In this context, the objective of this work was to assess the potential of interseasonal storage of surplus heat collected in the summer for recovery in winter in the urban setting of Louvain-la-Neuve (LLN).

The thermal storage system identified as most suitable for the LLN configuration is ATES (Aquifer Thermal Energy Storage), which utilizes the Brussels sands groundwater body as energy storage medium.

This study involved creating a lithostratigraphic model of the study area using the kriging method, followed by a hydrogeological model of the aquifer using MODFLOW software. Subsequently, the study explored the evolution of a simulated thermal plume behaviour throughout the study area to identify the most promising zones for installing an ATES system.
Next, a more in-depth analysis was made for the Blocry Sport Center, considering injection/pumping and flow periods. Thermal recovery efficiencies were calculated for different flow and injection temperature configurations to identify well locations that improve the storage system's performance.

Results confirm the potential of energy storage with efficiencies depending on the configuration of the ATES system. Additional data collection and holistic system efficiency analysis are suggested to reduce prediction uncertainties of ATES performances.

UNIVERSITÉ CATHOLIQUE DE LOUVAIN
Faculté des bioingénieurs
Croix du Sud, 2 bte L7.05.01, 1348 Louvain-la-Neuve, Belgique | **www.uclouvain.be/agro**